中国科学技术大学

博士学位论文

RHIC-STAR 500GeV 质子-质子对撞中 J/ψ 的测量

作者姓名: 杨 钱

学科专业: 粒子物理与原子核物理

导师姓名: 李 澄 教授

阮丽娟 研究员

唐泽波 副教授

完成时间: 二〇一七年四月

University of Science and Technology of China

A dissertation for doctor's degree

J/ψ production in proton+proton collisions at $\sqrt{s}$ = 500 GeV from the STAR experiment

Author :	Qian Yang
Specialty :	Particle and Nuclear Physics
Supervisor :	Prof. Cheng Li
	Prof. Lijuan Ruan
	Prof. Zebo Tang
Finished Time :	May, 2017

中国科学技术大学学位论文原创性声明

本人声明所呈交的学位论文，是本人在导师指导下进行研究工作所取得的成果。除已特别加以标注和致谢的地方外，论文中不包含任何他人已经发表或撰写过的研究成果。与我一同工作的同志对本研究所做的贡献均已在论文中作了明确的说明。

作者签名：_____　　签字日期：_____

中国科学技术大学学位论文授权使用声明

作为申请学位的条件之一，学位论文著作权拥有者授权中国科学技术大学拥有学位论文的部分使用权，即：学校有权按有关规定向国家有关部门或机构送交论文的复印件和电子版，允许论文被查阅和借阅，可以将学位论文编入《中国学位论文全文数据库》等有关数据库进行检索，可以采用影印、缩印或扫描等复制手段保存、汇编学位论文。本人提交的电子文档的内容和纸质论文的内容相一致。

保密的学位论文在解密后也遵守此规定。

□公开　□保密（____ 年）

作者签名：_____　　导师签名：_____

签字日期：_____　　签字日期：_____

摘 要

J/ψ 是粲夸克及其反粲夸克组成的束缚态，是最简单的量子色动力学 QCD 束缚态之一，是研究 QCD 的很好的探针。自 1974 年被发现以来，对其产生机制的实验和理论就从未中断过。J/ψ 的产生过程通常可以被划分为两个子过程：粲夸克和反粲夸克对的产生以及夸克对演化成束缚态的过程。粲夸克对产生通常是具有较大四动量转移的硬过程，可以通过微扰量子色动力学 (pQCD) 计算。而粲夸克对演化到 J/ψ 的过程是一个非微扰的软过程，只能通过唯象模型来描述。目前在描述 J/ψ 产生的诸多模型中，比较成功的有色单态模型 (CSM), 色蒸发模型 (CEM), 以及色八重态模型 (COM)。但目前没有任何一个模型能够同时描述所有的实验测量结果。在实验中观测到的 J/ψ，不仅包括由粲夸克对演化产生的直接贡献，还包含从更高阶的粲偶素和 B 介子衰变而来的贡献，从而进一步加大了研究 J/ψ 产生机制的难度。

此外，粲夸克对在强子对撞的产生并没有被完全理解。ALICE 合作组最近测量了在质子-质子 7TeV 对撞能量下粲夸克和 J/ψ 的产生随带电粒子多重数的变化。该结果显示随着带电粒子多重数的增加，粲夸克和 J/ψ 产生相对于多重数有强于线性的增长，并且这种增长没有横动量依赖性。J/ψ 和粲夸克的非线性增长在测量精度下高度一致预示该非线性增强可能来自于粲夸克的产生过程而非强子化过程。目前包含流体力学模型的事例产生器 EPOS 3.099 以及渗透模型都能够较好的描述 ALICE 的实验数据。但是造成该非线性增长的深层次物理机制并没有被完全理解。因此在新的对撞能量下测量 J/ψ 的产额以及其与带电多重数的关联，对于人们理解强子对撞中粲夸克对的产生机制及其演化过程有极大帮助。

在本文中，我们首次精确测量了 J/ψ 在 RHIC-STAR 质子质子 500 GeV 对撞中的产生截面及其与带电多重数的关联。本文通过 J/ψ 的双电子衰变道来重建 J/ψ，采用的的数据是由电磁量能器阈触发得到的样本。电磁量能器触发的方式，极大的压低了背景事例，显著提高了 J/ψ 事例的积分亮度。得益于 STAR 优越的电子鉴别能力和极高的积分亮度，通过过修正触发效率，径迹重建效率等效率和接受度的影响，得到了 J/ψ 在 $4 < p_T < 20$ GeV/c 横动量区间的产额的精确测量结果。该测量结果能够被次领头阶 (NLO) 的色八重态模型描述，虽然该色八重态模型并没有包含通过 B 粒子衰变来 J/ψ 的贡献。同时对于 J/ψ 的微分截面我们也做了 x_T 标度的检测，在测量的动力学区间，J/ψ 的微分截面遵循 x_T 标度。我们同时也首次在 RHIC STAR 上测量了在横动量区间为 $4 < p_T < 12$ GeV/c 的 $\psi(2S)$ 与 J/ψ 粒子衰变到双电子道的反应截面比，该比值为 $3.2 \pm 1\%$。该测量有助于剥离 J/ψ 中 $\psi(2S)$ 衰变的贡献

在 J/ψ 的产生随着带电多重数变化的测量中，我们观察到了与 ALICE 类似的非线性增强。在测量到的最高的带电多重数区间，J/ψ 的产额相对于平均值有

25 倍的增强。不同与 ALICE 的观测结果，该非线性增强有显著的横动量依赖性：J/ψ 横动量越高该非线性的增长就越强。该测量不能够被 PYTHIA8 模拟结果所描述：PYTHIA 8 低估了在高带电粒子多重数时 J/ψ 粒子的产生。

ABSTRACT

J/ψ production in hadron collision contains plenty of physics, which have attracted a lot interests both in experimentally and theoretically. One of the main interest is its production mechanism, which have not been fully understood yet. The intuitive expectation of producing a J/ψ can be understand in terms of two distinct steps: the production of $c\bar{c}$ pair, and the subsequent evolution of the $c\bar{c}$ pair into the J/ψ. Due to large mass of charm quark the process of producing a $c\bar{c}$ pair can be calculated by perturbative Quantum Chromodynamics (pQCD), while the evolution of the $c\bar{c}$ pair involves non-perurbative physics which can only be described by model. Different assumptions of the produced $c\bar{c}$ in terms of the different quantum number and in terms of the different evolution process have led to various J/ψ models. The most notable ones among these models are the color-singlet model (CSM), the color-evaporation model (CEM), and the non-relativistic QCD (NRQCD) factorization approach. However, none of the existing theoretical models can simultaneously describe the transverse momentum (p_T) spectrum and the polarization. Furthermore, the composition of inclusive J/ψ is complicated, which include direct production via gluon fusion, parton fragmentation, and feed-down from excited charmonium states and B hadrons. Measurements of J/ψ production at a different beam energy can shed new lights on the understanding of J/ψ production mechanisms, and help to constrain model calculations.

On the other hand, the production of $c\bar{c}$ could also be complicated. ALICE collaboration measured the charm production at central rapidity versus charged-particle multiplicity in proton-proton collisions at $\sqrt{s}$ = 7 TeV. A faster than linear increase of the relative D meson yield as a function of charged-particle multiplicity at high multiplicity range is observed with no significant p_T dependence. By comparison of open charm and hidden charm's results, it concluded that the yield enhancement is related the $c\bar{c}$ production process rather than the hadronisation process. Predictions from EPOS 3.099 with hydrodynamics and percolation model can both qualitative describe the data. However, the origin of the faster than linear increase is still not well understood. Measurement of J/ψ production as a function of charged-particle multiplicity at a very different collision energy of 500 GeV will help to understand the production and evolution of $c\bar{c}$ pair at different energy.

In this thesis, we report measurements of J/ψ production in p+p collisions at $\sqrt{s}$ = 500 GeV via di-electron channel at STAR. The data set used for the J/ψ reconstruction is triggered by Barrel Electromagnetic Calorimeter (BEMC) which requires the deposit energy inside the calorimeter above certain threshold. The trigger enriches the high

p_T electron sample and also ensured the reconstructed vertex to be the correct vertex associated with a J/ψ in a high pile-up background. The particle identification of the trigger electrons is selected by the ionization energy loss (dE/dx) measured by the Time Projection Chamber (TPC) and the energy deposition in the BEMC. The other electrons with relative low transverse momenta are identified by dE/dx alone. By pairing the identified electron and positron, the J/ψ is reconstructed at high p_T ($4 < p_T < 20$ GeV/c) with a good signal to background ratio. The inclusive J/ψ cross section as a function of transverse momentum has a large kinematic range with $4 < p_T < 20$ GeV/c at mid-rapidity. The NLO NRQCD prediction of the prompt J/ψ production is compared with the measurement and the prediction is consistent with our measurement. The J/ψ x_T scaling is also tested, our measurement also follow the x_T scaling with $p_T \geq 4$ GeV/c. Feed-down contributions from $\psi(2S)$ is studied in the p_T range of $4 < p_T < 12$ GeV/c, the measured $\psi(2S)$ to J/ψ yield ratio via di-electron decay is $3.2 \pm 1\%$.

In addition, the J/ψ production as a function of charged-particle multiplicity is also measured, which shows a strong than linear increase of the relative J/ψ yield with respect to the relative multiplicity and reveals a significant p_T dependence. The p_T integrated J/ψ yield in events with a multiplicity of 4 times of the average charged-particle multiplicity is a factor of 25 respect to the average J/ψ yield. The results are compared with predications from PYTHIA8 simulation, The PYTHIA8 simulation underestimates the increase trend of J/ψ yields with respect to the charged-particle multiplicity at high multiplicities.

Table of Contents

List of Tables

List of Figures

Chapter 1 Introduction

1.1 The subatomic world

The understanding of the natural world is originated from looking for the basic composite particle and the description of interaction between particles. J.J. Thomson studied "cathode rays" emitted by a hot electrode. He measured the charge-to-mass ratio of "cathode rays", which turn out to be a thousand times larger than that of hydrogen. He pointed out that the new charged particle produced by radioactive material is universal. This new particle is electron, it is the first measured "block" particle. In 1909, Rutherford scattered α particles off a gold foil. High deflection angle of the α particles indicate that the atom's positive charges are concentrated in a tiny core. Rutherford's experiment is more than telling the structure of the atom, but providing a method to explore the subatomic world. In 1934, to explain the bound state of nucleus, H. Yukawa proposed a new particle to carry the strong force between neutrons and protons. The new particle was named as meson. The interaction is happen by exchanging meson between two nucleons. This interaction picture has been extended to all subatomic world, which gives a fundamental describing of force. In 1956, the K^+ particle was actually thought to be 2 different particles. The K^+ shows different parity in different decay channels, which is the so called "τ-θ puzzle". T. D. Lee and C. N. Yang resolved this puzzle by proposing that parity is violated in the weak interactions [1]. And the parity violation is quickly confirmed by C.S. Wu, who took the polarized ^{60}Co beta decay electron's direction as the reference direction [2] . The discovery of parity violated describes the unique property of weak interactions.

With the invention of the bubble chamber by Donald Glaser in 1952 and the developments of particle accelerators, particle physics comes to an era of particles zoo. With so many new particles been discovered, the physicist was looking for some order to the chaos. In 1962, M.Gell-Mann introduced "The Eightfold Way" to organize the hadrons and predicted the existence of Ω^-. The Ω^- was discovered in 1964. The success of "The Eightfold Way" indicated that in these subatomic particles some more basic blocks may exist. In 1964, Gell-Mann and Zweig introduced quarks (aces) to explain the picture of "The Eightfold Way". They argue that quarks are the basic blocks of all hadrons. Mesons are a bound state of quark and anti-quark. Baryons are qqq triplets. In 1968, high energy electrons were used to probing the structure of proton by firing electrons to protons at Standford Linear Accelerator Center (SLAC), which is so called deep inelastic scattering (DIS) experiment [3, 4]. The Experiment data showed a "Bjorken scaling" which means quarks are "asymptotically free" when probing at very short dis-

tances, even though they are bound tightly at long distances. This scaling behavior was thought to be the evidence of the existence of quarks.

In 1974, many things came to a point. The quark model had already got plenty of successes. One only needs three different kinds of quarks in various combinations to explain all of the new particles. However, there were also plenty of doubters as to whether quarks are real or just a coincidence but useful tool for theorists. In 1972, Quantum Chromodynamics were introduced. QCD explained the reason why there is no free quark been measured and the necessary requirements of the strong interactions which will not mess up the simple results seen in the deep inelastic scattering experiments. However, due to the property of strong force, the QCD equations can not be solving just like QED equations. Hence, a proof was needed for QCD. Also in 1967, Weinberg and Salam proposed a theory which unified the electromagnetic interaction and weak interaction. Experimental evidence began to build up In 1973. Experiments at CERN discovered the so-called 'neutral currents', which is just the Z^0 boson predicted by theory. However, the electroweak theory unambiguously predicted the fourth kind of quark to make it a complete theory. With such a background in 1974, the J/ψ particle was discovered. The discovery of J/ψ is normally called the November revolution in particle physics. The found of J/ψ is self-consistent in all the pictures: quarks, QCD, and the electroweak theory. Furthermore, J/ψ is consitiuted another new quark: the charm quark. After the discovery of J/ψ, the era of fundamental discoveries with colliding beams began. Following the J/ψ discovery, the third generation quarks were discovered in 1977 [5] and 1995 [6], separately. With all the basic blocks been discovered, and the description in their interaction mechanism, the model used to described the subatomic world came into being, which is the Standard Model [7].

1.2 Standard model

In the Standard Model, the elementary particles can be classified into three groups: quarks, leptons, gauge bosons, as all be shown in Figrue 1.1. There are six kinds of quarks named as up, down, charm, strange, top, and bottom, which can be divided into three generations according to their properties. The quarks have a vast mass range: the lightest quark (up) has a mass of 2.3 MeV/c^2, while the most massive one (top) is about 170 GeV/c^2. The electric charges of quarks are fractional, in which the up, charm, and top quarks have a charge of 2/3, while the electric charge for the down, strange, and bottom quarks are -1/3. The quarks also carry the color charge (red, green, blue and the anti-ones), which are the source of strong interaction. Leptons can also be divided into three generations. Each generation consists of one electric charged lepton (also known as electron-like lepton) and the corresponding neutral lepton (better known as

neutrinos). Leptons are colorless particles, which don't participate in strong interactions. Quarks and leptons are the basic building block of matter with a spin of 1/2. The interactions between these basic blocks result from the exchange of force-carrier particles (gauge bosons). Photon is the mediator of electromagnetic force. The Z and W bosons are the carriers of weak interaction. The electromagnetic and weak interactions can describe by the Quatuam Electrodynamics (QED), which is a pertubation theory of the electricmagnetic quantum vacuum. Analogous to photons in the electromagnetic force, the gluons mediate strong interactions between quarks. The strong interaction can be described by the Quantum Chromodynamics (QCD). Unlike the photon, which is the carrier of electromagnetic interactions but lacks an eletric charge, gluons themselves carry color charge, and therefore participate in the strong interaction in addtion to mediating it, which makes the QCD significantly harder to analyze than QED. Both magnitude ("relative strength") and "range" in QCD and QED are significant different. If we take the electromagnetic force strength as a reference, the weak force strength is 10 orders of magnitude lower than the electromagnetic force while the strong force strength is two orders of magnitude larger. The interaction range for electromagntic force is infinite, while for the strong and weak interactions, they are about 10^{-15} and 10^{18} m, respectively. According to the Standard Model, a field of the necessary kind (the "Higgs field") exists throughout space, and breaks certain symmetry laws of the electroweak interaction. The existence of this field triggers the Higgs mechanism, causing the gauge bosons responsible for the weak force to be massive, and explaining their very short range. This mechanism predicted the existence of Higgs boson [8], which was discovered at LHC in 2012 [9].

1.3 Quantum chromodynamics

Quantum Chromodynamics is a local non-abelian gauge theory with symmetry group SU(3) [10], which describes the strong interactions between quarks and gluons. Gluons are the gauge bosons. The source of strong interaction is so-called color charge. Unlike the electric charge, the color charge is a quantum vector charge, just like the angular momentum in quantum mechanics. These are three fundamental colors: red, green, and blue. These three color form a basis in a 3-dimensional complex vector space. Any color state of quarks can be represented as a vector in the color space. Three colored quarks of each quark flavor consist the triplet basis in the fundamental representation of SU(3), while eight gluons form an octet in the adjoint representation. The gauge invariant QCD Lagrangian is

$$\mathcal{L}_{QCD} = -\frac{1}{4}F_a^{\mu\nu}F^{a\mu\nu} + \bar{\psi}_j(i\gamma_\mu D_{jk}^{mu} - M_j\delta_{jk})\psi_k, \tag{1.1}$$

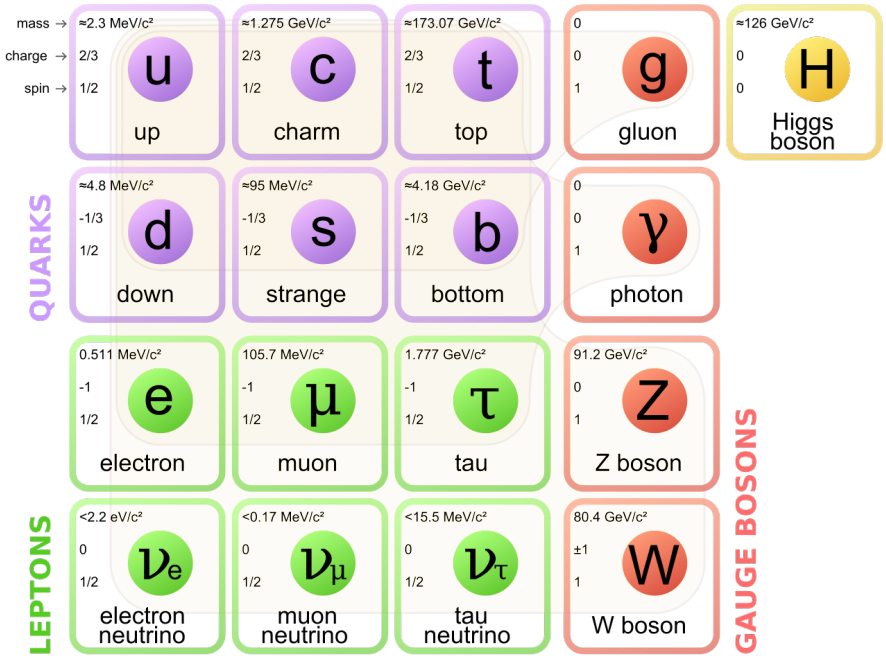

Figure 1.1: The elementary particles in Standard Model.

where the indices a, j and k refer to color and assume the value a = 1, ..., 8 and j, k = 1, 2, 3. ψ_k are the quark field. The $F_a^{\mu\nu}$ is the gauge invariant gluon field strength tensor. The covariant derivative D acting on a quark field is

$$D_{jk}^{\mu} = \delta_{jk}\partial^{\mu} + ig(T_a)_{jk}G_a^{\mu}, \tag{1.2}$$

where the G_a^{μ} is the gluon field. T_a are the SU(3) generators. M and g are the mass of quarks and strong coupling constants.

As mentioned, the main difference between QCD and QED is that the gluons can carry interaction source, thus gluons can interact with each other. This self-interaction property introduces a lot of unique and salient features of QCD, such as asymptotic freedom and color confinement.

1.3.1 Asymptotic freedom

Asymptotic freedom is one of the most striking properties of QCD. The picture of asymptotic freedom is that the coupling strength between two quarks becomes smaller as they getting closer [11]. This can be analogized from the simplest case in QED, the bound state of an electron and positron. In quantum field theory, the vacuum is a Dirac sea which has an infinite sea of particles with negative energy. When a photon propagates in the vacuum, it can induce a transition of the electron that in the Dirac sea from a negative state to a positive energy state. Virtually, photon creates a pair of electron and positron. As shown in the left panel of Figure 1.2, the coupling of the

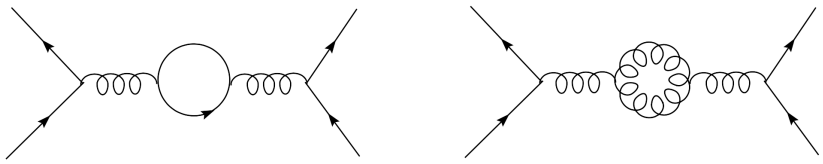

Figure 1.2: The vacuum fluctuation which effectively changes the interactions strength. The first diagram is shared by QED and QCD which renders the interaction stronger at shorter distance (screening). The second diagram arising from the nonlinear interaction between gluons in QCD has the antiscreening effect, which makes the coupling weaker at short distance.

original electron and positron will be affected by the electron and positron from pairing effect. Hence, the fine structure constant is depending on the distance between electron and positron. This dependence can be described by the differential equation in QED

$$\mu \frac{d\alpha(\mu)}{d\mu} = \beta(\alpha(\mu)), \tag{1.3}$$

The differential equation is also suited for strong coupling constant, but the $\beta(\alpha)$ function is different:

$$\beta(\alpha) = -\frac{\beta_0}{2\pi}\alpha^2 + ..., \tag{1.4}$$

with β_0 = 11 - $\frac{2}{3}$n$_f$, where n_f is the number of active quark flavor equivalent to the pairing electron and positron in QED. The number 11 in β_0 is from the non-line gluon contribution as shown in the right panel of Figrue 1.2. This negative 11 in the β indicates that the gluon has an anti-screening effect due to gluon self-coupling. The effective coupling constant can be written as:

$$\alpha_s(\mu) = \frac{2\pi}{\beta_0 ln(\mu/\Lambda_{QCD})}, \tag{1.5}$$

As the momentum scale increases ($\mu \to \infty$) or the distance approaches to 0, the α will close to 0. This behavior is the so-called asymptotic freedom. Experimental measurements [12] of α_s at different momentum transfer scale are shown in Figure 1.3, where Q is the four momentum transfer. The decreasing trend of α_s indicates the asymptotic freedom behavior between quarks.

The Λ_{QCD} is the strong interaction scale. It is introduced to set the scale at which the coupling constant becomes smaller enough to allow the perturbative calculation. The Λ_{QCD} is $\sim$ 250 MeV. So the QCD becomes a perturbative theory if $Q^2 \gg \Lambda^2_{QCD}$.

1.3.2 Color confinement

The color confinement is another prominent features of QCD. The color confinement requires that any strong interaction system at zero temperature and density must be in a color singlet state with distance scale larger than $1/\Lambda_{QCD}$ [13]. This kind of color

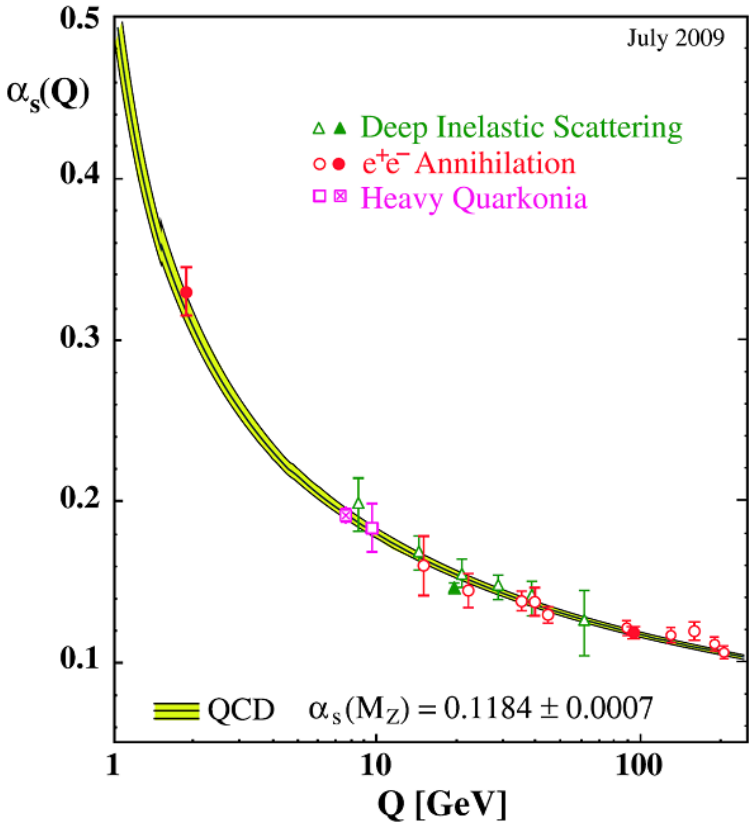

Figure 1.3: Experimentally measured α_s as a function of the energy scale Q [12].

confinement is the consequence of running of $\alpha_s(\mu)$. The color confinement restricts that no free quarks can be be observed. The physical picture of color confinement can be understood as following. When a color singlet state of quark-antiquark pair becomes separated, the gluon anti-screening effect becomes less and the interaction between two quarks becomes so large that it can pull out a new pair of quarks from vacuum. Hence, one can not find free quarks. The color confinement phenomenon is the QCD theoretical conjecture and consistent with currently experimental measurements, although the strict testifying in the QCD frame is still challenge.

Chapter 2 J/ψ meson

One of the most remarkable discoveries in particle physics in the last century is the observation of J/ψ meson. In 1974 November, the J/ψ was simultaneously discovered by two groups [14, 15]. The first group was led by Samuel Ting and used the AGS accelerator at Brookhaven. They [14] saw J/ψ signals in the e^+e^- mass spectrum in the reaction of

$$p + Be \rightarrow e^+e^- + anything. \tag{2.1}$$

While the second group was led by Burton Richter and used the SPEAR machine at SLAC, they used the reaction of

$$e^- + e^+ \rightarrow hadrons. \tag{2.2}$$

The observation of J/psi manifests the existence of charm quark. The new particle has two remarkable properties. The first one is the extreme narrowness in width comparing to other ordinary strong interaction resonances, which suggests a longer lifetime [16]. The second one is that it has a large mass of 3097 MeV/c^2. The large mass of charm quark makes it possible to make use of the non-relativistic approach in the $c\bar{c}$ system. The bound states of $c\bar{c}$, thus, can be analogous to positronium in the e^+e^- system.

The discovery of J/ψ was soon followed by the unveiling of the whole family of 'charmed' particles. A few days after the discovery of the J/ψ, $\psi(2S)$ was discovered at SPEAR, with a mass of 3686 MeV/c^2. Several other J/ψ family members have been found latter. The discovery of J/ψ also triggered a vast experimental effort of searching for heavy quark pairs. In 1977, upsilon was first discovered at Fermilab via at $\mu^+\mu^-$ channel in proton-nucleus collisions.

2.1 Charmonium

Figure 2.1 shows the $c\bar{c}$ spectroscopy [17]. Different $c\bar{c}$ states have different total angular momentum, charge conjugation, parity and principal quantum number. The J^{PC} assignment is shown at the bottom of the figure. Y axis shows the mass of different $c\bar{c}$ bond states. The dashed line shows the two times of the D^0 meson mass which is a bound state of a charm quark and an up quark. As shown in the figure, J/ψ is a spin-1, parity odd, charge-0 charmonium state. There are a whole set of spectroscopic recurrences of 1^{--} states just as J/ψ. All these states constitute the so-called J/ψ family. They can be analogous to orthopositronium in the case of e^+e^- bound states. One interesting thing is the width of different $c\bar{c}$ bound states. The mass of $D\bar{D}$ is a threshold for $c\bar{c}$ decay mode which decided the width of different $c\bar{c}$ bound states. Vector charmonium

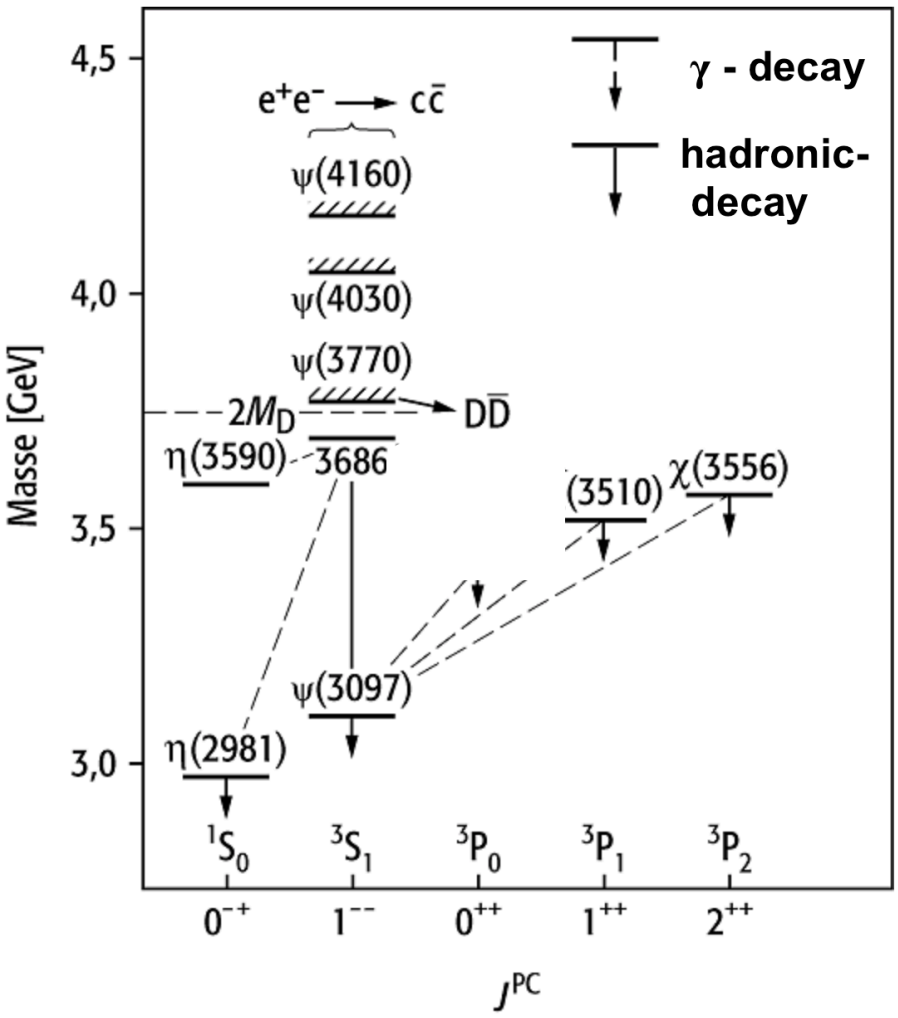

Figure 2.1: Level diagram for the J/ψ family.

states above this threshold are broad resonances, while those lying below the dash lines (J/ψ and $\psi(2S)$) have a very narrow width.

The width of J/ψ is $\Gamma \approx 93$ keV, which is a factor of 1000 smaller than a typical hadronic width. The extreme narrow width of J/ψ can be explained by OZI rule, which was invented by Okub, Zweig, and Iizuka. OZI rule argues that "disconnected quark diagrams are suppressed relative to connected ones". The lightest charm meson D^0 has a mass of 1.86 GeV/c^2, the J/ψ mass and $\psi(2S)$ mass are lower than the threshold for decaying into $D^0\bar{D}^0$. Hence, J/ψ can not decay into two D mesons but through OZI forbidden channels. The J/ψs mainly decay to hadrons with a branching ratio of 87.7 $\pm$ 0.5 %. However, the most favor channel in experiment measurement is the dilepton channels [18]. The branching ratios of J/ψ decay to di-electron and di-muon are 5.94 $\pm$ 0.06 % and 5.93 $\pm$ 0.06 %, respectively.

2.2 J/ψ production mechanism

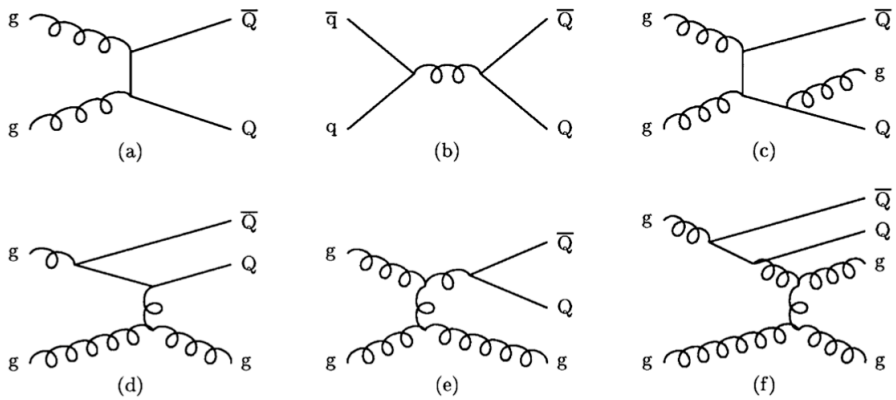

Figure 2.2: Examples of heavy-flavour production diagrams. (a,b) Leading order of gluon fusion and Quark-antiquark annihilation. (c) Pair creation with a gluon emission. (d) Flavour excitation. (e)Gluon splitting. (g)gluon splitting with an flavour excitation [19]

Since the discovery of J/ψ in 1974, measurements from different collider systems and collision energies were carried out to understand the J/ψ production mechanism. An intuitive picture of J/ψ production can be described into two steps. The first step is the production of the $c\bar{c}$ pair. And then followed by the subsequent evolution of the $c\bar{c}$ pair into a J/ψ meson. J/ψ has three intrinsic momentum scales, which can be used in describing the J/ψ production. They are the mass of charm quark, the momentum of the charm or anti-charm in J/ψ rest frame, and the binding energy of the $c\bar{c}$ pair. Due to the large mass of the charm quark, a non-relativistic dynamics can used to describe the momentum and binding energy scale. The momentum of charm in J/ψ rest frame is on the order of $m_c v$ and the binding energy of the $c\bar{c}$ pair is on the order of $m_c v^2$. The v is the velocity of the charm quark in the J/ψ rest frame ($v^2 \approx 0.3$). The charm quark mass ($\sim$ 1.5 GeV) is larger than the typical QCD scale. Hence, the process of producing a $c\bar{c}$ pair will have a large momentum transfer, which can be calculate in perturbative QCD (pQCD) frame. The process of producing a $c\bar{c}$ pair is often called 'short distance' process as it has a large momentum transfer. Figure 2.2 shows the Feynman diagrams of producing a heavy quark pair. (a) and (b) of Figure 2.2 [19] shows the leading-order diagram of $q\bar{q} \rightarrow c\bar{c}$ and $gg \rightarrow c\bar{c}$. The gluon fusion is the dominated source of charm production at RHIC energy range [46]. Some other higher order production channels are also shown.

The evolution of the $c\bar{c}$ into a J/ψ involves the small dynamical scales of charm quark's momentum and its binding energy, which reveals the non-perturbative feature. Hence, it is hard to describe the production of J/ψ from first principles, but can only be understood in model-dependent ways. This non-perturbative process is usually called

'long distance' process. In order to use the "$c\bar{c}$ pair + evolution" intuitive picture of J/ψ production, one must demonstrate that the short-distance can be separated from the long-distance. Such a separation is known as 'factorization'. By using the factorization theorem, the short-distance cross section should be expressed as a sum of products of infrared-safe, short-distance coefficients, while the long-distance dynamics can be expressed as an operator matrix elements. The short-distance coefficients can obtain by perturbative calculation at high p_T range. The operator matrix element involves all long-distance, non-perturbative physics. The operator matrix element can be determined by experiment measurement or phenomenologically.

The $c\bar{c}$ evolution has been extensively discussed in terms of models. Different assumptions are applied to the produced $c\bar{c}$ pair and its evolution process, which led to various theoretical models for J/ψ production. Among various of models, the color-evaporation model (CEM), the color-single model (CSM) and the most phenomenologically successful, so far, non-relativistic QCD (NRQCD) factorization approach are most notable. All these models are based on the fact that J/ψ is a colorless particle with $J^{PC} = 1^{--}$, while the produced $c\bar{c}$ pair could have different quantum assumption either in a color-single state or a color-octet state. Then the evolution of these different color $c\bar{c}$ states will have a total different evolution picture. Each of these models has its advantages and defects, which will be discussed in later section.

2.2.1 Color singlet model

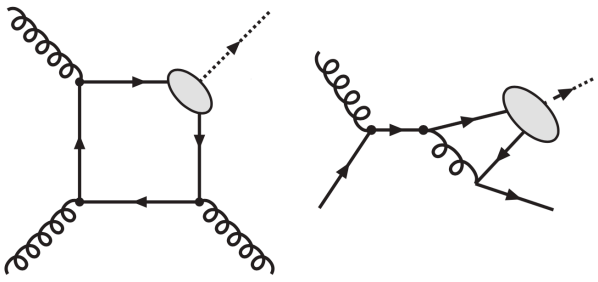

Figure 2.3: Leading order (α_S^3) of diagrams contributed to $^3S_1$ charmonium hadroproduction via color singlet channels.

The color-singlet model (CSM) [20–22] is the first model that described the inclusive J/ψ production at relatively low energy [23]. The color-single model considers that the produced $c\bar{c}$ has explicitly the same quantum number as the final state J/ψ. This means the produced $c\bar{c}$ pair is in a color-singlet state with the same spin and angular momentum as J/ψ. The following long-distance evolution will not affect quantum number

of $c\bar{c}$ pair. Thus all information are determined by the hard process. The production rate of different charmonium state is a function of the color-singlet $c\bar{c}$ wave function and its derivatives at zero separation of $c\bar{c}$. And these quantities need to be extracted from experimental data. Once it determined, the color singlet model has no more free parameters and can give predictions of J/ψ cross sections. The assumption made by color single model constraines the channels of producing a color singlet $c\bar{c}$. Two gluon fusion will produce a C-even state, while the J/ψ is a C-odd states, thus the production of a color singlet $c\bar{c}$ in gluon-gluon fusion channel will be accompanied by another gluon. So the leading order of producing a $c\bar{c}$ in the color singlet model is in the order of α_S^3 and the $c\bar{c}$ is in ${}^3S_1$ state. Figure 2.3 shows the leading order diagrams contributed to ${}^3S_1$ charmonium state in a color singlet state.

Recent calculations show that color-singlet next-to-leading order (NLO) and next-to-next-leading order (NNLO) correction at α_S^4 and α_S^5, respectively, have very large correction to the $c\bar{c}$ cross section especially at large-p_T range [24–26]. The high order cross-section correction actually opens new production channels. These new channels show a more gently dropping in cross section as a function of p_T. The high order correction dominates the total cross section at high transverse momentum range. However, the larger contribution arising from α_S^4's diagram and α_S^5's diagram would cast doubt on the convergence of the perturbative expansion. Then, the comparison of leading order and next to leading order predictions are important. Another difficulty is that the color singlet model can only handle S-wave $c\bar{c}$ state. In color singlet model, leading relativistic correction from other states like ${}^1S_0^{[8]}$, ${}^3S_0^{[8]}$, and ${}^3P_J^{[8]}$ are not take into account, where the upper index '8' states the $c\bar{c}$ in color octet states. This omission of these channels leads to an uncanceled infrared divergence of the P-wave and higher-orbital-angular-momentum $c\bar{c}$ state cross section.

2.2.2 Color evaporation model

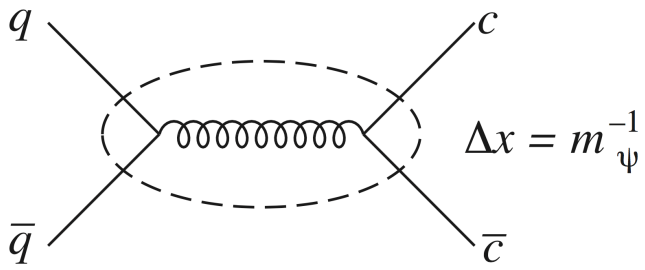

Figure 2.4: color evaporation J/ψ production.

The color-evaporation model (CEM) [27–29] was proposed shortly after the dis-

covery of J/ψ in 1974. Color evaporation model has a fundamental difference in dealing with the color requirement for $c\bar{c}$ pair. Rather than explicitly requiring the produced $c\bar{c}$ in a color single state, the appearance of color singlet asymptotic states depends only on the follow long-distance fluctuations of quarks and gluons. CEM argues that the long-distance fluctuations are complex, it can handle different color states respect to statistical counting. In other words, the color has been 'ignored' in producing the $c\bar{c}$ pair, and the colorless requirement becomes a non-perturbative phenomenon. For J/ψ case, the colorless requirement of J/ψ is initially ignored, as one of the production channel shown in Figure 2.4 [28, 30]. The leading order of produce a $c\bar{c}$ from $q\bar{q}$-annihilation is shown and this process can be calculated through pQCD. The process can be expressed in terms of short-distance interaction range $\Delta x \approx m_{J/\psi}^{-1}$. The colorless requirement is not necessary to be imposed at a short distance, the long distance, which has an infinite time, can readjust the color of $c\bar{c}$ by soft gluons before forming a color singlet J/ψ. Then the inclusive cross section of produce a J/ψ is the sum over the colors and spins of the final state $c\bar{c}$ pairs.

There are some very strong assumptions in the color evaporation model. It assumed that every produced $c\bar{c}$ pair evolves into a charmonium statue as long as its invariant mass is less than the threshold of produce a pair of $D^0\bar{D}^0$ meson [31]. Another assumption is that the materialization of the $c\bar{c}$ into a charmonium state is process independent. The second assumption gives the fraction $\rho_{J/\psi}$, which describes the possibility of a $c\bar{c}$ evolved into a J/ψ. The fraction $\rho_{J/\psi}$ is energy-momentum and process independent. Thus the fraction $\rho_{J/\psi}$ is a universal value. Once it is determined by experimental data, color evaporation model can predict the J/ψ cross section in other processes and in other kinematic regions. The production cross section of J/ψ in p+p collisions can be written in

$$\sigma_{CEM}[p+p \to J/\psi + X] = \rho_{J/\psi} \int_{4m_c^2}^{4m_{D^0}^2} dm_c^2 \frac{d\sigma}{dm_{c\bar{c}}^2}[p+p \to c\bar{c} + X], \qquad (2.3)$$

where $m_{c\bar{c}}$ is the invariant mass of the $c\bar{c}$ pair, m_c is the charm quark mass, and the $d\sigma/dm_{c\bar{c}}^2$ is inclusive differential cross section of a $c\bar{c}$ pair produced in a the proton-proton collision.

2.2.3 Non-relativistic QCD approach

In 1995, Non-relativistic QCD (NRQCD) factorization approach [32] was proposed to describe the inclusive heavy-quarkonium production. By far, NRQCD is the most successful phenomenological model in describing the J/ψ production. The NRQCD is an effective-field-theory framework of non-relativistic QCD. It encompasses both CSM and COM. It also can be regarded as a unification of these two models within one

theoretical framework. The NRQCD approach can be used to separate the short-distance process from the longer-distance process associated with $c\bar{c}$ evolution. In NRQCD factorization approach, the cross section of J/ψ production can be described by the following formula

$$\sigma(AB \to J/\psi + X) = \sum_n \sigma(AB \to c\bar{c}[n] + x) < \mathcal{O}^{J/\psi}[n] > \tag{2.4}$$

where the $\sigma(AB \to c\bar{c}[n] + X)$ is the short distance process cross section used to described the production of a $c\bar{c}$ pair in an intermediate Fock state n at parton-level. This cross section can be obtained by perturbative calculation at the high-p_T range. One notable difference from the CSM is that the produced $c\bar{c}$ are not necessary to be color neutral state. The $c\bar{c}$ could also be in an color octet states. The $\mathcal{O}^{J/\psi}[n]$ are the long distance matrix elements (LDMEs). The LDMEs describe the transition of intermediate $c\bar{c}$ state into a J/ψ via soft gluon radiation. Unlike color singlet model and color evaporation model just with very few free parameters in describing the cross section, NRQCD factorization formula, as shown in equation 2.4, is a double expansion in powers of LDMEs and in powers of α_S. As mentioned, the non-perturbative physics process can be expressed in terms of momentum of charm in the J/ψ rest frame. Hence, LDMEs are described as a function of v. In the phenomenological calculation case, the formula needs to be truncated at fixed order in v, thus only a few matrix elements survived in the formula. So the NRQCD approach's prediction power is affected by perturbative calculability of the $c\bar{c}$ cross sections, LDMEs as well as the validity of truncation on LDMEs.

In equation 2.4, if one only take the color singlet contribution of leading order in v for each charmonium state, then one obtains the color singlet model. As discussed in earlier section, color singlet model is plague with uncanceled infrared divergences in P-wave production rates by ignoring the color octet contributions. While in NRQCD approach, one can well deal with this infrared divergences.

A comparison between CEM and NRQCD was carried out in [31]. They translated the CEM assumption into predictions of the ratios of NRQCD production matrix elements. They found that the velocity scaling assumption of NRQCD causes some odds predictions and disagreement between the NRQCD LDMEs extracted from phenomenology and CEM predictions. These facts indicate that the evolution of a $c\bar{c}$ into J/ψ from CEM is very different to NRQCD' s description.

The equation 2.4 has the assumption that one can obtain the $c\bar{c}$ production cross section from perturbative QCD, which means the momentum transfer in the hard-scattering production process is the order of charm quark mass or larger. Hence, the J/ψ $c\bar{c}$ production cross section can only obtain at high p_T (p_T > 5 GeV/c) [33–35]. While in low

$p_T \lesssim m_c$ region, the $c\bar{c}$ cross section is far from understanding. However, this low-p_T range dominates the total $c\bar{c}$ production cross section. Recently, a novel color glass condensate (CGS) + NRQCD framework [36] was proposed to describe the J/ψ production at low p_T range in proton-proton collision and proton-ion collision [58, 59]. The effective CGC theory at small x QCD range [39] can give prediction on $c\bar{c}$ pair cross section at low p_T range. x is define as $x \sim m_c/\sqrt{s}$, where $\sqrt{s}$ is the center-of-mass (c.m.) energy of the proton-proton system. In the CGC framework, by summing over all small x logs, it will lead to the phenomenon of gluon saturation, which can be characterized by a dynamically generated semihard scale Q_S in the hadron wave function [40, 41]. In the forward going 'dilute' proton, the x may have a small x resummation, but the phase space densities are still small. Meanwhile the phase space densities in the backward going proton, which is 'dense', can reach the maximal value of $1/\alpha_S$. Thus, the backward going proton will shows a gluon saturation state. Hence, the production of $c\bar{c}$ can be expressed in a "dilute-dense scattering" phenomenon. However, the validation of CGC effective theory requires a low-x range. So the CGC+NRQCD framework has a p_T range limitation. At high p_T range, the CGC+NRQCD may not valid. But the perturbative QCD computation of $c\bar{c}$ at high p_T range becomes reliable. Another nice feature of the CGC+NRQCD framework is that it can quantify color singlet's and color octet channels' contribution in the J/ψ production in both $p + p$ and $p + A$ collisions.

2.2.4 J/ψ polarization and reference frames

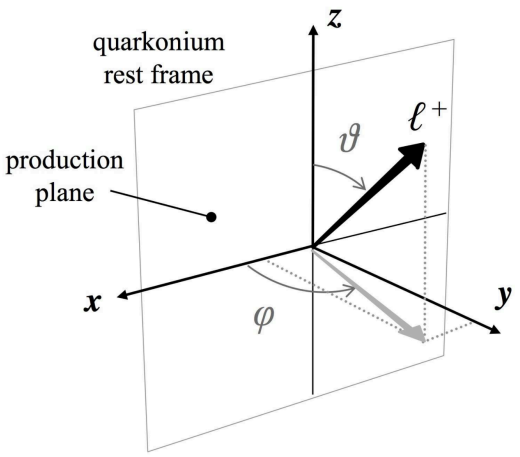

Figure 2.5: Coordinate system in J/ψ polarization measurement in the J/ψ rest frame [42].

To complete the discussion of J/ψ production mechanism, it is worth to mention another observable: J/ψ polarization. Rather than only focusing on the unpolarized cross section, J/ψ polarization measurement provides a new test for production mechanism models. J/ψ particle, with J=1, can have three polarization states in a particular

coordinate at the J/ψ rest frame. Figure 2.5 shows a coordinate system definition, The z-axis is defined as polar axis, x-axis and z-axis defined the production plane, the y-axis is along the production plane normal direction. The polar angle is the angle between the momentum of the J/ψ decayed lepton in the J/ψ rest frame and the polar axis z.

The geometrical shape of the angular distribution from decayed lepton has encoded the J/ψ polarization information. In the measurement, the J/ψ polarization is extracted from the distribution of the lepton momentum direction with respect to a certain spin quantization axis. The yield distribution is expressed as

$$1 + \alpha cos^2\theta_{ll} \tag{2.5}$$

where α is the fraction of longitudinal or transverse cross section, $\alpha = 1$ means full transverse polarization, $\alpha = -1$ means full longitudinal polarization. Different selec-

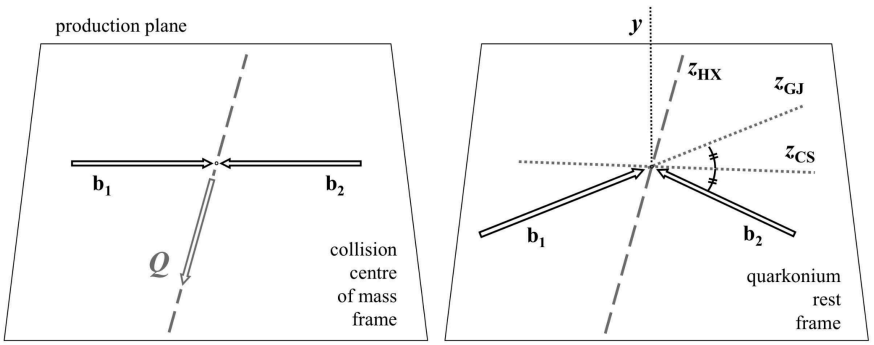

Figure 2.6: Left: production plane definition. Right: polarization axis in helicity (HX), Collins-Soper (CS) and Gottfried-Jackson (GJ) reference frames [42].

tion on the polar axis will define different reference frames. Currently, there are three favorite reference frames in the market: helicity [43], Collins-Soper [44] and Gottfried-Jackson [45] frame. All these three reference frames select the z-x plane as the production plane, as shown in the left plane of Figure 2.6. The definitions of polarization axis in these three reference frames are also shown on the right hand side.

The helicity frame (HX) choose J/ψ momentum direction in the laboratory reference frame as the polarization axis. HX frame is usually used in the collider experiments. The Collins-Soper frame (CS) defines the z-axis as a bisector of the angle formed by one beam direction and the opposite direction of the other beam, in the J/ψ rest frame:

$$z = \frac{\overrightarrow{P_b}}{P_b} - \frac{\overrightarrow{P_a}}{P_a}, \tag{2.6}$$

where $\overrightarrow{P_a}$ and $\overrightarrow{P_b}$ are the 3-momenta of each beam boosted into the J/ψ rest frame. In the Gottfried-Jackson frame (GJ), the polarization axis is chosen along the momentum vector of one beam boosted into the J/ψ rest frame.

2.3 Experimental measurements

Since 1974, numerous experimental collaborations measured the J/ψ production in different energies and reaction channels, and the measurements are still ongoing in current existing collaborations. The center-of-mass frame collisions energy has an enormous dynamics range of 6.8 GeV (CERN-PS) to 7000 GeV (ALICE), and the measurements were carried in abundant collision systems: proton-proton collisions, proton-antiproton collisions, as well as various proton-ion collisions. The measurements are also distributed in colliders and fixed-target experiments. In the follow section, some experimental measurements are shown and the comparison with different models are also be discussed.

2.3.1 Feed down

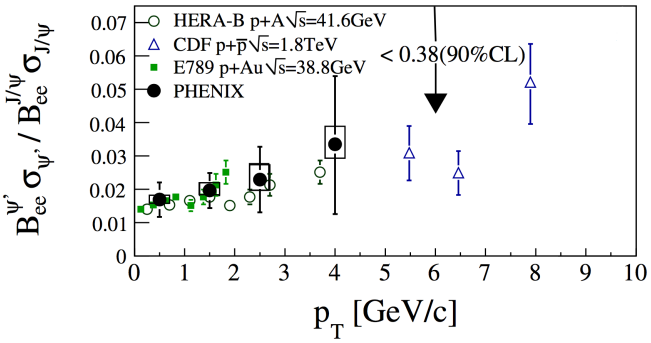

Figure 2.7: ψ' to J/ψ yield ratio involving branching ratio of e^+e^- channel [47].

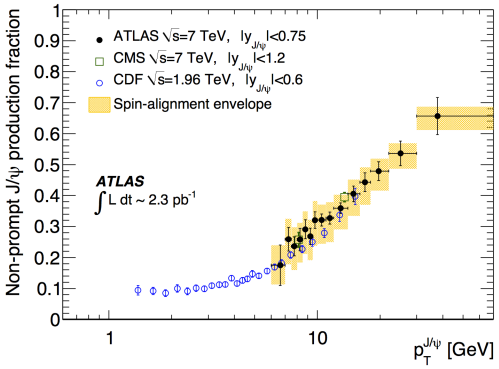

Figure 2.8: Non-prompt J/ψ to inclusive fractions as a function of J/ψ transverse momentum [48].

Before going to the measurements from different collaboration, feed-down contributions for J/ψ production should be mentioned. The measured inclusive J/ψ production has different production source, not only the contribution from $c\bar{c}$ evolution but also from decays. The inclusive J/ψ cross section has four kinds of component: (a) Direct J/ψ production, which is evolved from $c\bar{c}$, contributes $\sim$ 60% of inclusive J/ψ, (b) J/ψ

from $\psi(2S)$ decay (∼10%) [47], (c) J/ψ from χ_c decay (∼30%) [47], (d) J/ψ from B-mesons weak decay (∼6%) [48]. (a), (b), and (c) are so-called prompt J/ψ, correspondingly, (d) is the so-called non-prompt J/ψ. Figure 2.7 [47] shows the $B_{ee}^{\psi'}\sigma_{\psi'}/B_{ee}^{J/\psi}\sigma_{J/\psi}$ as a function of transverse momentum from different experiment measurements. Figure 2.8 [48] shows the non-prompt J/ψ to inclusive J/ψ fraction as a function of J/ψ transverse momentum. Both $\psi(2S)$ to J/ψ ratio and the non-prompt J/ψ fractions show a p_T dependence. The non-prompt J/ψ fractions at high-p_T range has a very rapid increase. At about 20 GeV/c, the non-prompt J/ψ fraction is $\sim$ 50%. Another interesting thing is that despite of a vast collision energy range, from 41.6 GeV to 1.8 TeV, and collision species, from p+p collisions to p+Au collisions, the $B_{ee}^{\psi'}\sigma_{\psi'}/B_{ee}^{J/\psi}\sigma_{J/\psi}$ curves follow an universal trend. The non-prompt J/ψ fraction also shows a universal trend. Distinguishing the different source of J/ψ in the inclusive measurement at different p_T range is helpful in making comparison between experimental measurements and different production mechanism models.

2.3.2 Cross section measurements

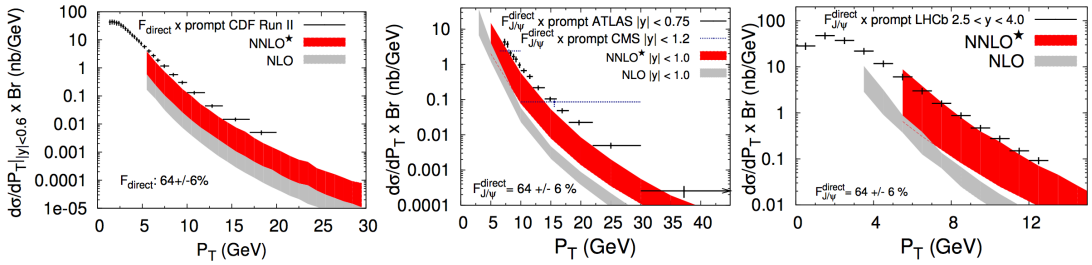

Figure 2.9: The J/ψ $d\sigma/dp_T \times Br$ measurements from CDF (left), ATLAS (middle), and LHCb (right). The prediction for CSM NLO and NNLO* is also shown in gray and read band [51].

It was the glory days for the color singlet model at low collision energy range [49]. All differential J/ψ cross-section measurements can well describe by CSM at low collision energies. The first deviation was shown in the first CDF measurement [50] of the direct production of the J/ψ at $\sqrt{s}$ =1.8 TeV, the discrepancy is that CSM prediction shows to be two order of magnitudes lower than measurement at the high-p_T range. Such a big difference has triggered the development of NRQCD approach, as well as the NLO and NNLO CSM correction study. Figure 2.9 [51] shows the direct J/ψ $d\sigma/dp_T$ measurements from CDF ($p+\bar{p}$) experiment [52] at $\sqrt{s} = 1.96$ TeV, ATLAS (p+p) experiment [53] as well as LHCb experiment [54] at $\sqrt{s} = 7$ TeV. The direct J/ψ fraction is extracted by CDF experiment and applied to ATLAS and LHCb's measurements. As aforementioned, the large correction at α_S^4 and α_S^5 in CSM is essential to understand the J/ψ transverse momentum spectra in high energy collisions. After taking the NLO and

Table 2.1: NLO fit results for prompt J/ψ NRQCD LDMEs.

LDMEs	Value
$\langle \mathcal{O}^{J/\psi}(^3S_1^{[1]}) \rangle$	$1.16/(2N_c)$ GeV^3
$\langle \mathcal{O}^{J/\psi}(^1S_0^{[8]}) \rangle$	0.089 ± 0.0098 GeV^3
$\langle \mathcal{O}^{J/\psi}(^1S_1^{[8]}) \rangle$	0.0030 ± 0.0012 GeV^3
$\langle \mathcal{O}^{J/\psi}(^3P_0^{[8]}) \rangle$	0.0056 ± 0.0021 GeV^3

NNLO* into account, the upper bound of CSM predictions is very close to the data at Tevatron and LHC energies. But one should notice that the NNLO calculations are not completed yet in this comparison, only channels with real-emission contributions were calculated [55], as noted by NNLO*.

The NRQCD approach was developed since the discrepancy discovered at CDF experiment. The full NLO NRQCD approach calculation was done in 2010. The LDMEs then were extracted by fitting CDF high p_T prompt J/ψ production data [56]. After assuming the charm quark mass be 1.5 GeV, the LDMEs was extracted from experiment data. The LDMEs is listed in Table 2.1.

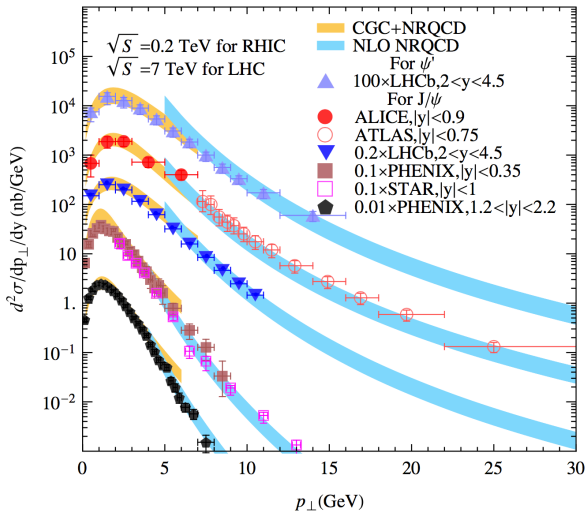

Figure 2.10: J/ψ and $\psi^{'}$ differential cross section as a function of p_T, measurements are from LHC and RHIC energy, NRQCD predictions and CGC+NRQCD predictions are shown in different collisions energy [36].

After applying these LDMEs to NRQCD approach, in Figure 2.10, cyan bars show the predictions from NLO NRQCD for RHIC and LHC energies [47, 53, 58–61]. One should notice that the measurements from different experiments are the inclusive J/ψ differential cross section. It includes component from decays of both B mesons and excited $c\bar{c}$ states, while the prediction from NRQCD and CGC+NRQCD only includes prompt J/ψ production contribution. The correction from B meson at high p_T range

needs additional consideration. It will contribute about 10% difference. With current measurements, the NRQCD [57] can reasonably describe all data points at high p_T range. At low p_T range, CGC+NRQCD predictions are also shown for the differential J/ψ cross section at different collision energies. The good agreement between measurements and the NRQCD predictions at high p_T range as well as low p_T range indicates that the $c\bar{c}$ hadronization can be well described by the LDMEs.

The LDMEs extracted from data has an universal property, thus LDMEs can be used in various collisions rather than only in hadroproduction at RHIC and LHC. Such LDMEs has been used to describe the J/ψ photoproductions at HERA [62], as well as in two-photon collisions measured at LEP [63].

2.3.3 Polarization measurements

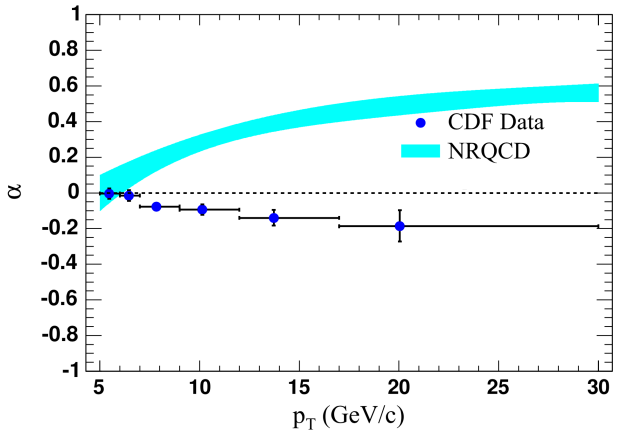

Figure 2.11: J/ψ polarization as a function of J/ψ p_T in $p\bar{p}$ collisions at $\sqrt{s}$ = 1.96 TeV at CDF experiment. The cyan band is J/ψ polarization from the leading order NQRCD factorization [65].

The success of NRQCD approach in predicting J/ψ cross section does not continue in the measurements of J/ψ polarization. Figure 2.11 shows the J/ψ polarization parameter α for prompt J/ψ production at CDF in Run II [64]. The leading order prompt J/ψ NRQCD prediction is also shown [65]. The LO NRQCD calculation included the contribution from $\psi(2S)$ and χ_c. The CDF measurement shows that the prompt J/ψ polarization becomes longitudinal as p_T increases, while LO NRQCD prediction gives a contrast trend. A transverse polarization is shown for NRQCD calculation at high p_T range. The NLO NRQCD J/ψ polarization calculation was carried out in [66]. However, the trend does not change much, a transversal polarization for J/ψ production at high p_T is still shown [66].

Leading order CSM also predicts a transverse polarization as p_T increases [67]. However, both NLO and NNLO* correction give a longitudinal polarization. As we mentioned, high p_T J/ψ productions are dominated by NLO and NNLO* corrections.

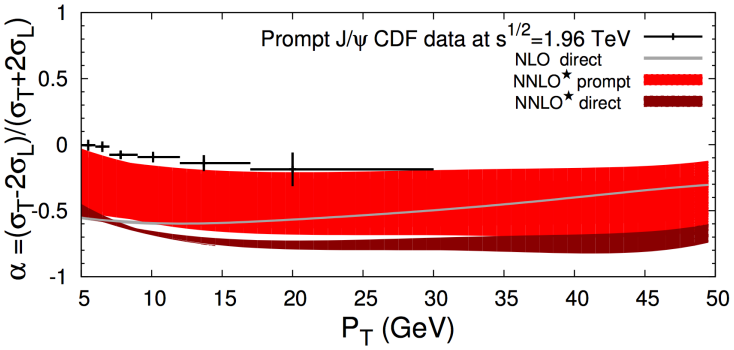

Figure 2.12: (Color online) J/ψ polarization as a function of J/ψ p_T in $p\bar{p}$ collisions at $\sqrt{s}$ = 1.96 TeV at CDF experiment. Predictions of prompt J/ψ polarization from CSM at LO, NLO, NNLO* are also shown. Direct J/ψ NNLO * polarization prediction is shown in thinner dark-red band.

Figure 2.12 shows the CSM predictions with different order of corrections. Similar to the cross section measurements, the upper band of CSM NNLO* predictions can touch the CDF measurement.

The J/ψ polarization at LHC and RHIC energies were also measured. The polarization parameter α are consistent with zero at LHC energies from different experiment [68–70]. At RHIC, both STAR [71] and PHENIX [72, 73] experiment measured the J/ψ polarization at proton-proton collisions at $\sqrt{s}$ =200 GeV. The J/ψ polarization is measured in the kinematic range of 0 < p_T <6 GeV/c. Measurement shows a longitudinal polarization with big uncertainties, and the NLO CSM can describe the date. The CSM prediction also have big uncertainties. Furthermore, the validation of perturbative calculation is also questionable at such a low p_T range.

2.4 J/ψ production at partonic level

In high energy proton-proton collisions, the proton can not be treated as a point like particle. The proton-proton collision can be understood as the overlap of the nucleon wave functions. The overlap range is affected by the impact parameter and the transverse spatial partonic distribution of proton. The production of $c\bar{c}$ pair is generally treated as a hard process due to the large mass of charm quark, which happens at the early stage of the collision and normally originates from a $2 \rightarrow 2$ parton-parton hard scattering. However, the detail scenario of the $c\bar{c}$ production is not very clear yet. Measurements have shown that hard parton-parton scattering is more likely happening in the central collisions (smaller impact parameter) [74, 75]. Furthermore, an early study from NA27 experiment in p+p collision at $\sqrt{s}$ = 27 GeV has shown that charged-particle multiplicity distribution in events with open charm produced has a mean value that is higher by $\sim$ 20% than the one without charm produced [76]. And events with open

charm produced has a soften momentum spectra. On the other hand, the number of final state charge particles is also affect by the impact parameter. The partonic distribution function fluctuation is another important factor that affect the charged particle production. There are two additional contributions to J/ψ production and its related multiplicity at high energy proton-proton collisions. The first one is the gluon radiation associated with the hard process at high energy and particle transverse momenta. The second one is the Multiple-Parton Interactions (MPI) for both soft and hard process. Hence, the measurement of the J/ψ production as a function of charged-particle multiplicity is of interested. It can provide insight into the process occurring in the collision at the partonic level and the interplay between the hard and soft mechanisms in particle production. .

The final-state particles produced in the hadronic collisions can be described in two-component approach: an initial hard partonic scattering process and an underlying event. The hard partonic scattering can be calculated in pQCD approach, while the calculation of underlying event, which including soft process and mini-jet with small transverse momenta, is based on phenomenological model. The properties of Jet and underlying event as a function of multiplicity have been studied at CMS Collaboration in pp collisions at $\sqrt{s}$ = 7 TeV [78, 79]. The MPI production scenario can well describe the data. Analysis at ALICE Collaboration shows that high multiplicity event is a result of high number of MPIs and a higher average number of fragments [80]. The gluon density fluctuations in proton is also advocated to describe the results at high multiplicity proton-proton collisions [81–83]. Indeed , the transverse structure of proton is of great importance in defining the underlying event structure and the probability MPIs. The LHCb Collaboration' measurement of double charm production in proton-proton collisions indicates that MPIs also play an important role in $c\bar{c}$ production [84, 85].

The first inclusive J/ψ production as a function of charged-particle multiplicity measurement was done by AlLICE Collaboration in pp collisions at $\sqrt{s}$ = 7 TeV at both mid-rapidity ($|y|$ < 0.9) and forward rapidity (2.5< y < 4.0) [77]. Both rapidity range observed an approximate linear increase of the relative yield of J/ψ with respect to the charged-particle multiplicity which varied between the multiplicity range of 0 to 4 times of the average multiplicity. And the results from these two rapidity ranges are consistent with each other, while Pythia 6 event generator with only $2 \rightarrow 2$ hard process gives a decrease trend prediction. The ALICE Collaboration also measured charm and beauty production at central rapidity versus charged-particle multiplicity in proton-proton collisions at $\sqrt{s}$ = 7 TeV [86]. They measured D meson, prompt J/ψ, as well as non-prompt J/ψ production as a function of charged-particle multiplicity. A faster than linear increase was observed at high multiplicity, and both D meson, prompt J/ψ and

non-prompt J/ψ show a similar increase trend, and no p_T dependence was shown. The similar trend between open charm and hidden charm indicates that the hadronization does not affect the non-linear trend. The average D-meson relative yield as a function of the relative charged-particle multiplicity is shown in Figure 2.13. Figure 2.14 shows the non-prompt J/ψ relative yield as a function of relative charged-particle multiplicity at central rapidity for $p_T > 0$ GeV/c.

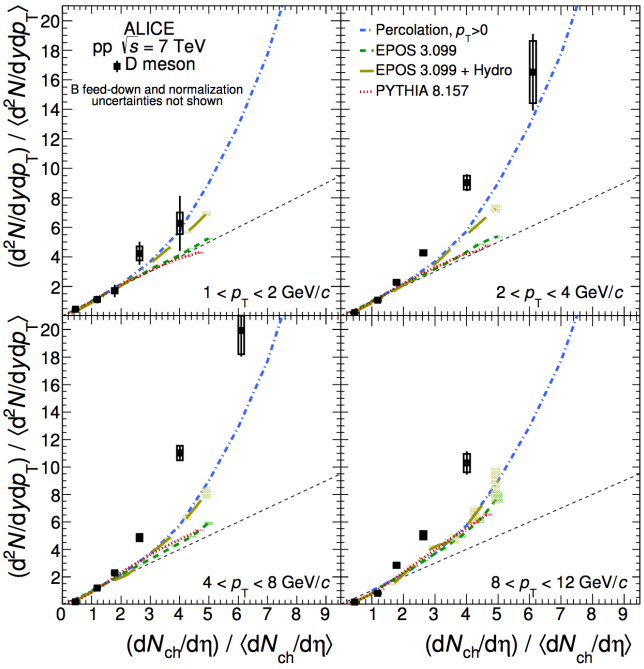

Figure 2.13: (Color online) Average D-meson relative yield as a function of the relative charged-particle multiplicity at central rapidity in different p_T intervals. Model calculations from PYTHIA 8.157, EPOS 3 with and without hydro and a p_T-integrated are also shown. The diagonal (dashed) line is shown to guid the eye.

At the LHC energies, the track densities at high multiplicity proton-proton events is comparable with collisions in Cu+Cu collisions at RHIC energies [87]. A collective expansion was observed for light hadrons in these heavy-ion collisions. This may bring the question: whether a small system has been created in the high multiplicity events? EPOS 3 [88, 89] is a event generator which assumes initial conditions followed by a hydrodynamical evolution. The collision initial conditions were obtained in the Gribov-Regge multiple scattering framework, which used the "Parton based Gribov-Regged" formalism. In EPOS 3, the individual scatterings are referred as Pomerons and are identified with parton ladders. The ladder is composed of a pQCD hard process with initial and final state radiation. While non-linear effects are considered by means of a saturation scale. The hadronisation is described by a string fragmentation procedure. A hydrodynamical evolution, then, is applied on the dense core of the collisions with

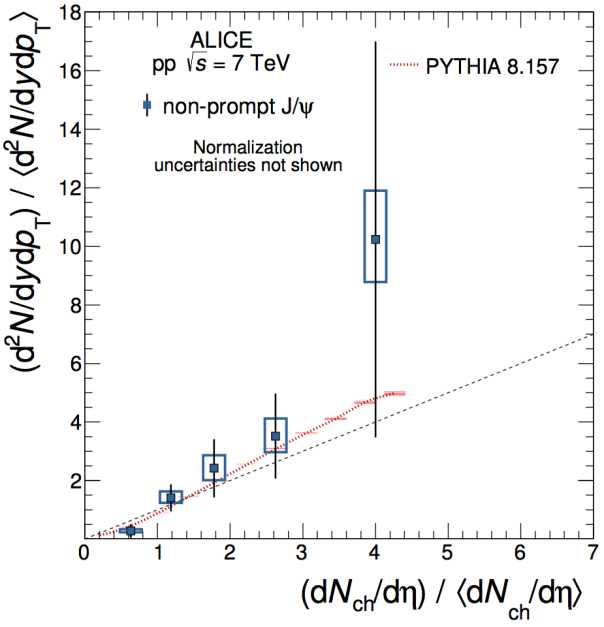

Figure 2.14: Non-prompt J/ψ relative yield as a function of the relative charged-particle multiplicity at central rapidity. PYTHIA 8.157 calculation for B mesons is shown in red band. The diagonal (dashed) line is shown to guid the eye.

initial condition obtained by using "Parton based Gribov-Regged" formalism. Simulation [90] has shown that at LHC energies the energy density is high enough to apply the hydrodynamic evolution. The EPOS event generator without hydrodynamic evolution gives a linear increase of D-meson production as a function of the charged-particle multiplicity. With hydrodynamic evolution involved, EPOS 3 predicte a strong than linear multiplicity dependence.

The percolation model [91] describes the high energy hadronic collisions by exchanging color sources between partons. The color sources are produced by parton collisions, it has a finite spatial extension and most important of all it can intact with each other. The size of color source is determined by the source's transverse mass. The soft sources will reduced due to larger size in high energy pp collisions, which introduce a reduce of total charged-particle multiplicity. While hard sources is less affected due to the smaller size. This color source shadowing effect also introduce stronger than linear increase of heavy flavour relative production yield with respect to the relative charged-particle multiplicity. In this scenario, at high-p_T range a stronger deviation from the linear expectation is expected.

A strong than liner increase of the relative heavy-flavour yields with respect to the relative charged-particle multiplicity was observed at the LHC energy of $\sqrt{s}$ = 7 TeV. The PYTHIA 8 which includeds MPI effect has shown an underestimation of the faster than linear trend at high multiplicity. The increase trend can be described by both EPOS

3 event generator with hydrodynamics and percolation model.

2.5 Discussion and thesis scope

Understanding J/ψ meson hadroproduction has been a long-term effort both experimentally and theoretically. However, none of the existing theoretical models can successfully describe both J/ψ transverse momentum (p_T) spectrum and the polarization. Furthermore, the composition of inclusive J/ψ is complicated, including direct production via gluon fusion, parton fragmentation, and feed-down from excited charmonium states and B hadrons. Measurements of J/ψ production at a different beam energy can shed new lights on the understanding of different J/ψ production mechanisms, and help to constrain model calculations.

The measurement of J/ψ production as a function of charged-particle multiplicity measurement could provide insight at the partonic level and the interplay between the hard and soft mechanisms in particle production. The J/ψ production is dominated by gluon fusion in both LHC and RHIC energies. However, due to huge collision energy difference, the x scale of the fusion gluon will be very different. Another difference is that the energy density at LHC is large enough to apply the hydridynamic evolution. At RHIC energies we are lack of this kind of simulation. However, the final-state particle density in p+p collision is at least one order of magnitude lower than that in the most peripheral Au+Au collisions which may indicate that hydridynamic evolution should not exist in pp collisions at RHIC energies. The study of J/ψ production as a function of charged-particle multiplicity at RHIC energy will shed light on both small system and the J/ψ production mechanism in detail.

In this thesis, we measured the J/ψ spectrum, $\psi(2S)$ to J/ψ yield ratio and the J/ψ production as a function of charged-particle multiplicity in proton-proton collisions at $\sqrt{s}$ = 500 GeV from the STAR experiment.

Chapter 3 Experimental Setup

3.1 Relativistic Heavy Ion Collider

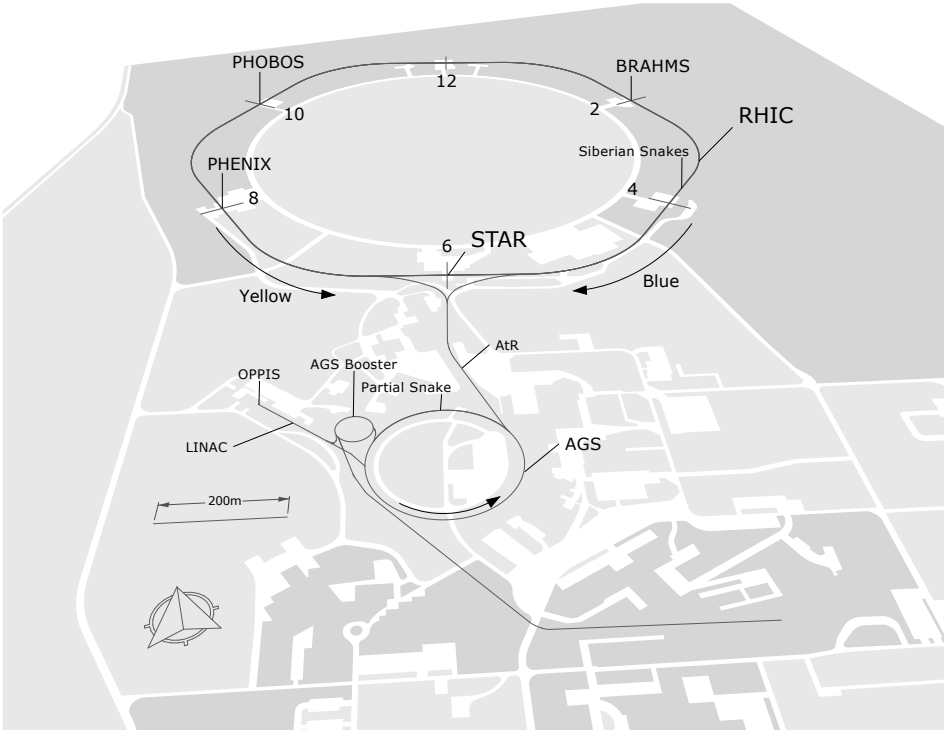

Figure 3.1: The Relativistic Heavy Ion Collider accelerator complex.

The Relativistic Heavy Ion Collider (RHIC) facility at the Brookhaven National Laboratory (BNL) is a circular accelerator. The layout of RHIC facility is shown in Figure 3.1. RHIC has the capability to collide a wide range of nuclei from proton to uranium. RHIC can operate unequal beam species such as protons on gold ions. RHIC is also the only existing collider which can operate the polarized protons. RHIC has two opposite directions store quasi-circular concentric rings, clock-wise and counter-clockwise, known as blue and yellow beams respectively. The circumference of each ring is 2.4-miles. Detectors are built at intersection point to detect final state particles produced in the collisions. In 2008, RHIC achieved the design values and an "Enhanced Design" parameters of RHIC performance objectives were formulated [92]. One of the "Enhanced Design" goals is to enhance the average luminosity to 150×10^{30} cm^{-2}s^{-1} in polarized proton and proton collisions at $\sqrt{s}$ = 500 GeV. In 2009, the average p+p luminosity was 55×10^{30} cm^{-2}s^{-1} and primarily with the longitudinally polarized beam at STAR collision point. In 2011, the luminosity increased 63% compared to 2009 and reached 90×10^{30} cm^{-2}s^{-2}. The polarization of the proton at STAR collision point was primary vertical polarization. In 2013, the goal of "Enhanced Design" luminosity was

achieved. The details of RHIC recent achievements and the future program can be found in [92].

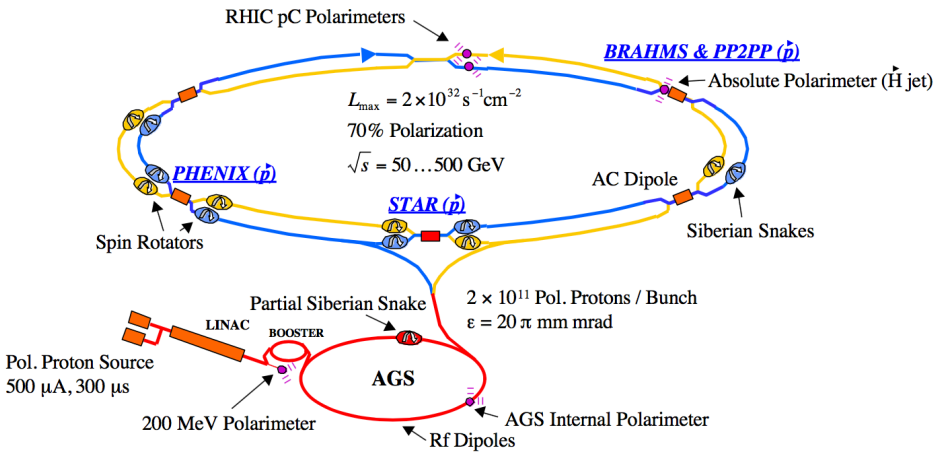

Figure 3.2: RHIC acceleration scenario for polarized beam [94].

Polarized proton accelerating at RHIC complex is consists of a long injector chain. RHIC uses an optically pumped polarized H^- source (OPPIS) [93] as the polarized ion source. OPPIS produces a 0.5 mA H^- ion current, about 9×10^{11} polarized H^-, with 80% polarization during 300 μs pulse. These H^- ions are accelerated to 200 MeV in the linear accelerator (LINAC) and then strip-injected into Booster Synchrotron. In the Booster, the H^- ions are captured in a single bunch which contains about 4×10^{11} polarized protons. After accelerated the polarized protons to 1.5 GeV in the Booster, protons are delivered to the Alternating Gradient Synchrotron (AGS). In the AGS, protons are accelerated to 25 GeV, then injected to RHIC through the AGS-to-RHIC transfer line. Once in RHIC, the protons are accelerated to 250 GeV and stored for collisions. Given the RF (Radiofrequency) cavity frequency and store ring circumference at RHIC, RHIC has 360 RF buckets. Not all RHIC Buckets are filled with bunches, every three buckets a bunch is filled. Experimentally only 109 bunches are filled in 2009 and 2011, anther 11 bunches positions are abort gap which used to form a gap in the circumference. The purpose of this gap is that in the dump process it takes a short but significant time to switch on the magnets which divert the beam from the RHIC into the dump. RHIC rings have six interaction points. The STAR experiment, the only experiment collaboration in operation now, located at 6 o'clock. PHENIX, at 8 o'clock, experiment decommissioned in 2016. The RHIC acceleration scenario for polarized beam can be found in Figure 3.2.

3.2 STAR Detector

The Solenoidal Tracker at RHIC (STAR) was designed to understand the microscopic structure of hadronic interactions at high energy. In order to accomplish this goal, STAR was designed to be a multi-purpose particle detector [95]. STAR has a large-acceptance with a full azimuthal coverage ($0 < \phi < 2\pi$) and a pseudo-rapidity range of $|\eta| < 1$, and the acceptance is effectively extended by sub-detectors at forward. With the large acceptance and the featuring detector system, STAR can measure many observables simultaneously to study signatures of quark-gluon plasma (QGP), high momentum particles from hard parton-parton scattering, and correlations. Figure 3.3 illustrates the STAR detector complex with various sub-detectors.

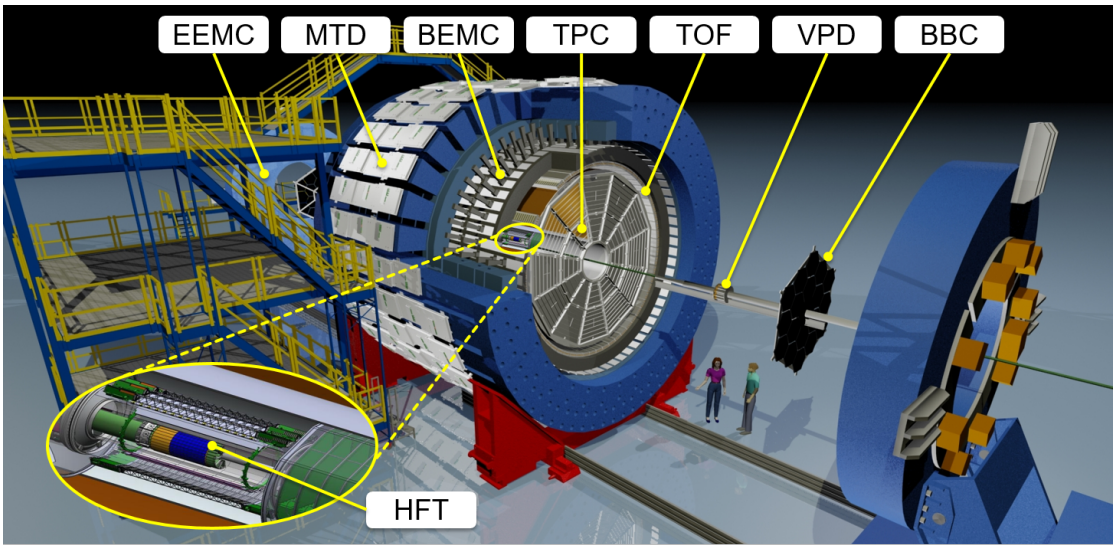

Figure 3.3: Perspective view of the STAR detector.

The innermost detector system at STAR is the Heavy Flavor Tracker (HFT) [96]. The HFT consists of three silicon sub-detectors: a silicon pixel detector (PXL), an intermediate silicon tracker (IST) and silicon strip detector (SSD). The purpose of HFT detector is to provide an excellent position resolution at the interaction point. This will resolve secondary particles and decay vertices from a primary vertex and primary tracks. The most inner sub-detector is PXL. It has two layers, each layer used a Monolithic Active Pixel Sensors (MAPS) technology, which makes the thickness of PXL down to 50 μm. By using MAPS technology, the total radiation length $X/X0$ is as little as 0.4% per layer. And the detector is placed as close as 2.5 cm to the interaction point to achieve a good resolution. The IST is placed next to PXL in radial direction. It has an position resolution of 170 μm in the $r \times \phi$ direction and 1.8 mm in the z direction. The IST is used to match the high resolution of PXL and courser resolution from TPC and SSD. The outermost HFT detector is SSD. The position resolution of SSD is 20 μm in the

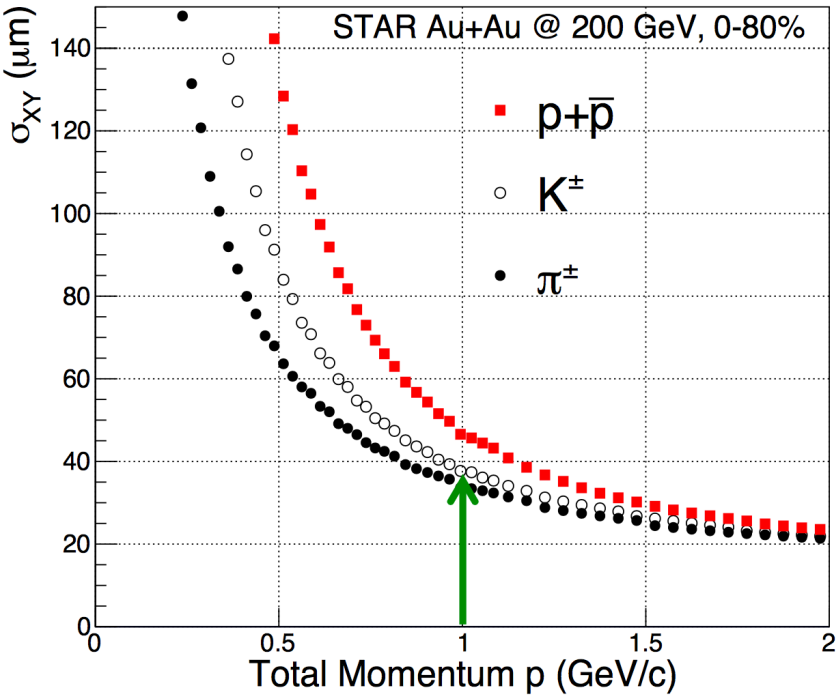

Figure 3.4: Track pointing resolution along transverse direction as a function of the particle momentum.

$r \times \phi$ direction and 740 μm in the z direction. Figure 3.4 shows the hadron's distance of closest approach resolution achieved by using HFT in 2014 Au + Au collisions. For Kaons instance, with $p_T > 1$ GeV/c, the spatial resolution in $X - Y$ plane will less than 40 μm. The HFT started its service at 2014 and retired at 2016. It collected $\sim$1.2 billion minimum-bias events in 2014 Au + Au collisions, $\sim$1 billion p + p events, $\sim$0.6 billion p + Au events in 2015 and $\sim$2.0 billion minimum-bias events in 2016 Au + Au collisions.

STAR core tracking detector Time Projection Chamber (TPC) [97] is located outside of the HFT detectors. TPC is a cylindric detector with an inner radius of 50 cm and outer radius of 200 cm. The acceptance is $|\eta| < 1.8$ in the pseudo-rapidity range and 2π in azimuth. TPC is used to do particle tracking, momentum determination, and energy loss measurement at STAR. The details of TPC detector will be discussed in the next section. The Time-of-Flight (TOF) [98] is next to TPC, which covers $|\eta| <$ 0.9 and a full azimuthal acceptance. TOF detector has an intrinsic timing resolution < 80 ps which makes it vary suit to measure charged particle flight time. In p+p collisions, the luminosity is about 10^{32} cm^{-2}s^{-1} and the TPC recording time is about 40 μs, then hundreds of events will record from different branch crossing. Such a good intrinsic timing resolution of TOF detector enable it to reject pile-up tracks from other branch crossings. The Barrel ElectroMagnetic Calorimeter (BEMC) [99] is just behind

the TOF detectors. It covers $|\eta| < 1$ with complete azimuthal symmetry. BEMC measures energy deposition in the calorimeter. It served as a rare event trigger to measure high transverse momentum electrons and high energy photons. The BEMC is one of the main detector used in this analysis, a detail describe and discussion can be found in section 3.2.2. Following the BEMC is the STAR magnet system. The STAR magnet is a room temperature solenoidal magnet. It can be operated at full field ($|B_z|$ = 0.5 T) and half full field. The outermost detector at STAR is the Muon Telescope Detector (MTD) [100], which is used to measure muons from collisions. BEMC, magnet coils, and steel stop most of the hadron produced in collisions while muon can easily reach MTD due to low interaction cross-section. MTD covers ∼45% in azimuth and $|\eta| <$ 0.5. MTD was fully installed in 2014. About 14.2 nb^{-1} Au+Au events were collected in 2014 by using MTD di-muon trigger. Figure 3.5 shows di-muon invariant mass distribution. Compared to di-electron channel, the muon is less effect by bremsstrahlung energy losses in detector material. This gives the advantage to study different Upsilon states.

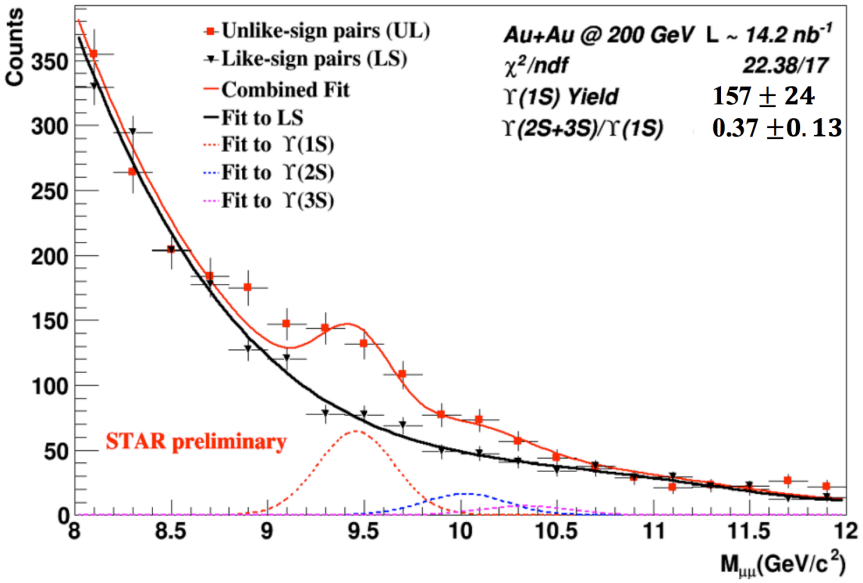

Figure 3.5: Invariant mass distribution in 2014 Au+Au collisions.

There are three trigger detectors at forward direction: Beam Beam Counter (BBC), Vertex Position Detector (VPD), Zero Degree Calorimeter (ZDC) [101–103]. The BBC detector is installed around the RHIC beam pipe on the EAST and WEST side of STAR with a pseudo-rapidity range of $3.4 < \eta < 5.0$. Each side consists of four scintillator annuli and is 3.75 meters from the center of STAR. BBC trigger is defined as a prompt coincidence between fires in both sides. The BBC trigger defines a minimum bias trigger, the triggered cross section for p+p collision at $\sqrt{s}$ = 200 GeV is ∼26.1mb. The corresponding detector efficiency is 87% on none single diffractive events. The VPD

has two identical detector assemblies on both east and west side of STAR with a pseudo-rapidity range of $4.24 < |\eta| < 5.1$. Each VPD assembly consists of nineteen units, only 16 units are used as STAR trigger detector. The VPD has been integrated into trigger system, it provides the primary detector input to the minimum bias trigger in A+A collision. With the precise timing information from VPD, it can be used to measure the location of the primary vertex along beam pipe and provides event "start time" for TOF and MTD systems to perform particle identification at mid-rapidity. The Zero Degree Calorimeter are mainly used in heavy ion collisions. It is used to detect neutrons emitted by ions. The neutrons beam fragments dominate the range of $\theta < 4\ mr$ along beam directions. The coincidence of such a 'zero degree' range from ZDC is a minimal bias selection of heavy ion collisions. Thus ZDC is used as an event trigger and a luminosity monitor both at STAR and PHINEX. The main detector used in this analysis are TPC, BEMC, and TOF. The details of these sub-detectors are described in the following sections.

3.2.1 Time Projection Chamber

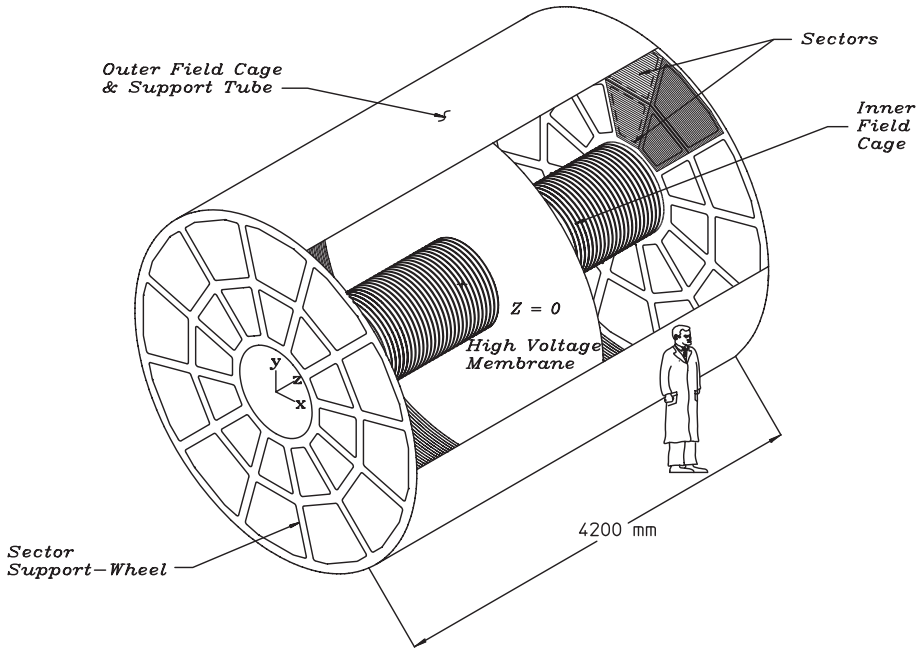

Figure 3.6: The schematics of the STAR TPC [97].

The Time Projection Chamber (TPC) is the primary tracking detector at STAR experiment, which covers a pseudo-rapidity range of $|\eta|$<1.8 and a full azimuthal angle [97]. Figure 3.6 shows TPC structure. The TPC is 4.2 m long and the outer and

inner diameters are 4 m and 1 m, separately. It sits inside a 0.5 T solenoidal magnet. The TPC volume is filled by P10 gas (10% methane, 90% argon) at 2 $m$bar above atmospheric pressure and holds a uniform electric field of $\sim$135 V/cm. The uniform electric field in the TPC is provided by a thin conductive Central Membrane (CM), concentric field-cage cylinders, and the readout end caps. The central membrane is operated at -28 kV and the end caps are at ground potential. The field-cage cylinders provide a uniform gradient between the central membrane and grounded end caps. The drift velocity is about 5.45 cm/μs inside the TPC, which leads to a maximum drift time in the TPC of $\sim$ 40 μs. After a maximum 2.1 m drifting under 0.5 T magnetic field, the electrons cluster diffusion in transverse is about σ_T = 3.3 mm and σ_L = 5.2 mm in longitudinal direction. The longitudinal diffusion width sets the scale of tracking system resolution in the drift direction.

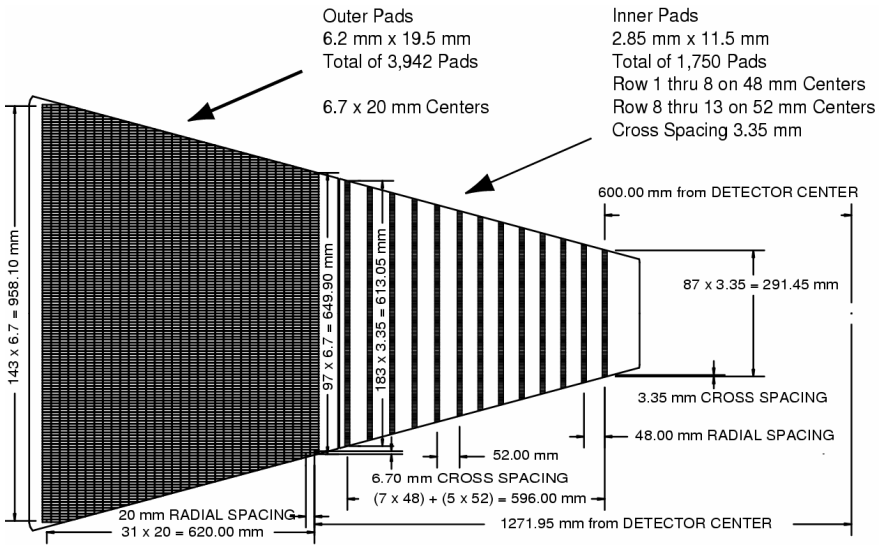

Figure 3.7: The anode pad plane with one full sector shown. The inner sub-sector is on the right and it has small pads arranged in widely spaced rows. The outer sub-sector is on the left and it is densely packed with larger pads.

The end-cap readout planes of STAR is based on Multi-Wire Proportional Chambers (MWPC) with readout pads. 12 MWPC modules are mounted as a clock on both east and west side of TPC. Each MWPC module consists of four components: a pad plane and three wire planes. The anode wire direction is chosen to best determine the momentum of the highest particle's transverse momentum (p_T) which track is nearly straight in radial lines. The drifting electrons avalanche in the high field at the 20 μm of anode wires providing an amplification of 1000-3000. The positive ions created in the avalanche could induce a temporary image charge on the pads. The pad plane is shown in Fig. 3.7. Each module has 45 pad rows and can be divided into the outer (32 pad rows) and inner (12 pad rows) sub-sectors. The outer sub-sector has continuous

pad coverage to optimize the dE/dx resolution and tracking resolution. The continuous pad coverage can collect full track ionization signal and more ionization electrons which improve dE/dx measurement statistics. The tracking resolution is improved due to anti-correlation errors between pad rows. The inner sub-sectors are in the region which has the highest track density and thus are optimized for good two-hit resolution. For inner sub-sectors, it uses smaller pads and the pad plane to anode wire spacing is reduced accordingly. The TPC readout system details can be found at [104].

A track passing through the TPC is reconstructed by finding corresponding ionization clusters along the path. The ionization cluster spatial positions are measured by pad row in $x - y$ plane and by drifting time of the ionization cluster in the z direction. To have a more precise measurement in the z direction, the cathode voltage is set to make sure that the electron has a peak drift velocity. Operating on this peak velocity makes it insensitive to temperature and pressure fluctuations, which can provide a precision of 0.1% on drift velocity. Various factors could distort the reconstructed position of the spatial hits. In the pad plane, the non-uniformities and global misalignments in the electric and magnetic could cause a millimeter-scale distortion. These distortions are important as it will affect the transverse momentum determination especially at high p_T. The correction of distortions and its origin can be found in [105]. The tracking algorithm is developed to associate spatial points to form tracks and extract physics information from reconstructed tracks, such as particle's momentum. The STAR track model is, to first order, a helix, where the magnitude of the curvature reflects the transverse momentum of the charged particle and the direction of the curvature decides the charge of the particle. However, some other effects such as energy lost in the P10 gas can cause particle trajectory deviation from the helix. STAR uses canonical Kalman filter [106] to determine track parameters and reconstruct tracks from hits in TPC.

Charged particle tracking efficiency depends on the acceptance of the detector, the electronics detection efficiency, as well as the two-hit separation capability of the system. A maximum of 45 hits is used for track reconstruction. Particle with different pseudo-rapidity will have different possible maximum hits. Then, particle's pseudo-rapidity will affect its tracking efficiency. The spaces between sectors, mounted wires, is anther contributor to tracking inefficiency. At 2008, the RHIC p+p luminosity was increased by a factor of 4. After that, the luminosity was increased even more. The hit merging effect becomes important in tracking. The tracking efficiency for pion is about 75% in 2011 p+p 500 GeV collisions while in 2009 the efficiency is about 80%. The transverse momentum of particles is determined by fitting a circle through the x, y coordinates of the vertex and the points along the track. The momentum resolution of primary track in p+p collisions is approximately $\Delta p_T/p_T \sim 1\% + 0.5\% \times p_T$. Charged

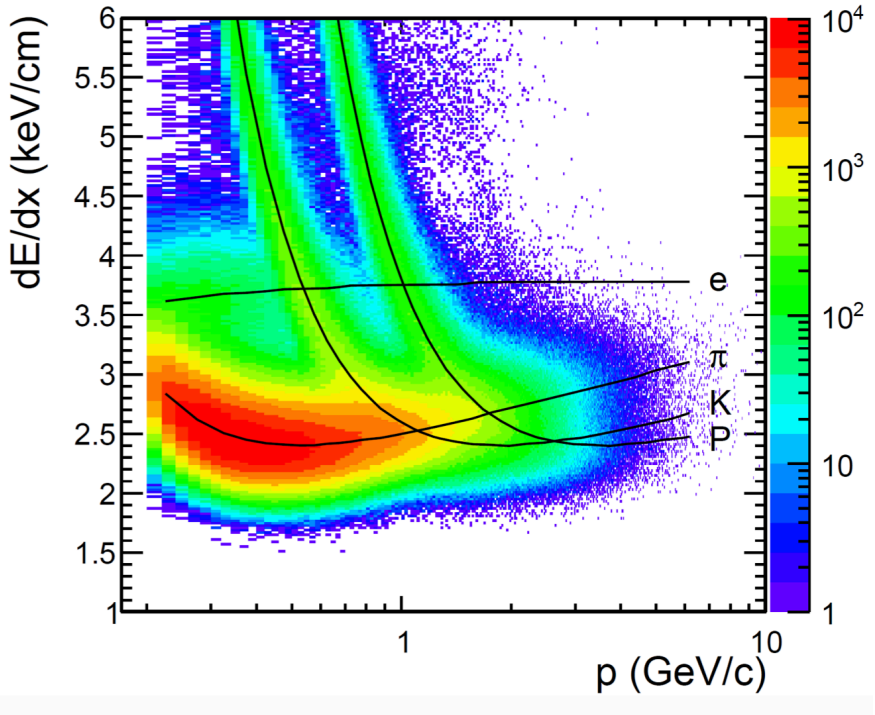

Figure 3.8: The dE/dx distribution in TPC as a function of momentum in p+p collisions for different particle species. the expected curves are calculated from Bichsel functions.

particle's energy loss (dE/dx) in TPC can well describe by Bichsel function [107]. The mass dependence of energy loss is well separated with velocities $v > 0.7$c. The dE/dx is extracted from the energy loss measured on 32 outer pad rows. The path length of a particle's in the TPC is too short to average out ionizations fluctuations [107]. Instead of measurement on the average dE/dx, the most probable energy loss is measured. The most probable energy loss is measured by removing a given fraction (typically 30%) of the largest ionization clusters. Figure 3.8 shows the dE/dx of different charged particles as a function of momentum in p+p collisions. The dE/dx theoretical curve from the Bichsel functions for different charge particles in the TPC is also shown.

3.2.2 Barrel Electromagnetic Calorimeter (BEMC)

The Barrel Electromagnetic Calorimeter (BEMC) [99] at STAR is a lead-scintillator sampling calorimeter. The BEMC detector covers $|\eta| < 1$ and 2π in azimuthal angle and is placed inside the aluminum coil of STAR solenoid. The inner surface of the BEMC has a radius of 220 cm and is parallel to the beam axis. BEMC includes a total of 120 calorimeter modules, each subtending 6^o in $\Delta\phi$ (~ 0.1 rad) and 1.0 unit in $\Delta\eta$. Module is segmented into 40 towers, each tower covers $\Delta\eta \times \Delta\phi = 0.05 \times 0.05$. Each of these towers is projective and point back to the center of the TPC. Figure 3.9 shows a schematic side view of a module illustrating the projective nature of the towers

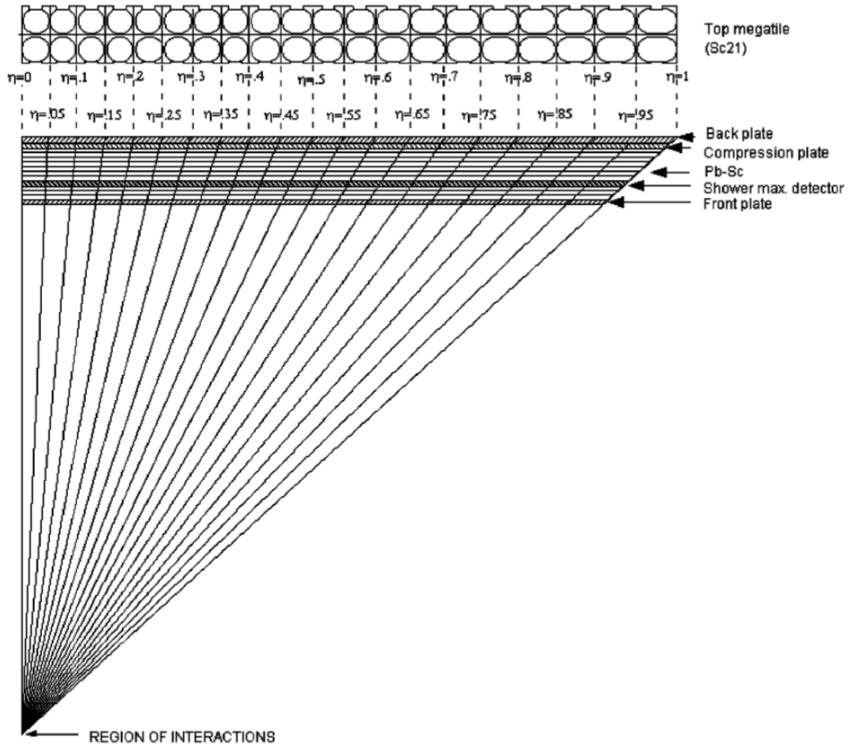

Figure 3.9: Side view of a calorimeter module showing the projective nature of the towers. The 21st mega-tile layer is also shown in plan view.

in the η direction. BEMC module consists of 21 layer scintillator and 20 layers of 5 mm thick lead. The lead layers are sandwiched by the scintillators. Among 21 layers of scintillators, 2 layers of 6 mm thick scintillator is used in the pre-shower detector, other scintillators are 5 mm thick. The scintillator's active material is Kuraray SCSN81.

Each scintillator layer is machined in the form of 'megatile' sheets and it has 40 optically isolated 'tile' corresponding to 40 towers in each module. Each tile has been machined a 'σ-groove' for signal readout. The signal from each scintillating tile is read out by a wavelength shifting (WLS) fiber which embedded in the 'σ-groove'. The optical isolation between different tiles is achieved by machining 95% of the way through scintillator and backfilling the resulting groove with opaque, silicon dioxide loaded epoxy. A black line is painted between the isolation grooves on the uncut scintillator surface. This black line will reduce the potential optical cross to the level of < 0.5%. The photomultiplier tubes used for the EMC towers are Electron Tube Inc. model 9125B with nearly 25% quantum efficiency at peak sensitivity and a mean quantum efficiency of 13.3%.

Shower maximum detector (SMD) is placed at 5.6 radiation lengths depth in the calorimeter modules at $\eta = 0$. It is used to measure the developed shower size. STAR SMD is a wire proportional counter with a double sided strip readout system. Strips

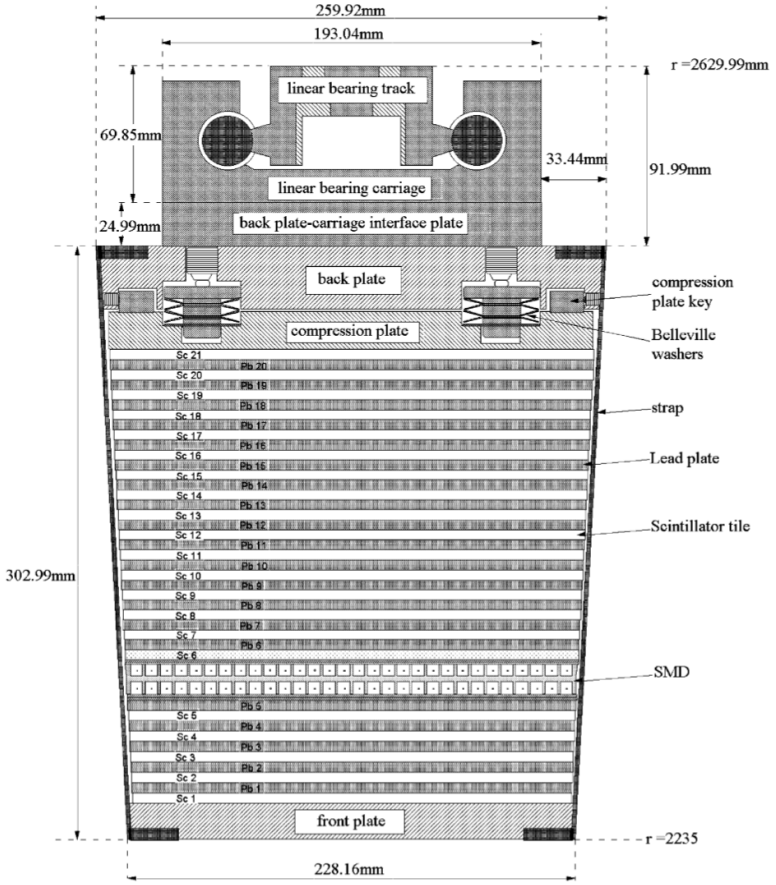

Figure 3.10: Side view of a STAR BEMC module showing the mechanical assembly including the compression components and the rail mounting system. Shown is the location of the two layers of shower maximum detector at a depth of approximately 5X0 from the front face at $\eta = 0$.

measure the induced charge from the charge amplification near wire in both perpendicular and parallel direction. The perpendicular strips has a size of 0.1 rad in ϕ and 0.0064 in η while 0.1 units in η and 1.33 cm wide for parallel strips. The SMD has an approximately linear response with energy from 0.5 to 5 GeV. The ionization for back plane is about 10% lower than the from plane. The energy resolution in the front plant is given approximately by $\sigma/E = 12\% + 86\%/\sqrt{E}$ [GeV]. The back plane energy resolution is 3-4% worse. The spatial resolution from front and back planes are given approximately by $\sigma_{front}(mm) = 2.4mm + 5.6mm/\sqrt{E}$ [GeV] and $\sigma_{back}(mm) = 3.2mm + 5.8mm/\sqrt{E}$ [GeV]. Figure 3.10 shows the side view of a STAR BEMC module. The mechanical assembly including the compression components and the rail mounting system.

3.2.3 Time of Flight

The Time of Flight detector [98] is a full acceptance time-of-flight system, which matchs the acceptance of TPC and BEMC. It consists of 120 trays, with 60 trays in both east and west side. Each tray has 32 single-end readout MRPC modules. Figure 3.11 shows two side views of a MRPC module. The MRPC module has an active size of 61 $\times$ 200 mm^2 with 6 readout pads in each module. Each pad has an area of 63 $\times$ 31.5 mm^2. MRPC is basically 7 floating resistive plates (glass) divided into 6 uniform gas gaps by nylon monofilament fishing line. Electrodes are applied to the outer surface of the outer plates which will provide a strong electric field in each sub-gap. All internal plates are electrically floating. Charged particle going through the chamber will generate avalanches in the gas gaps. Glass plates, a resistive material with $\sim 10^{12}\ \Omega/cm$, is transparent to the charge induction from avalanches in each gaps. The beam test at CERN PS-T10 test beam facility shown a 65 ps time resolution and greater than 95% detection efficiency for MRPCs by using 7 GeV/c pion beam [108, 110]. TOF system

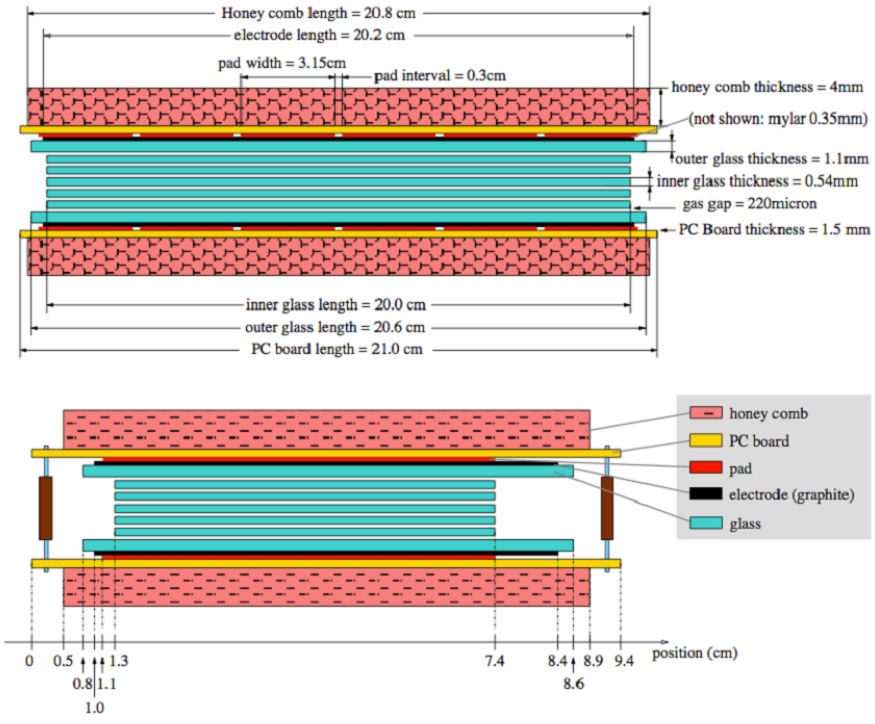

Figure 3.11: Two side views of MRPC [98]. The upper is for long side view and the lower is for short side view.

measures time intervals between two detectors - an event "start" time from VPD and a charged particle "stop" time from TOF detector. The start and stop time digitization are performed in the same electronics. Each of this two detectors has specific resolution on particle arrival times. The TOF time resolution is about $<$ 80 ps. The start time resolution from VPD has an collision energy and collision species dependence. The resolution

goes like $\sim \sigma_0/\sqrt{M}$. M is the total number of VPD tubes lit by prompt particles in an event. In Au+Au $\sqrt{s_{NN}}$ =200 GeV, the VPD resolution is 20-30 ps. In p+p collisions, the VPD start time resolution is approximately 80 ps [102].

The measured time intervals from VPD and TOF are associated with TPC tracks. By combine the TPC information (momentum and path length) and TOF information (Δt), the particle's inverse velocity can be given by

$$1/\beta = c\Delta t/s \tag{3.1}$$

Then the particle mass is

$$M = p\sqrt{(1/\beta)^2 - 1} \tag{3.2}$$

The TOF system significantly improves the particle identification capability. Figure 3.12 shows the m^2 distribution as a function of particle momentum measured by TOF in p+p collisions at $\sqrt{s}$ = 500 GeV. Pion, Kaon and Proton band are clearly shown. The π/K separation momentum range is extended to ~1.7 GeV/c and $(\pi, K)/p$ separation is extended to ~3 GeV/c [111]. With such a good time resolution from TOF system ($\sim$ 113 ps), TOF is very useful for pile-up track rejection. Thus in the year of 2012, The TOF matched track was implement in Pile-Up Proof Vertex (PPV) finding algorithm, which will be discussed in details in section 4.4.1.

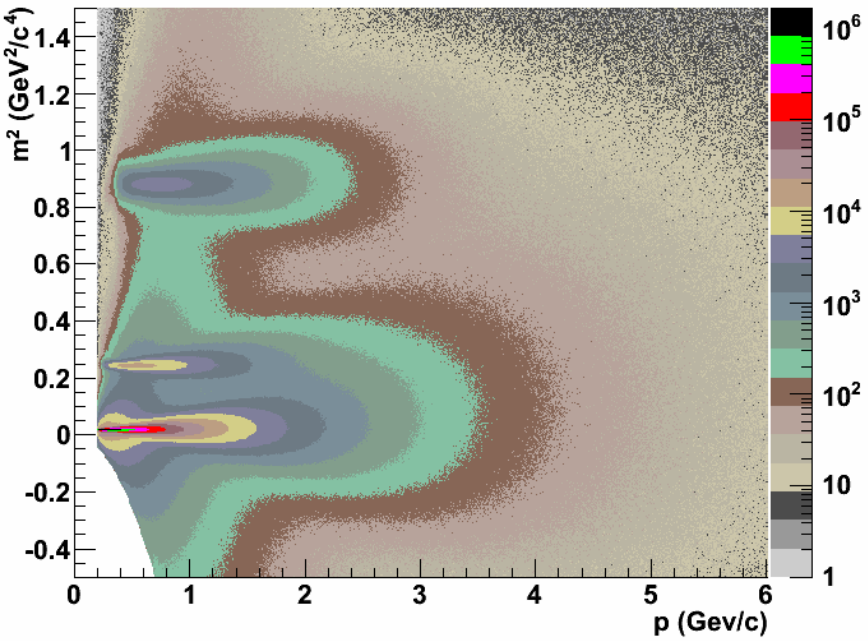

Figure 3.12: m^2 distribution as a function of momentum in p + p collisions at $\sqrt{s}$ = 500 GeV.

Chapter 4 Data analysis

4.1 Analysis overview

There are three analysis related to J/ψ meson in this chapter. The first one is the measurement of J/ψ cross section as a function of J/ψ transverse momentum. The second measurement is the invariant yield ratio of $\psi(2S)$ over J/ψ meson. The third measurement is the J/ψ relative yield as a function of relative charged-particle multiplicity, which is also be called J/ψ versus event activity in the following section. All these three measurements are using the same data sample for J/ψ reconstruction, which was taken in proton-proton collisions at $\sqrt{s}$ =500 GeV by STAR experiment at RHIC in 2011(Run11). The online event sampling criterion is defined by a High Tower (HT) triggered in Run11 trigger setup, which requires the deposit energy in a single BEMC tower is larger than 4.3 GeV. Another data sample which is triggered by BBCMB trigger in 2009 (Run09) is also used in the J/ψ versus event activity study. This data sample was taken in a low luminosity run which is about 40 times lower than J/ψ data sample taken in Run11. The Run09 data sample is used to measure the charge-particle multiplicity distribution in MB event, which is essential to the J/ψ versus event activity study.

The measured J/ψ signals are inclusive J/ψs which contain the feed-down contributions from excited charmonium states and B meson. The J/ψ has a short lifetime of $7 \times 10^{-21} s$ and the decay width is 92.9 $\pm$ 2.8 keV. As mentioned, J/ψ has a relative larger branch ratio decay to leptons. The decay branching ratio of $J/\psi \rightarrow e^- e^+$ channel is 5.95% $\pm$ 0.06%. This di-electron channel is used in the J/ψ reconstruction in this analysis.

TPC and BEMC are detectors help to identify electrons. Two different electron/positron samples are defined: "EMC + TPC" electron and "TPC" electron. "EMC + TPC" electrons are electrons that fired HT trigger. "TPC" electrons are electrons which have a relatively low energy. Both electrons are selected from primary tracks. The J/ψ is reconstructed by combining the electron and positron in the same event. The combinatorial background is estimated by the like-sign method. The residual background is defined by an exponential function. Efficiency and acceptance correction for electrons and J/ψ in this analysis are estimated by embedding technique. Some other efficiencies like the nσ_e cuts efficiency and $nDedx$ cut efficiency are extracted by using a data-driven method. The $\psi(2S)$ analysis used the same method as J/ψ.

The J/ψ versus event activity study is started with vertex investigation. Vertex investigation describes the vertex finding algorithm used in STAR experiment. By using ranking larger than 0 cut on a vertex, it potentially requires two or more tracks at mid-

rapidity range. The characterization of event activity in a pile-up rich event is studied by comparing the primary track distribution and the TOF matched primary track distribution as a function of BBC coincidence rate. The TOF matched primary track is selected to characterized the event activity as it is much insensitive to the collision rate. The signal charge hadron tracking efficiency is also obtained by using embedding technique. The TOF matched track multiplicity efficiency and tracking efficiency correction are done by unfolding method. The secondary particle from weak decay is also studied by using PYTHIA simulation. The BBCMB trigger efficiency and vertex finding efficiency as a function of charged-particle multiplicity is studied in the Pythia6+starsim simulation frame.

4.2 J/ψ analysis

4.2.1 Dataset and Trigger

The dataset used in this analysis was taken in proton-proton collisions at $\sqrt{s}$ = 500 GeV in Run11. In Run11, the instantaneous luminosity is high, as indicated in BBC coincidence rate ($\sim$2 MHz). While the total J/ψ production cross section in an inelastic proton-proton collision has a relatively low total cross section ($\sigma_{J/\psi}$ $\sim$nb) [112]. Hence, most of the event are of not interested events in this analysis. Furthermore, TPC has a finite sampling rate of 1000Hz. We are interested in events with a high energy electron, which may decay from a high p_T J/ψ. Thus BHT1 trigger is employed to sampling events with a larger energy deposited in the BEMC and helps to sampling as much luminosity as possible in high instantaneous luminosity runs. The BHT1 trigger is defined as energy deposited in a single BEMC tower with E_T > 4.3 GeV.

In Run11, 154M BHT1 triggered events were recorded, it is equivalent to 22 pb^{-1} sampled luminosity. The trigger name, trigger definition and sampled luminosity are listed in Table 4.1. VPDMB trigger details are also shown in the table to illustrate the BHT1 enhancement on recording luminosity. The VPDMB trigger is a minimum-bias trigger which requires at least one hit on both east and west side of VPD. Huge enhancement on recording events respected to the sampled luminosity ratio in BHT1 trigger is obtained. Due to the bandwidth limitation assigned to the BHT1 trigger in Run11, a pre-scaler technology was applied to data taking system at the end of Run11, which requires every two of BHT1 triggered events only one event is recorded. The Run11 BHT1 triggered dataset was produced in the production series P11id using SL11d library. Figure 4.1 is the BHT1 sampled luminosity as a function of time.

Table 4.1: Run11 proton-proton collisions at $\sqrt{s}$ = 500GeV BHT1 and VPDMB trigger details

Trigger Name	Trigger Description	Number of Events	Sampled Luminosity
BHT1	$E_T^{TOW} > 4.3$ GeV	154M	22 pb^{-1}
VPDMB	hits on both sides	106M	0.011 pb^{-1}

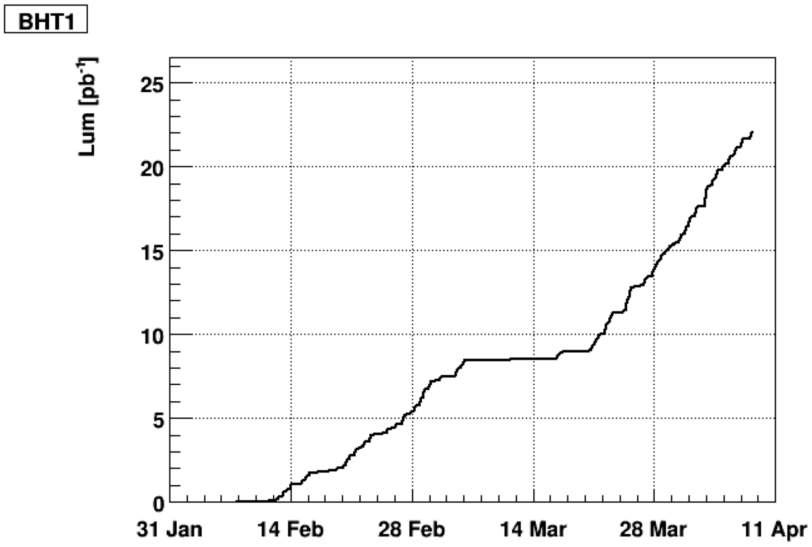

Figure 4.1: BHT1 sampling luminosity as a function of time in proton-proton collisions at $\sqrt{s}$ = 500 GeV in Run11.

4.2.2 Event Selection

The importance of the vertex-finding algorithm to find a real trigger event is self-evident. In p+p collisions, the low charged-particle multiplicity and high luminosity, which results in a pile-up rich event, all set obstacle to finding the truth vertex. The charged-particle multiplicity of the primary vertex can be found in the left panel of Figure 4.2. The charged-particle multiplicity is measured by counting the number of primary tracks in the pseudo-rapidity range of $|\eta| \leq 0.5$ with basic track quality cuts. However, one should notice that this multiplicity has lots of pile-up tracks involved despite named as primary track.

A PPV vertex finer (Pile-up Protected Vertex finder) is used to find the most probable vertex in the recorded event. The PPV gives the z position of a vertex. The x and y value of the vertex are given by the beam-line constraint, which is calculated by fitting high multiplicity events with Minuit VF method. This beam-line constraint will obtain the relationship among x, y, and z. The details of this vertex finding algorithm will be discussed in later section. The beam line is clearly shown in the right panel of Figure 4.2 in Run11 data. The big shift on the beam line is due to changing of beam line during

Table 4.2: Event selection criterions

Event Cut Parameters	Cut Value
Valid vertex	$V_x^{TPC} > 10^{-5}$ or $V_y^{TPC} > 10^{-5}$ or $V_z^{TPC} > 10^{-5}$ cm
V_z	$\|V_z^{TPC}\| < 200$ cm

Run11.

The PPV method can reconstruct vertex with very high accuracy especially for BHT1 J/ψ events which has a very high-p_T electron or positron [113]. A valid vertex requirement is applied to every BHT1 triggered events in this analysis, which requires 3 components of the reconstructed vertex positions not simultaneously less than 10^{-5} cm. Figure 4.3 shows the primary vertex V_z distribution. In the J/ψ transverse momentum spectrum measurement, we only required the reconstructed vertex be in the TPC to maximize the J/ψ statistics. The cuts on event level in the BHT1 trigger J/ψ cross section measurement are summarized it Table 4.2.

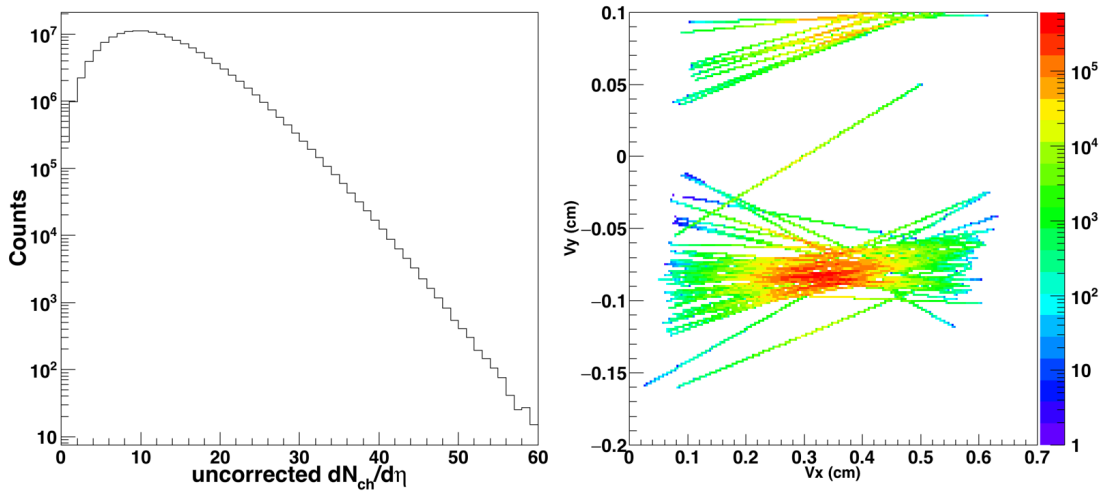

Figure 4.2: Left: uncorrected charged-particle multiplicity distribution, Right: primary vertex V_x verse V_y distribution

4.2.3 Track Selection

There are two categories of tracks: primary track and global track. The difference between global track and the primary track is that on top of the global track, the primary track has been associated with a vertex and the momentum of the primary has been recalculated by adding the vertex in the fitting. As mentioned in the TPC detector, TPC can provide a maximum of 45 hits measurement for a track that passing through the TPC. All these measured hits are used to reconstruct track and calculate the track's transverse

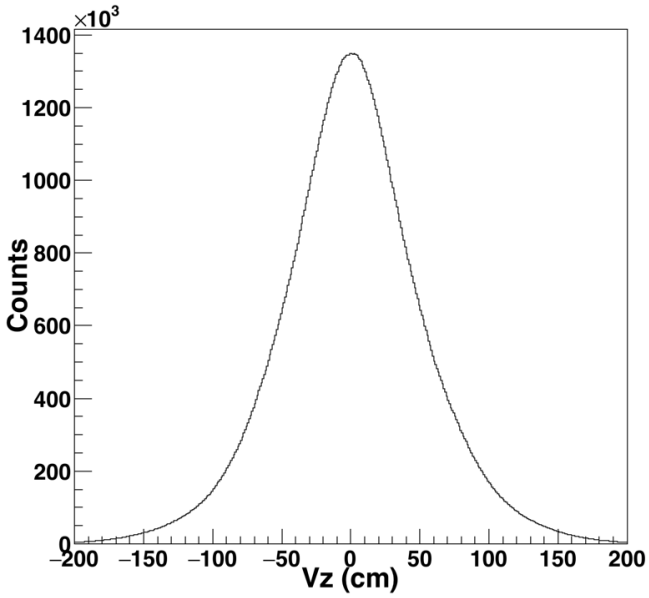

Figure 4.3: Primary vertex V_z distribution.

momentum. Thus the global track has a maximum of 45 hits, while this number becomes 46 for primary track if taking the vertex as another independent measurement. Primary track is used in this analysis. In the follow section, if no special notification, the track means primary track. Several considerations are placed on the reconstructed track to ensure it is the track of interested. A minimum requirement of 25 number of reconstruction hit points (nHitsFit) for each track is used to ensure the reconstruction of the track without track splitting effect. Particle ionization energy loss per unit length (dE/dx) is calculated by using outer pad rows of energy deposition information, thus, a minimum of 15 number of dE/dx hit points (nHitsDedx) is required to make sure that dE/dx has a good resolution. The TPC acceptance requires each track should in the η range of $|\eta| < 1$.

There is another track quality requirement, which is the distance of closest approach (DCA) to the event primary vertex of its associated global track. We actually more interesting in primary tracks with a small DCA value since J/ψ has a very small decay length. In this analysis, the DCA selection has following considerations:1) reject pile-up track, Run11 data was taken in a pile-up rich environment, 2) reject the tracks from long decay length particle, such as K_s, λ, and etc, 3) tracks from differ primary vertex. Furthermore, tracks that fired BTOW or could match with BEMC would have a relative higher transverse momentum, thus the multi-scatting effect would have less effect on it as it goes through the detector. All these considerations require a small DCA value. However, the first TPC measured point is at least 50 cm away from the event primary vertex, this constrain the DCA resolution at about one-centimeter order.

Different DCA cuts are applied to different electron or positron. DCA less than

Table 4.3: Primary track selection criteria in p+p collisions

Event Cut Parameters	Cut Value
Spatial Hits	nHitsFit $\geq$ 25
dE/dx Hits	nHitsDedx $\geq$ 15
dca	dca < 3 cm or dca < 1 cm
Pseudorapidity	$\|\eta\|$ < 1.0

one centimeter is employed in "EMC+TPC" electron selecting, which normally has a larger transverse momentum. Tracks that do not match with EMC, we applied a DCA less than 3 cm cut. The track quality requirements for "EMC+TPC" electron and "TPC" electron are lists in Table 4.3.

4.2.3.1 dE/dx

Charged particles, while traversing the TPC gas volume, will interact with the gas atoms and lose energy by ionizing electrons out of the gas atoms. This specific ionization energy loss, called dE/dx, is a function of the particle's momentum magnitude. This property provides a strong particle identification power when select electron candidates. The charge particle's ionization energy loss in material is given by Bethe-Bloch formula. In a thin material, it is described by the more precise Bichsel formula. With measured particle momentum and dE/dx, particle's species can be determined by comparing the ionization energy loss measurements against the Bichsel expectation. Figure 4.4 shows the expected dE/dx distribution for electron, muon, pion, kaon, as well as proton. The dE/dx distribution of charged particle at length L is a Landau distribution at given momentum.

As discussed in the TPC section, a new variable nσ_e is used to have a proper deconvolution of the dE/dx from Landau distribution to a Gaussians distribution by removing 30% of the largest ionization clusters. nσ_e defined as the dE/dx normalized to the expected dE/dx for electrons obtained from the Bichsel functions ($dE/dx_{Bichsel}$) and scaled by the dE/dx resolution ($\sigma_{dE/dx}$). as showed in Eq. 4.1.

$$n\sigma_e = \frac{1}{\sigma_{dE/dx}} log \frac{\langle dE/dx \rangle^{Measured}}{\langle dE/dx \rangle_e^{Bichsel}} \tag{4.1}$$

nσ_e also described the deviation of measured dE/dx value from the predictions value. Figure 4.5 shows the nσ_e vs. particle momentum distribution, which has applied the track quality cuts and associated with a BEMC tower. Two cores are showed. The core appeared around nσ_e $\sim$ -3 is dominated by charged hadrons. The core appeared around 0 is the electron candidates of interested. In this analysis, electron candidates

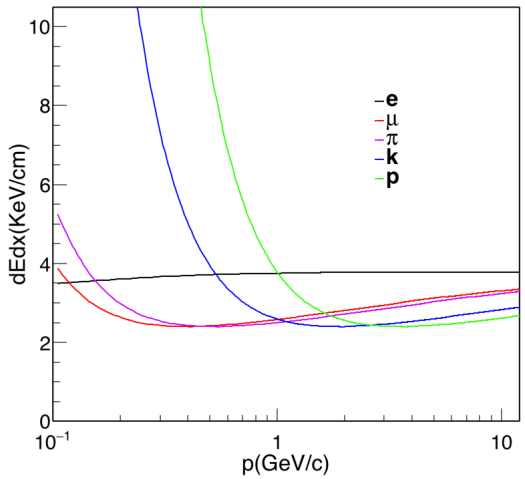

Figure 4.4: Expected dE/dx as a function of momentum for electron, muon, pion, kaon, and proton.

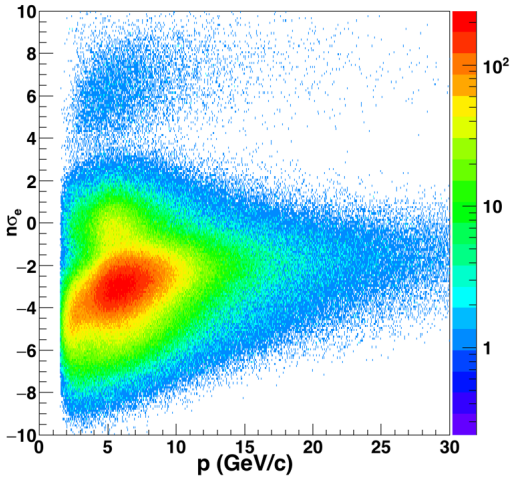

Figure 4.5: nσ_e versus particle momentum after track quality cuts and BEMC association requirement.

are selected by utilizing |nσ_e| < 2 cut. In the high-p_T J/ψ reconstruction, we demand at least one very pure electron daughter at high p_T. Hence, additional information from another detector, such as BEMC, will help to improve the electron purity.

4.2.3.2 BEMC p/E

High energy electron and high energy hadron that passing through a material especially an electromagnetic absorber have very different phenomenon. Bremsstrahlung is the main method to lose energy for a high energy electron in material. The decelerating electron will radiation out high energy photons. The high energy photons will also produce electron and positron through pair production. The parent electron will continue to radiate out photons until it eventually falls below the critical energy. With the electron energy low then the critical energy, ionization energy will dominate the energy loss. At this point, no more shower particles will be produced. Hence, the high electron will induce a shower in the BEMC. The BEMC towers have a radiation length of 21, it is thick enough to stop electron and collect almost all energy that electron deposited in the BEMC. To make sure all electron deposited energy to be collected, in this analysis, the energy deposition in BEMC is defined as energy deposited in a cluster which includes 2 $\times$ 2 towers. Hence, the electron's measured momentum over deposit energy in BEMC ratio p/E is about 1. The picture is more simple for high-energy hadrons that passing through a material. About 30 $\sim$ 40% hadrons produced in collision are so-called "Minimum Ionizing Particles"(MIP). These particles only deposit $\sim$250 - 350 MeV of its energy in the calorimeter due to ionization energy loss. The rest part of particles may interaction with nuclei via strong interaction, which additionally deposes some energy

in BEMC. Thus, the p/E distribution will have a very broad distribution for high energy hadrons. The difference between electron and hadrons can help to suppress the hadron and enhance election sample purity in selection electron candidates.

To compare the electron and hadron p/E distribution, we use a nσ_e < -2 cut to get a hadron rich sample. Electron rich sample is not easy to abstain in a simple method. A composite identification method is used in select electron sample. At middle p_T range, nσ_e and $1/\beta$ information from TOF detector are used. At high p_T range, a tighter $n\sigma_e$ is used. The distributions for electron rich sample and hadron rich sample are showed in Figure 4.6.

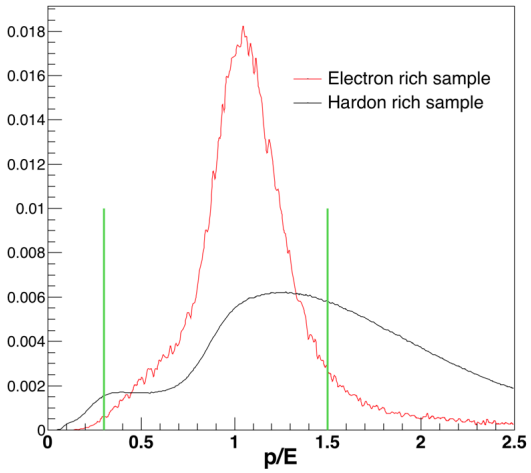

Figure 4.6: The pc/E distribution for hadron rich and electron rich sample from the same data set.

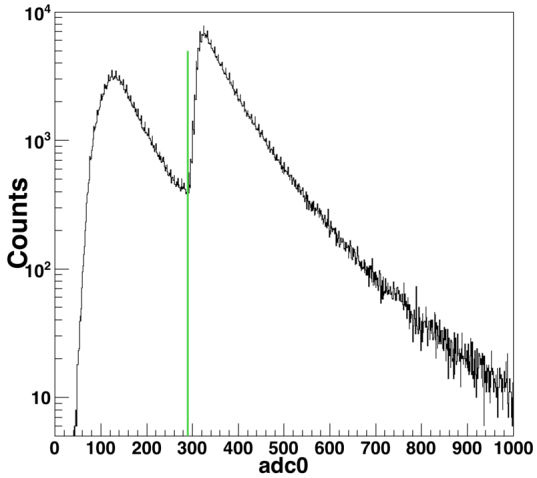

Figure 4.7: The adc0 distribution of all BEMC associated tracks from the BHT1 triggered events.

Hadron sample is scaled to the same number of events as electron rich sample. Electron rich sample is peaked at $\sim$ 1 and shows almost a Gaussian distribution. While, the hadron sample has a long tail on the right-hand side. Hence, we cut on p/E between 0.3 and 1.5 to select electrons.

The BHT1 trigger is used to trigger on the DAQ system which told the system to record the whole events information from every sub-detector. For those BHT1 events, as we are selecting "EMC+TPC" track, one needs to ensure this track (electron) is the one that really triggered the DQA system. A adc0 cut method was proposed by Purdue group [114] to select the trigger electron, which use the adc0 value to mimic the BHT trigger. In the trigger system, the lower 4 bit of Adc0 has been truncated to form a new variable dsmadc which used to compare with the threshold value (18) setting in the trigger setup table. Event will be tagged as BHT1 event with one of the BTOW's dsmadc value larger than 18. Figure 4.7 shows the Adc0 distribution from BHT1 triggered data. A cut is clearly shown at 290, which correspond to the online $dsmadc > 18$ cut. Hence, the trigger particle is selected by requiring the associated BTOW Adc0 larger than 290.

Table 4.4: The summary of the electron identification criteria

Parameter	"EMC+ TPC electron"	"TPC" electron
p_T	p_T > 3.5 GeV/c	p_T > 1.0 GeV/c
Pseudorapidity	$\|\eta\|$ < 1.0	$\|\eta\|$ < 1.0
Spatial Hits	nHitsFit $\geq$ 25	nHitsFit $\geq$ 25
dE/dx Hits	nHitsDedx $\geq$ 15	nHitsDedx $\geq$ 15
dca	dca < 1 cm	dca < 3 cm
nσ_e	(-2, 2)	(-2, 2)
pc/E	(0.3, 1.5)	
adc0	> 290	

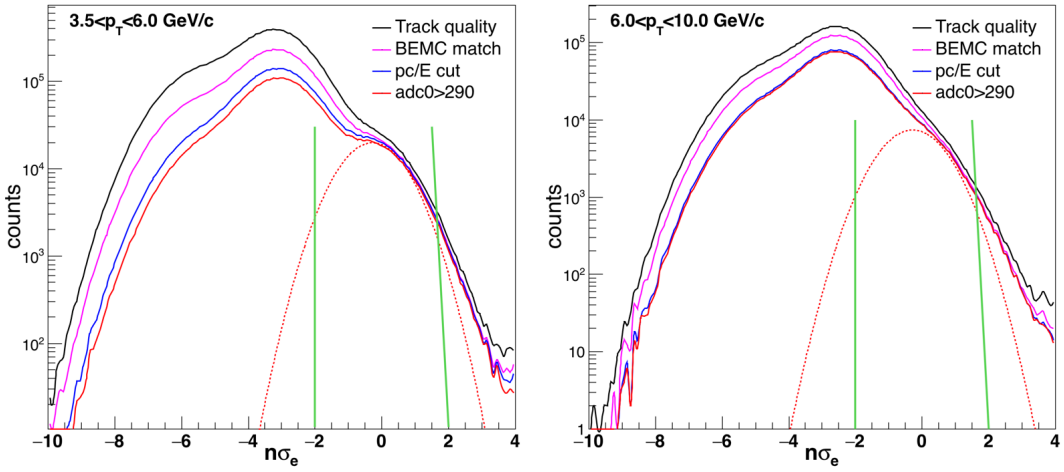

Figure 4.8: The nσ_e distribution after track quality cuts, BEMC association, pc/E and adc0 cuts in two different transverse momentum range.

4.2.4 Electron candiates

After all discussion above, Table 4.4 shows the summary of the electron identification criteria. Figure 4.8 shows different $n\sigma_e$ distributions of charge particle after placing the track quality cuts, BEMC association requirement, pc/E and trigger requirement cuts. As shown in the p_T range of 3.5 to 6 GeV/c, the BEMC association, adc0, and p/E cuts reduced hadron contamination, while electron sample almost keeps the same under these cuts. These cuts help to enhance the purity of trigger electron candidates. In this analysis, electron candidates are selected by requiring -2 < nσ_e < 2.

4.2.5 High-p_T J/ψ reconstruction

Electron and positron that originated from the collision have been used to reconstruct the dielectric invariant mass spectrum. To ensure this event is a real electron triggered event, one electron candidate must fire the BHT trigger, which has been named "EMC + TPC" electron. "EMC+TPC" electron normally has a relatively high trans-

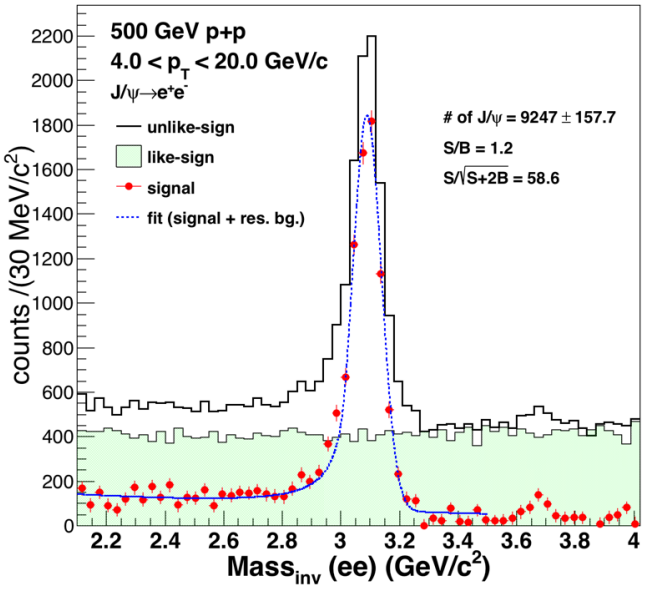

Figure 4.9: The invariant mass distribution of raw signal (red dots), combinatorial background (green filled histogram) and an eye guide fit of the raw J/ψ signal (blue line).

verse momentum compare to another daughter electron. However, the "EMC+TPC" electron sample actually is a very small part in the event. To maximum the J/ψ statistics, we are not only pairing "EMC+TPC" with "EMC+TPC" electrons but also pairing "EMC+TPC" electrons with "TPC" electrons which has a relative low transverse momentum. A track ID index is used to avoid the double counting. The unlike-sign pairs ($e^+ + e^-$) spectrum included physics signals which contain the real J/ψ signal and some correlated background and some non-physics information like the random combinations of opposite-sign pairs. The correlated background involves contributions from D mesons, B mesons decay, and Drell-Yan process. Like-sign pairs (e^++e^+ and e^-+e^-) has been used to estimate the background from random combinations of opposite-sign pairs. Normally, the number of background pairs, $N_{Like-sign}$ is calculated as:

$$N_{Like-sign}(m) = 2 \times \sqrt{N_{e^+e^+}(m) \times N_{e^-e^-}(m)}, \tag{4.2}$$

where N is the number of like-sign pairs. However, as previously discussed, the electron candidate statistics are very low in p+p event, there is a large possibility that $N_{e^+e^+}$ or $N_{e^-e^-}$ is equal to 0. Then, the formula may not reproduce the combinatorial background reasonably and underestimate the conbinatorial background. So we use the sum of $N_{e^+e^+}$ and $N_{e^-e^-}$ instead of 2 times of their geometrical mean as the combinatorial background. Figure 4.9 shows the p_T integrated J/ψ signals with the pair rapidity range of |y| < 1. The unlike-sign is shown in black histogram. The like-sign background is the green filled histogram. The red dot is the raw J/ψ signals which obtained by subtracted the combinatorial background. An eye guidance fit of J/ψ signal and the residual back-

ground are also shown. A J/ψ peak is clearly shown around 3.1 GeV/c^2. The width of the peak is about 50 MeV which mainly coming from electron momentum resolution. On the left-hand side of the J/ψ peak, there is a tail which is results of electron's bremsstrahlung energy loss in detector and the J/ψ internal radiation effect. J/ψ internal radiation is J/ψ decay into a lepton pair and a photon. The missing photon contribution will introduce a relative low reconstructed J/ψ mass. The J/ψ raw yield is extracted by using bin counting method which count the unlike-sign and like-sign pairs in a relatively large mass range from 2.7 to 3.3 GeV/c^2. The amount of background is quantified using the signal-to-background ratio, S/B, where S = $N_{J/\psi}$ = $N_{Unlike-sign}$ - $N_{Like-Sign}$ and the background is $N_{Like-Sign}$. The signal strength is defined by its significance $S/\sqrt{S+B}$. We have about 9000 raw J/ψ signals with a signal-to-background ratio of 1.2 and signal strength of 58.6 in this dataset.

4.2.6 Acceptance and Efficiency

4.2.6.1 Embedding technique and QA

J/ψ efficiency and acceptance are obtained by embedding Monte Carlo technique which embedded the Monte Carlo J/ψs into the real data events. The real data events used in the embedding are sampled over the entire data-taking period in order to have proper representation of the whole dataset used in analysis. The embedding has following procedure: First, 5 J/ψs are embedded in the event and every J/ψ decays in di-electron channel. A GEANT simulation which turned on all processes including hadronic interaction, decay and multiple scattering is used to determine the interaction of the daughter electron with the detector material and electrons are propagated through the full STAR detector and geometry. The TPC simulation is done by a realistic simulation of the STAR-TPC response. The EMC response is usually done by running an EMC afterburner maker. The simulated electron tracks are blended into real events at raw data level. Second, the mixed event is treated as real data and processed through the full reconstruction chain. Third, an association map is created between the Monte Carlo tracks and the reconstructed tracks. The association is made by matching hit between Monte Carlo hits and hits used in track reconstruction in a 3 cm window in both x and y direction. With the association map, one can get the efficiency and acceptance from embedding. In this analysis, the Monte Carlo J/ψ has follow setup:

- 40k p+p 500GeV BHT1 trigger events
- Particles per event: 5
- Valid vertex

- $0 < \phi < 2\pi$, flat distribution
- -1 < η < 1, flat distribution
- $0 < p_T < 30$ GeV/c, flat distribution

Each event embedded in 5 J/ψs, equivalent to 10 tracks, may affect the TPC reconstruction efficiency as the charged-particle multiplicity is low in p+p collision. This effect has been studied by Bingchu Huang, who embedded 15 Pions into a p+p event at $\sqrt{s}$ = 200 GeV. His study shows that the efficiency difference is less than 0.3%. Another potential issue is that additional 10 tracks in a p+p event may enhance the signal electron trigger efficiency, especially at low p_T. The probability of two or more electrons hit on the same BEMC tower is increased. This double hit tower obviously has a higher deposited energy than a single electron, which will enhance the trigger efficiency. Zebo Tang has investigated this enhancement in his Ph.D. thesis [115], and pointed out that by applying an isolation cut of $|\Delta y_{MC}| \leq 0.1$ or $|\Delta\phi_{MC}| \leq 0.5$ between electrons can successfully get rid of this enhancement. The same isolation cut is also applied in this analysis.

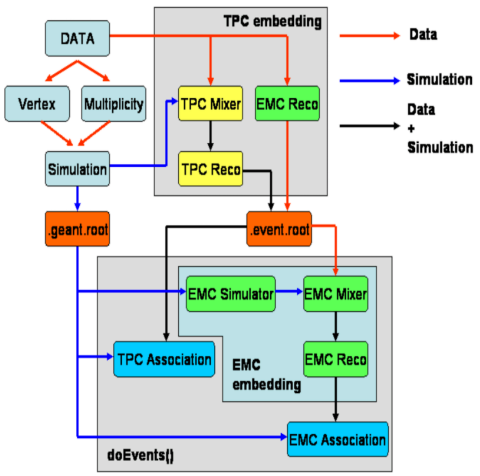

Figure 4.10: The Barrel EMC embedding workflow of J/ψ. The blue line shows the simulation data transfer. The organ line are the real data flow. The black line is the simulation and data mixed data flow.

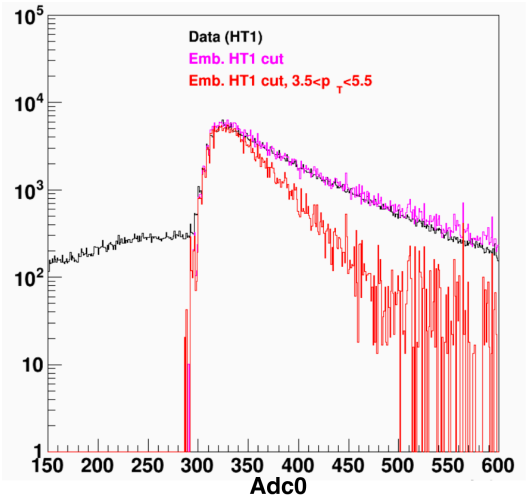

Figure 4.11: The adc0 distribution of BEMC associated tracks. The black curve is the distribution from read data measurement. The magenta and red curve are from BHT1 embedding data and a specified p_T range.

Trigger efficiency is an essential part of the embedding. The difference between data and embedding will directly affect the final cross section measurement. As discussed previously, BHT1 trigger events are those events which have one BTOW's Adc0 large than 290. Hence, this trigger requirement is an event level criterion. However, given the condition that in p+p event the produced track number are very small, the

online $dsmadc$ cut could also be understood as a track level cut especial with a high p_T matching requirement. Hence, we can compare the Adc0 distributions between data and embedding as a consistent check. Figure 4.11 shows the comparison, the edges are consistent with each other, which means: 1) the trigger implementation is quite good; 2) the energy scale of BEMC is very well.

4.2.6.2 Electron detection efficiency

In this section, we will talk about the electron detection efficiency. Two kinds of electron/positron are selected in the analysis. "EMC+TPC" electron detection efficiency includes the trigger efficiency, tracking efficiency, as well as the nσ_e cuts efficiency. The "TPC only" electron detection efficiency includes all the efficiency as "EMC+TPC" except the trigger efficiency. In the previous section, we talked the embedding technique on how to built the map between embedding track and reconstructed track. The embedding technique can estimate the trigger efficiency and tracking efficiency, while the nσ_e cuts efficiency and the nHitsDedx cuts efficiency need to be extracted directly from data.

4.2.6.3 "EMC + TPC" electron and "TPC" electron efficiency

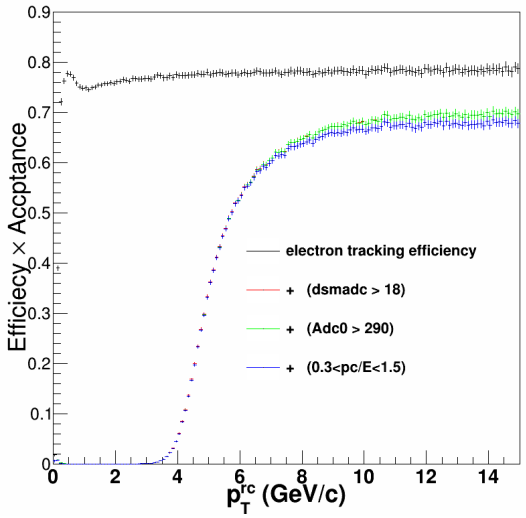

Figure 4.12: Single electron efficiency after applied the track quality cuts, online trigger requirement, offline trigger electron selection criteria, as well as the pc/E cuts.

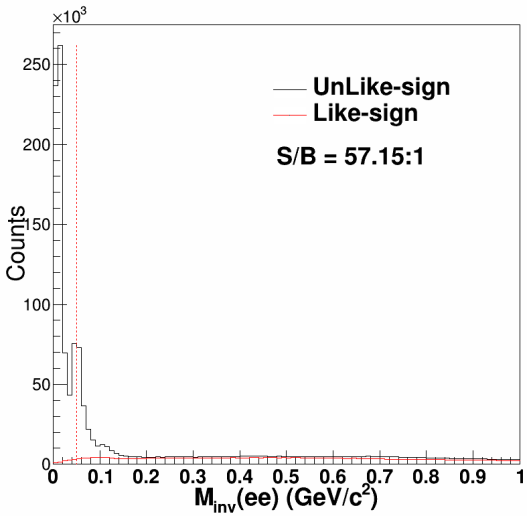

Figure 4.13: The unlike-sign and like-sign invariant mass distribution in black and red, respectively. The red dash line indicated the mass criteria for pure electron sample selecting.

The selection criteria for "EMC+TPC" electron and "TPC" electron have been listed in Table 4.4. The "TPC only" electron tracking efficiency is shown in Figure 4.12 which obtained from embedding by using the same track quality cuts as used in the real data analysis. The tracking efficiency quickly saturated at 78% as p_T increase.

The electron trigger efficiency is also shown, the efficiency curve turns on at about 3.5 GeV/c, and quickly get saturated at high-p_T. The pc/E cuts, as it showed, has a high selection efficiency for electrons.

4.2.6.4 nσ_e cuts and nHitsDedx cut efficiency

Currently, the embedding simulation can not fully simulate particle's dE/dx in TPC. Hence, we need to get the nσ_e cuts and nHitsDedx cut efficiency from real data. If the TPC has an ideal calibration, then nσ_e distribution's mean and σ should equal to 0 and 1 for electron. However, the real case is that the mean of nσ_e is not exactly equal to 0 and the sigma is also not exactly equal to 1. A pure electron sample is used to get the electron's nσ_e distribution. In the BHT1 events, we can reconstruct many "0" mass particle by pairing the electron and positron candidates. This "0" mass particles have two source, one part is π^0 Dalitz decay contribution, another part is the photon pair production. In the mass range of 0 to 0.05 GeV/c^2, the signal to background ratio is larger than 57, and the background is estimated by the like-sign method. As shown in Figure 4.13. This high S/B ratio tells that the electron/positron candidates purity is very high in this mass range. One can use this part electron/positron to extract the nσ_e distribution's mean and σ. The mean and σ distribution as a function of transverse momentum are show in Figure 4.14. Both mean and σ shows no p_T dependence. The mean value is slightly lower than 0 and the σ is about 0.9. In this analysis, we applied a very large nσ_e cuts. Hence, the slight deviation from 0 of nσ_e's mean will not have a large effect on the cuts efficiency. The efficiency of $|n\sigma_e| < 2$ cuts efficiency is larger than 95%. The nHitsDedx > 15 cut efficiency is also acquired from photonic electron.

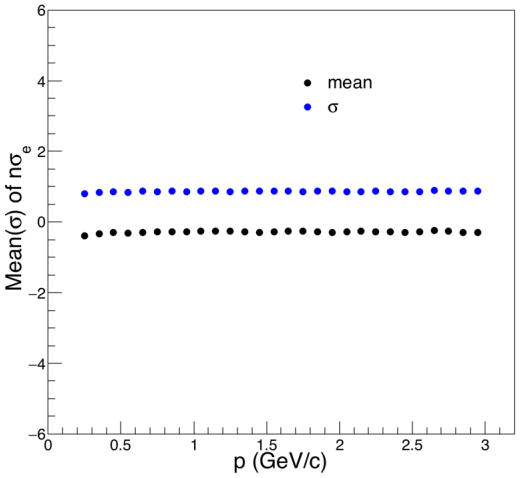

Figure 4.14: The mean and σ of nσ_e distribution as a function of the electron transverse momentum. The electron is selected from photonic electron.

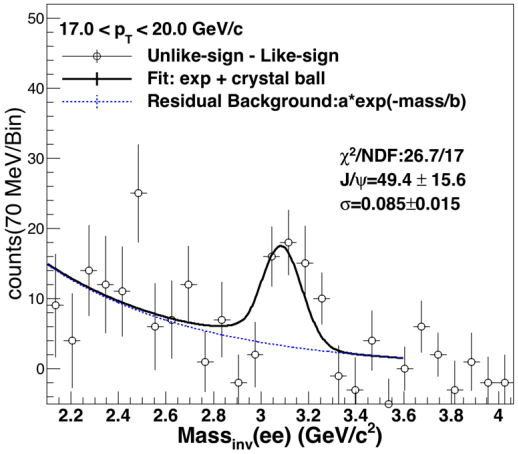

Figure 4.15: The J/ψ signal at the highest p_T bin. The open circle is the raw signal after combinatorial background subtraction. The dash blue line indicates the residual background.

We compared the number of tracks with and without this cut after the basic tracking quality cuts to estimate the nHitsDedx efficiency. The average efficiency of nHitsDedx > 15 cut is about 97%.

4.2.7 Yield extraction and J/ψ detector efficiency

4.2.7.1 Yield extraction

As shown in Figure 4.9, with the combinatorial background subtracted, residual background from $c\bar{c}$, $b\bar{b}$ and Drell-Yan needs to be further subtracted. In this analysis, we used an exponential function to describe the residual background and the raw J/ψ is extracted by using counting di-electron counts in the mass range of 2.7 to 3.3 GeV/c^2. Hence, part of the J/ψ will not be counted due to energy loss. To evaluate the mass window cut efficiency. A simulation of electron energy loss in the detector is needed. This simulation is done in the embedding procedure which has simulated all detector response as well as energy loss of the electron. Hence, the J/ψ signal line shape is determined from embedding Monte Carlo J/ψs. We fitted MC J/ψ signals by Crystal-Ball function which consists of a Gaussian core portion and a power-low tail. Such a power-low tail is account for the energy loss in material. The function is given by:

$$f(x;\alpha;n;\overline{x};\sigma) = \begin{cases} N \cdot exp(-\frac{(x-\overline{x})^2}{2\sigma^2}), & \frac{x-\overline{x}}{\sigma} > -\alpha \\ A \cdot (B - \frac{x-\overline{x}}{\sigma})^{-n}, & \frac{x-\overline{x}}{\sigma} \leq -\alpha \end{cases} \tag{4.3}$$

(4.4)

where:

$$A = \frac{n}{|\alpha|}^{n} \cdot exp(-\frac{|\alpha|^2}{2})$$

$$B = \frac{n}{|\alpha|} - |\alpha|$$

$$C = \frac{n}{|\alpha|} \cdot \frac{1}{n-1} \cdot exp(-\frac{|\alpha|^2}{2})$$

$$D = \sqrt{\frac{\pi}{2}}(1 + erf(\frac{|\alpha|}{\sqrt{2}}))$$

$$N = \frac{1}{\sigma(C+D)}$$

The invariant mass distribution of the J/ψ signal obtained from the embedding (the J/ψ line shape) involved the electron energy loss inside the detectors as well as the transverse momentum resolution. The electron's momentum normally needs an additional smearing. This can be found by comparing the reconstructed J/ψ width between simulation and data in the same p_T range. This can be understand in terms of different

treatment of the vertex in embedding and data. In the embedding sample, J/ψs are assigned to the vertex, and the J/ψ are forced to decay at this vertex. Furthermore, no embedded tracks were used in the vertex reconstruction. While the primary track's momentum is a refit of the track after adding vertex in track. Hence, the vertex's resolution was not contribute in the tracks's momentum resolution in the embedding, which introduce a better momentum resolution in embedding than data. There are two methods to deal with the underestimation of momentum resolution. One can add an additional Gaussian smearing on particle's momentum, while the Gaussian's σ is a function of p_T. By comparing the J/ψ from embedding and J/ψ from real data, one can find the best smearing parameter. In this analysis, we used another method. We extracted the J/ψ shape from embedding and fixed the parameters of n, α and mean value, but leave σ as a free parameter when fitting the data. This free σ will take into account the additional momentum smearing in the fitting process.

The residual background is obtained by integrating the exponential function in the mass range of 2.7 to 3.3 GeV/c^2 and divided the bin width. The mass counting efficiency is corrected by the Crystal ball function which extracted from data fitting. The Crystal ball function was integrated both in the mass range of 0 to 3.3 GeV/c^2 and mass counting range. The J/ψ mass counting efficiency is obtained by comparing this two integrated values. The mass counting efficiency is about 0.9 and no p_T dependence is observed in currently statistics. Thus, we applied an overall mass cuts efficiency in all p_T bins.

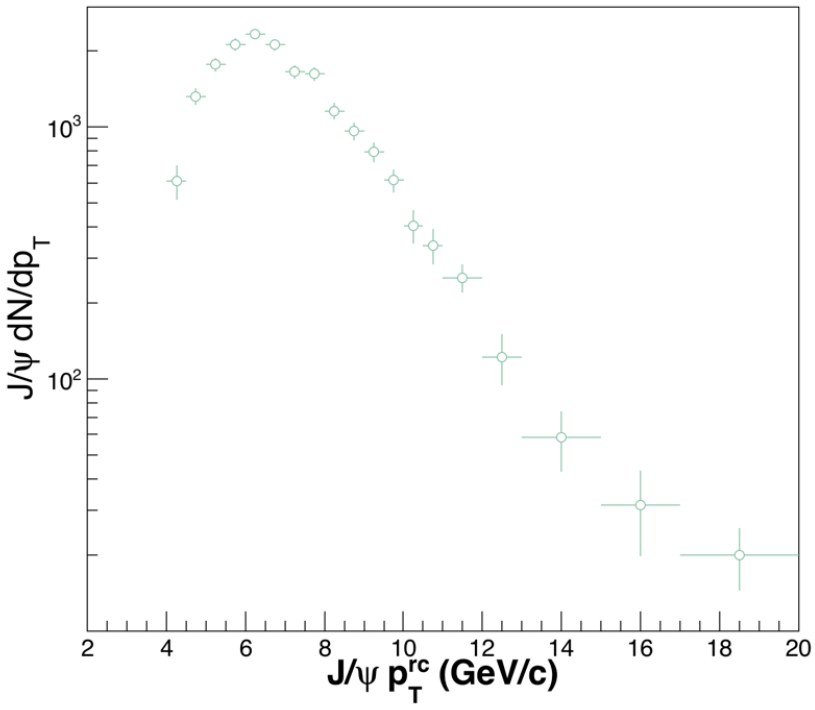

Figure 4.16: Inclusive J/ψ dN/dp_T distribution as a function of J/ψ p_T.

A total of 9000 J/ψs have been reconstructed by using BHT1 events in p+p collisions at $\sqrt{s}$ = 500 GeV. In each p_T bins, we couns the signals in the mass window of (2.7, 3.3) GeV/c^2, and subtracte all background (combinatorial and residual background), also correct the mass counting efficiency. Figure 4.15 shows the yield extraction at the highest J/ψ p_T bin with p_T range of 17 < p_T < 20 GeV/c. The open circle is the raw signal after combinatorial background subtraction. The black line is the data fitting result by using Crystal ball function and an exponential function. The blue dash line indicates the residual background. In this J/ψ p_T range, we get about 49 J/ψ counts. The yield of J/ψ as a function of reconstructed J/ψ transverse momentum is shown in Figure 4.16. The J/ψ is divided into 19 p_T bins with a kinematic range of 4 < p_T < 20 GeV/c in the rapidity range of |y| <1. We had enough statics have a very fine bin width of 0.5 GeV/c in the p_T range of 4 to 12 GeV/c.

4.2.7.2 Efficiency and acceptance correction

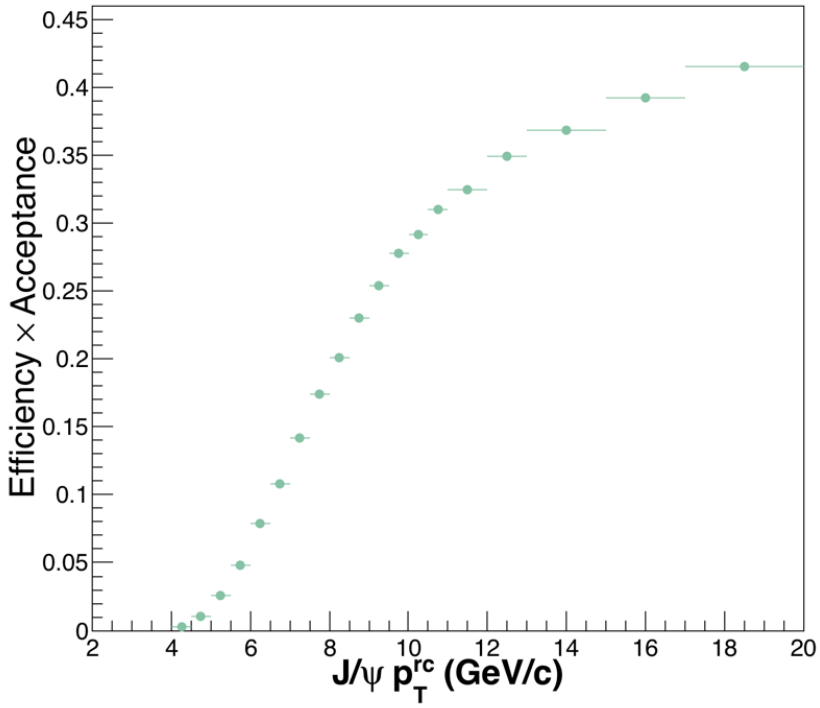

Figure 4.17: J/ψ total detector efficiency as a function of J/ψ transverse moemtnum.

The embedding J/ψ p_T spectrum has a flat distribution, while the real J/ψ spectrum is apparently not a flat distribution. The momentum smearing effect will change the reconstructed J/ψ spectrum to a different distribution which shows an input J/ψ p_T shape dependence. However, it is the first time to measure the J/ψ cross section in the proton-proton collisions at $\sqrt{s}$ = 500 GeV, the J/ψ transverse momentum spectrum is not known.

To deal with this effect, an iteration method is used to get the final detection efficiency. First, a flat J/ψ p_T distribution is used as an input distribution, and one can obtain the J/ψ detection efficiency under this MC p_T shape. Second, the raw J/ψ spectrum is corrected by the efficiency getting from the first step. Third, the corrected J/ψ spectrum line shape is used as a new J/ψ input p_T spectrum. Then repeating the procedure until the final efficiency becomes a stable shape. The final J/ψ detection efficiency in the BHT1 trigger is shown in Figure 4.17. The curve turns on at about 4 GeV/c. And the detector efficiency has a very rapidly increase at high p_T range. At the high-p_T range, the efficiency is more than 30%.

4.2.8 Systematic Uncertainty on J/ψ p_T spectrum measurement

The following sources has been taken into account in the systematic uncertainty evaluation: imperfect trigger simulation, imperfect tracking simulation, J/ψ yield extraction, as well as the nσ_e distribution.

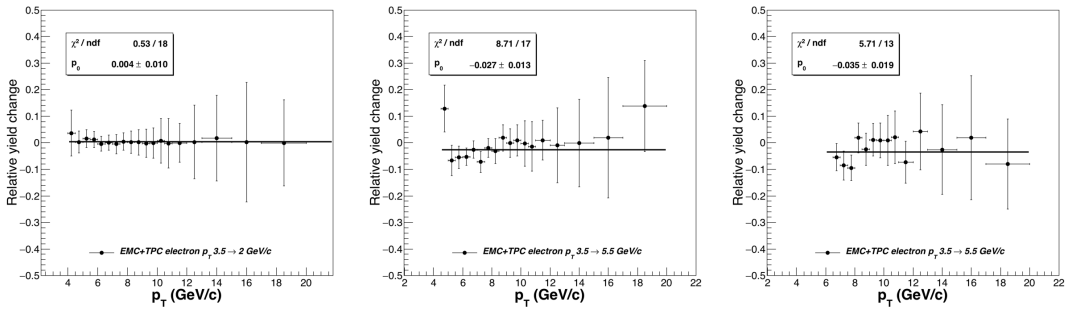

Figure 4.18: J/ψ bin-by-bin systematic uncertainties by varying p_T cut on "EMC+TPC" electron candidates.

The imperfect trigger simulation may caused by two reasons: imperfect momentum simulation and imperfect BEMC tower simulation. To estimate the imperfect momentum simulation, we changed the p_T cut of "EMC+TPC" electron candidates to 2 GeV/c, 4.5 GeV/c and 5.5 GeV/c, separately. By changing only on p_T cut in "EMC+TPC" electron candidates, the J/ψ raw yield and detection efficiency are recalculated and the difference between this two invariant yields is assigned as the systematic uncertainty. The bin by bin systematic uncertainty by varying p_T cuts on "EMC+TPC" electron candidates are shown in Figure 4.18. To average out the statistic fluctuation, a constant linear function is used to fit the bin-by-bin systematic uncertainties, the overall systematic uncertainties are 0.4%, 2.7% and 3.5% by using different p_T cuts. The maximum deviation is taken as the systematic uncertainty caused by p_T cuts.

We used the same method to evaluate the systematic uncertainty that originated from imperfect BEMC tower simulation by changing the adc0 value from 290 to 300.

Another simulation related to BEMC is the pc/E cuts. pc/E cuts are important cuts to suppress the hadron in selecting "EMC+TPC" electron candidates. Different pc/E cuts for "EMC+TPC" electron candidates are used to estimate the systematic uncertainty from possible imperfect BEMC cluster response simulation in embedding. The adc0 cut contribute 0.5% in systematic uncertainty. The pc/E cuts contribute about 2.3% in total systematic uncertainty, as shown in Figure 4.19. The tracking efficiencies system-

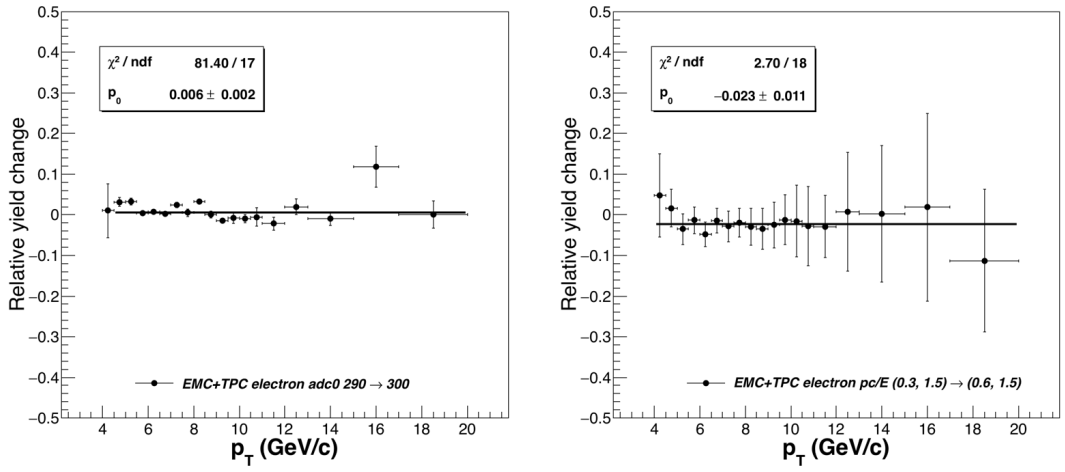

Figure 4.19: J/ψ bin-by-bin systematic uncertainties by varying adc0 cut and pcE cut on "EMC+TPC" electron candidates.

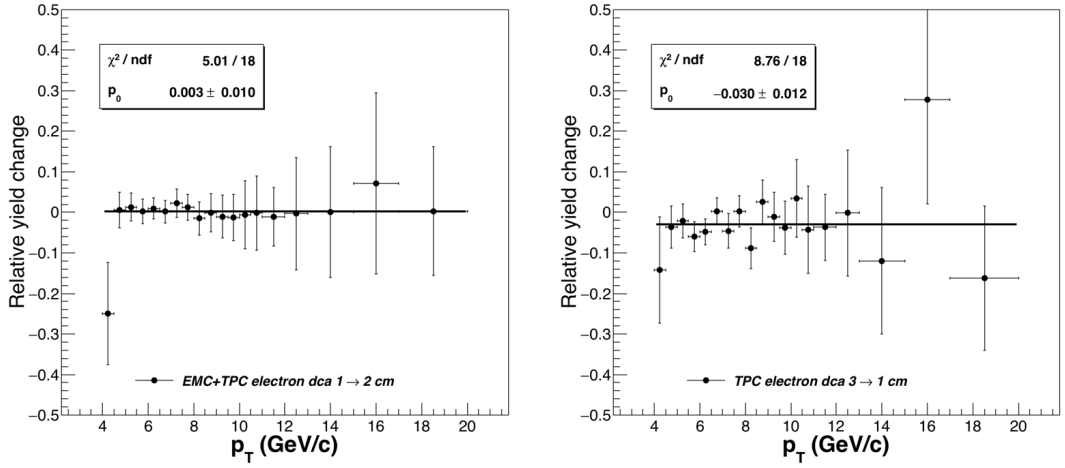

Figure 4.20: J/ψ bin-by-bin systematic uncertainties by varying "EMC+TPC" electron DCA cut and "TPC" electron DCA cut.

atic uncertainty is studied by changing the "EMC + TPC" electron's DCA and "TPC" electron's DCA, respectively. The "EMC + TPC" electron candidate's DCA is changed from 1 cm to 2 cm and the "TPC" electron candidate's DCA is changed from 3 cm to 1 cm, as shown in Figure 4.20. The uncertainties associated with the electron dE/dx

Table 4.5: The summary of the systematic uncertainty in $J\psi$ p_T spectra

Source	systematic uncertainty
p_T	3.5%
$adc0$	0.5%
p/E	2.3%
DCA	3.0%
$n\sigma_e$	3.6%
yield extraction	1.3%
totoal	6.4%

identification efficiency is evaluate by change "EMC +TPC" and "TPC" electron's nσ_e cuts from (-2, 2) to (-2.5, 2.5), respectively, as shown in Figure 4.21.

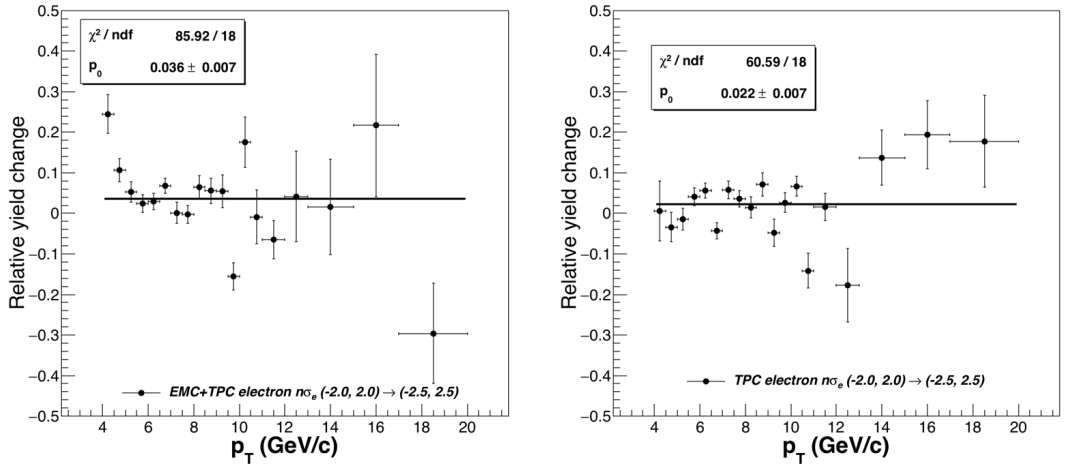

Figure 4.21: J/ψ bin-by-bin systematic uncertainties by varying "EMC+TPC" electron and "TPC" electron's nσ_e cuts.

Different mass counting range and fitting range are used to estimate the systematic uncertainties from yield extraction. We tried to enlarge and narrow down the signal counting mass range to evaluate the systematic uncertainties from mass counting range. The fitting range will affect residual background, we also enlarge and narrow down the fitting range to estimate systematic uncertainty from fitting process. The mass counting range and fitting range together contributes about 1.3% to the total systematic uncertainty.

The systematic uncertainties on J/ψ differential invariant cross-section are summarized in Table 4.5 for BHT1 triggered data.

The J/ψ polarization parameter λ_θ is measured to be negative at high p_T region in proton-proton collisions at $\sqrt{s}$ = 200 GeV at STAR experiment [116]. The detector acceptance is different for different J/ψ polarization parameter. Hence, the J/ψ polar-

ization is also a source of systematic uncertainty which affect the cross section measurement. Currently, there is no published J/ψ polarization measurement in p+p collisions at $\sqrt{s}$ = 500 GeV. STAR has a preliminary result on J/ψ polarization at $\sqrt{s}$ = 500 GeV with a p_T range of 5 < p_T < 16 GeV/c. We use this J/ψ polarization parameters to estimate the effect caused by polarization.

We assume that the polarization has a constant polarization parameter in the kinematic range of 0< p_T < 5 GeV/c, which may over estimate the polarization parameter. We also assumed the polarization is the same with p_T large than 16 GeV/c. The J/ψ decay electron angular distribution will follow the distribution below:

$$dN/d\cos\theta \propto 1 + \lambda_\theta \cos^2(\theta) \tag{4.5}$$

The left panel of Figure 4.22 shows the J/ψ detection efficiency with and without polar-

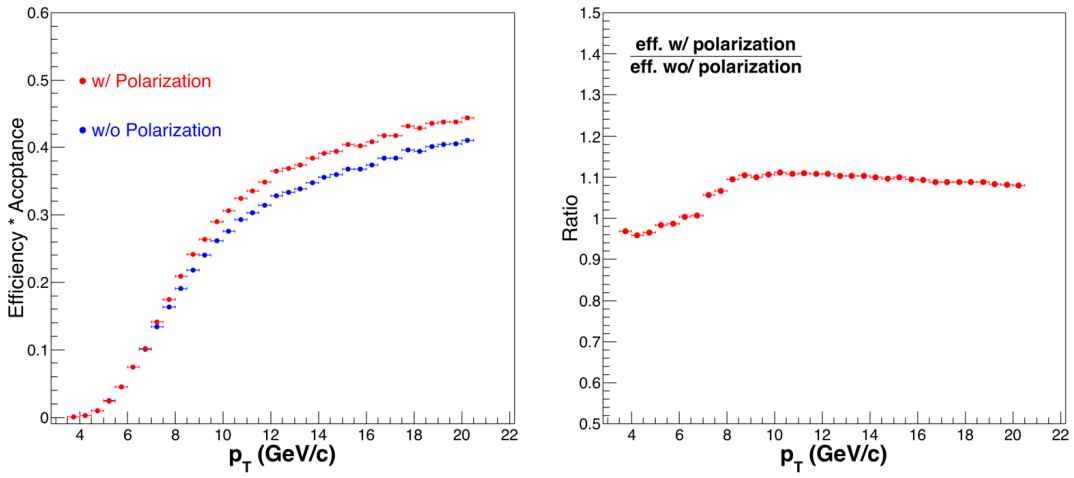

Figure 4.22: Left: J/ψ detection efficiency with (blue) and without (red) J/ψ polarization verse J/ψ p_T. Right: The ratio of J/ψ detection efficiency with and without J/ψ polarization.

ization. The right panel shows the ratio of polarized J/ψ and unpolarized J/ψ efficiency difference, there is about 10% difference. The systematic uncertainty caused by J/ψ polarization is taken as a special systematic uncertainty as the efficiency enhancement can be primely addressed with more study on J/ψ polarization.

4.3 $\psi(2S)$ analysis

The data set used for the $\psi(2S)$ analysis is the same as used in the J/ψ analysis. Also, the online trigger is BHT1 trigger as used in the J/ψ analysis. The di-electron decay branch ratio for $\psi(2S)$ is $(7.72 \pm 0.17)\times10^{-3}$, which is about an order of magnitude lower than J/ψ. But due to the high enhancement of the electron rich sample in the BHT1 trigger events, we can still reconstruct the $\psi(2S)$ in the di-electron decay channel.

4.3.1 $\psi(2S)$ analysis detials

Since we are reconstructing the $\psi(2S)$ also in the di-electron channel by using the same data set and trigger just like in the J/ψ reconstruction. The vertex requirement of BHT1 events are a valid vertex and the reconstructed V_z should be inside the TPC. The primary requirement of J/ψ reconstruction is a very purity electron sample, which requires the electron fired the BHT1 trigger. Hence, in the $\psi(2S)$ analysis, we used the same method as in the J/ψ analysis. First, we selected the "EMC+TPC" electrons, then selected the "TPC" electrons. The selecting criteria are also the same as in the J/ψ analysis, which have been listed in Table 4.4.

We pair the electron candidates and positron candidates from the same events to reconstruct the $\psi(2S)$ signal. The combinatorial background is estimated by the like-sign method as discussed in the J/ψ reconstruction. As for the residual background, we used a linear function to describe it. The yield extraction of $\psi(2S)$ method is by using bin counting, which counts the number of the count in the mass range of $3.5 < m_{inv} < 3.8$ GeV/c^2. The energy loss of the $\psi(2S)$ decayed electron is still there. Hence, a crystal ball function is also employed to describe the reconstructed $\psi(2S)$ signal. The line shape of the $\psi(2S)$ is obtained from embedding technique as we have discussed in J/ψ analysis. Figure 4.23 shows the $\psi(2S)$ signals, the open circle is the raw signal, which is the unlike-sign signals minus the like-sign signals. The blue line shows the residual background. In this data sample, the $\psi(2S)$ signals are 305 $\pm$ 106 in the kinematics range of $4 < p_T < 12$ GeV/c. The signal strength is 3.9.

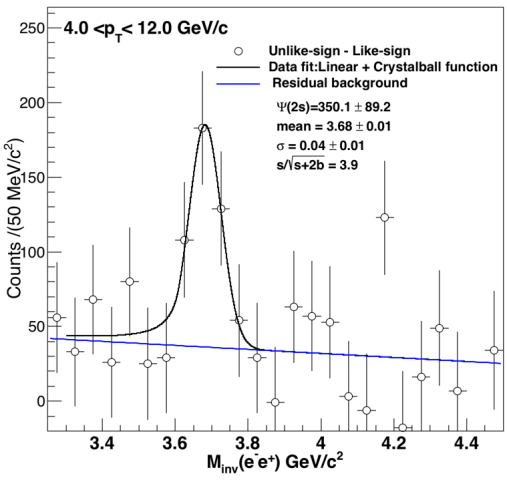

Figure 4.23: The $\psi(2S)$ signal after the combinatorial background subtraction (open black circles). Linear + Crystal ball function fitting are shown in black. Blue curve indicates the residual background.

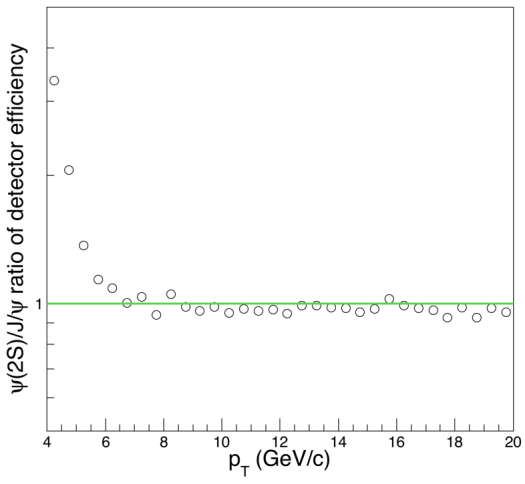

Figure 4.24: The detector efficiency difference between $\psi(2S)$ and J/ψ in the same BHT1 trigger events, $\psi(2S)$ are J/ψ are reconstructed by same selecting criterions on events, electron candidates.

In the $\psi(2s)$ analysis, we also required $\psi(2S)$ embedding sample, which embedded

5 $\psi(2S)$s in the real BHT1 data, with flat distributions in y, ϕ, as well as transverse momentum range of 0 < p_T < 20 GeV/c. The $\psi(2S)$ transverse momentum shape is not measured in p+p collisions at $\sqrt{s}$ = 500 GeV yet. As we have mentioned in the J/ψ measurement, we need a reasonable MC $\psi(2S)$ p_T shape, otherwise, the efficiency obtained from the embedding may not right. In this analysis, we assume that the $\psi(2S)$ has the same transverse momentum shape as J/ψ. With this assumption, we obtained the $\psi(2S)$ detector efficiency.

The total detector efficiency for $\psi(2S)$ may have some difference from J/ψ due to the different invariant mass. Figure 4.24 shows the $\psi(2S)$ efficiency to J/ψ efficiency ratio as a function of transverse momentum. The green line is a const function with y value equal to 1. A big difference can be found at the p_T about 4 GeV/c. In this p_T range, the energy of the decay electron, from both J/ψ and $\psi(2S)$, is near the trigger threshold ($\sim$ 4.3 GeV), and thus both have a low detector efficiency ($\sim$ 1%). Then one or two percent efficiency enhance will have a huge relative difference. The relative large invariant mass of $\psi(2S)$ can boost the decay electron to a higher energy. Thus, at about 4 GeV/c, the efficiency will have a huge difference. While at the high p_T range, the open angle between electron and positron from $\psi(2S)$ decay will slightly larger than J/ψ's in additional the trigger efficiency has been saturated at high-p_T. Hence, the main difference of detector efficiency for $\psi(2S)$ and J/ψ is the acceptance. A larger open angle means a smaller acceptance. Hence, at high p_T range the $\psi(2S)$ detector efficiency is slightly lower than the J/ψ.

4.3.2 Systematic Uncertainty on $\psi(2S)$ to J/ψ yield ratio measurement

The systematic uncertainty of $\psi(2S)$ to J/ψ yield ratio measurement are largely cancelled out due to the same set of cuts used in the analysis. In this analysis, the following uncertainties source are take into account: the p_T cuts of the triggered electron, the adc0 cut, the pc/E cuts, as well as the DCA value. The systematic uncertainty is extracted the same method as in J/ψ systematic uncertainty study. The systematic uncertainties of $\psi(2S)$ to J/ψ yield ratio are summarized in Table 4.6. The total systematic uncertainty is less than 11%.

4.4 J/ψ production versus charged-particle multiplicity analysis

4.4.1 Vertex finding algorithm in p+p events at STAR

It is important to reconstruct a vertex in a given event which corresponds to the collision that fired the trigger. The right vertex is essential to the physics results and calculates the corresponding sampled luminosity of certain trigger. The challenge is

Table 4.6: The summary of the systematic uncertainty in $\psi(2S)$ p_T spectra

Source	systematic uncertainty
p_T	6.0%
$adc0$	3.0%
p/E	6.0%
DCA	3.0%
totoal	$< 11\%$

that a high luminosity environment coupled with a detector read-out time much longer than the time between bunch crossings, will cause many pile-up vertices to be recorded in each event. Hence, every recorded event included lots of pile-up tracks from previous and post bunch crossing collisions. All these tracks will contribute to the vertex reconstruction. Thus, the vertex from previous and post bunch crossings will also be reconstructed, which is actually not interested. In addition, the proton-proton NSD collision has a very low charged-particle multiplicity, which is less than 10 tracks in the rapidity range of $|y|<1$. In proton-proton collisions, Pile-Up Proof Vertex (PPV) finder has been optimized for vertex finding in low multiplicity p+p events. PPV takes a collection of tracks from an event and uses these tracks to reconstruct vertices. Then, a ranking value is assigned to each reconstructed vertex according to the possibility of which is coming from corresponding bunch crossing. STAR TPC read-out time is about 40 μs, while in Run11 the BBCMB trigger rate is about 2M Hz. Then, every recorded event will contain about 140 min-bias collisions information. In order to determinate the right vertex location, three detectors are used in vertex finder: TPC, BEMC, as well as Endcap Electromagnetic Calorimeter (EEMC). EMCs are fast detectors, they can read out and reset in 10 ns, which allows them read out detector information every bunch crossing. There are three types of pile-up events: vertices that come from collisions

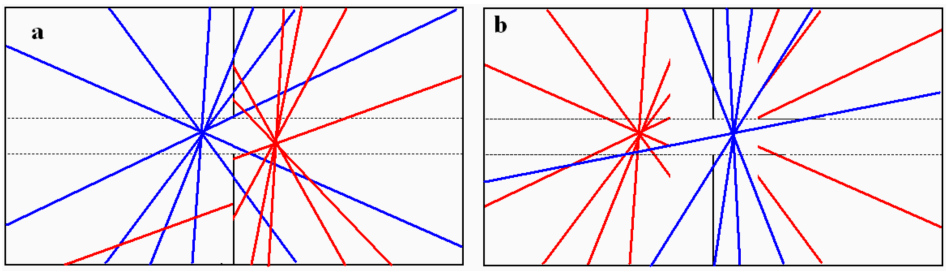

Figure 4.25: Pile-up events illustration, the blue line are tracks from the events fired the trigger, red lines are tracks from previous collision (a) and post collision (b).

within the same bunch crossing, vertices that come from collisions from previous or post bunch crossings. The ranking system is designed to remove vertices corresponding to the pre-crossing and post-crossing collisions. The idea of pile-up rejection is the

time difference between event that fired the trigger and the events from pro-crossing or post-crossing collisions which we call it out-of-time events. Tracks from these out-of-time events are reconstructed as being shifted along z and broken into two tracks where they cross the TPC central membrane as shown in Figure 4.25. The collisions that coming from the same bunch crossing are referred to within the bucket. The PPV can not separate in-bunch pile-up, as these collisions are fallen into the same time scale just like the events fired the trigger.

PPV is used to locate the z position of a vertex. The x and y position are determined by bean-line constraint in each run. The beam-line constraint is calculated by fitting high multiplicity events with MinuitVF without any constraints on the vertex position. MinuitVF is the vertex finder used in the heavy-ion collisions, which normally have a high multiplicity. Then, a straight line is fit to the vertex distributions to obtain a relationship between x, y, and z. For tracks used in the vertex reconstruction, it has followed requirement. The track can be extrapolated to within 3 cm to beam line and the closest point should be inside the TPC ($|V_z| < 200$ cm). The track's minimum momentum should be larger than 0.2 GeV/c. The fraction of TPC hit points over the number of possible TPC hit points should be larger than 0.7. Figure 4.26 shows the track selection criteria in the vertex reconstruction and the picture of extrapolation of tracks to the beam-line. The extrapolation has taken all material effect into account. Then the qualified tracks are assigned with an initial weight according to their DCA

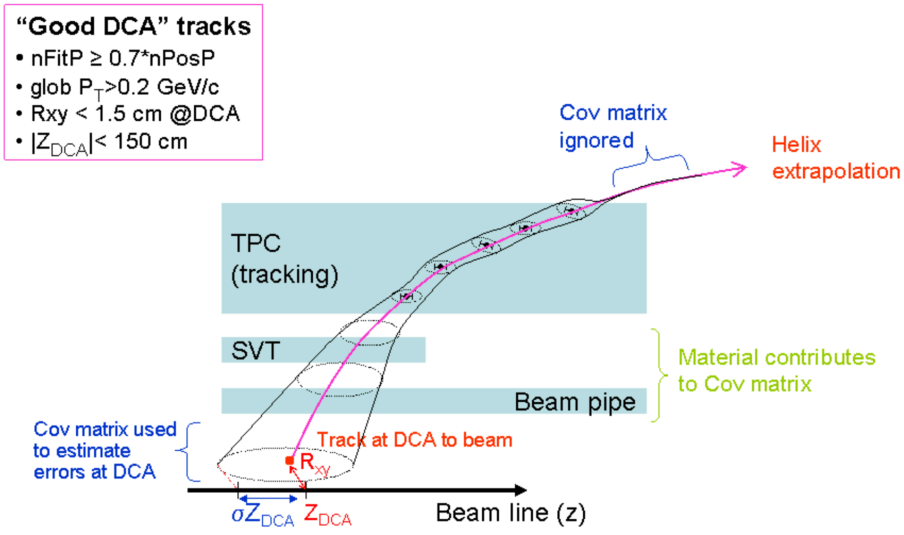

Figure 4.26: The track selection criteria in the vertex reconstruction and picture of extrapolation of tracks to the beamline, which taken all material effect into account.

to the beam-line and the error of their extrapolation. If the tracks can be projected to either BEMC or EEMC tower, and the EMC tower has an energy deposition, then the weight will increase to 4. If the track crossed the TPC central membrane, the track's

Table 4.7: Track weight corrections table for different detectors in PPV finder

Detector	Match Factor	Veto Factor	"Dunno" Factor
BEMC	4	3/4	1
EEMC	4	3/4	1
TPC	5	1/5	1

weight is increased to 5. On the contrary, tracks which extrapolate to a point in either BEMC or EEMC tower without a deposited energy are considered vetoed and given a reduced weight of 3/4 for EMCs. If the track doesn't extrapolate to the BEMC or the EEMC, or the part of the detector it extrapolates to is unable to be read out, the track gets a "dunno" factor for its weight. The total weight for the track is the product of all of the weights. The weight changes of different conditions are shown in Table 4.7. The truncated likelihood of the track belonging to a primary vertex at z, L_i, is calculated as:

$$L_i(z) = C_i exp(\frac{-(z_i - z)^2}{2\sigma_i^2}) \tag{4.6}$$

Where z_i is the z value of the track's DCA point to the beam-line, C_i is a constant, and σ_i is the error in the extrapolation of the track to the beam-line. All the likelihoods are combined into a truncated cumulative likelihood, $L^c(z)$, with a truncation value of c = 1.5 cm. This truncation value is the minimal separation between two vertices that PPV is able to find.

$$L_c(z) = \prod_i^{tracks} (L_i^c(z))^{wi} \tag{4.7}$$

$$L_i^c(z) = L_i(z), |z - z_i| < c$$

$$L_i^c(z) = L_i(z_i + c) \equiv C_i, |z - z_i| > c$$

By setting $L_i^c(z)$ to C_i for z values with no tracks within 1.5 cm, the minimum cumulative likelihood is a constant value. The first vertex candidate is the z value with the maximum cumulative likelihood. All tracks which extrapolate to within 3 cm of this location are associated with this vertex and removed from the pool of available tracks. This process is repeated with the remaining tracks until there are not enough tracks left to create further vertex candidates. Ranks are assigned to the vertex candidates based on their likelihood and number of matched tracks. Vertices with two or more matched tracks are given a rank that consists of their cumulative likelihood plus a large offset, vertices with a single matched track are given their cumulative likelihood as their rank and vertices with no matched tracks are given a rank of their cumulative likelihood minus a large offset. This offset allows the different categories of vertices to be easily distinguished from each other, but saves them so that they can be better analyzed

in post-processing. Up to five vertices without any matched tracks are saved as some STAR triggers are forward focused, which means the probability of two tracks pointing to the fast detectors for a real triggered event is low. All vertices with two or more matched tracks are saved.

The x and y values of the vertex position are determined using the beamline and the z position of the vertex. The vertex with the highest cumulative likelihood is set as the default (primary) vertex. All other vertices are saved in order of descending likelihood.

There is a consistent check of the PPV performance in different luminosity. In 2008, the luminosity is a factor of 4 larger than in 2006. The vertex finding efficiency obtained by PPV shows big difference in different trigger. The high-tower trigger which requires a large energy deposition in one of the BEMC towers in Run06 is 95.8%, and the efficiency in Run08 is 96.2%. They are fairly consistent with each other. The mb trigger which defines as two proton beams arrival at the same time and fire one of the forward detectors is 48.0% in Run06. The efficiency increased to 56.3% in Run08. Vertex precision investigation can be carried out by comparing the software vertex and the hardware vertex. The VPD detector can measure the z position of the vertex from the time difference between east and west side VPD hits, which is totally independent of the PPV vertex finder. The software vertex and hardware vertex comparison shows $\sim$80% of the vertices were within three sigma of each other. The remaining 20% were mostly coming from the in-bunch pile-up impact on VPD. The in-bunch pile-up will cause the VPD to find a vertex midway between two collisions in the same bucket.

The discussion above has shown that the vertex finding efficiency is large and no luminosity dependence for High tower trigger. Once there is a track fired a BHT1 tower, then the vertex, which associated with this track, can be taken as a true vertex. Thus, the primary vertex used in the BHT1 J/ψ analysis is a safety vertex to use. The vertex ranking algorithm shows that ranking larger than 0, most of the time, means two or more tracks matched with a fast detector. In the proton-proton collisions, the fast detector match actually is dominated by BEMC hits. As we mentioned, the Run11 events was taken in high instantaneous luminosity runs and lots of pile-up events have been recorded in the trigger events. A ranking > 0 cut was suggested for pile-up rejection for those non-high-tower triggered events. However, one should keep in mind, by requiring ranking > 0 for vertex, it means two or more tracks were matched with BEMC, and these two tracks have a very high track quality. The definition of the truncated likelihood of the track belonging to a primary vertex in equation 4.7 basically tells that track with a small DCA value are more likely originate from the vertex rather than from pile-up track.

4.4.2 Charged-particle multiplicity measurement

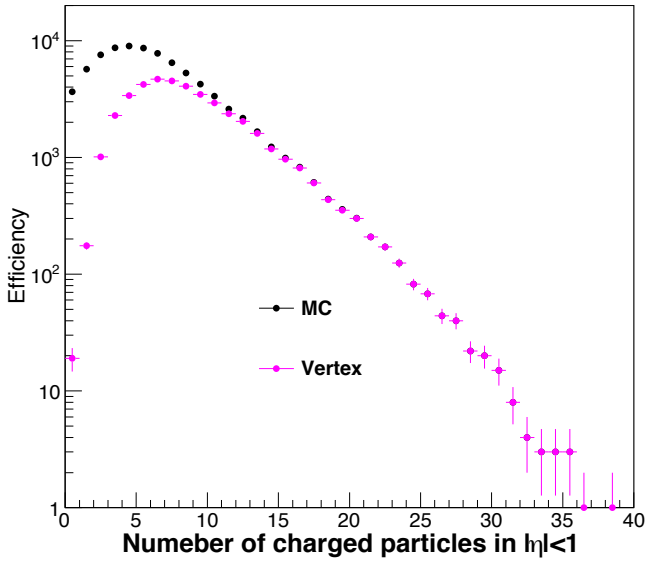

Figure 4.27: Charged-particle multiplicity distributions from Pythia events and reconstructed events with a valid vertex.

The charged-particle multiplicity measurement becomes complicated in a pile-up rich event. Not only the identification of pile-up tracks from primary tracks becomes difficulty, but also the mass of pile-up tracks can introduce a false vertex, which makes the measurement be wrong at the beginning. Normally, a ranking larger than 0 cut is used to select the right vertex. However, the ranking cut will bias the charged-particle multiplicity. A simulation study has been carried out on the charged-particle multiplicity distribution difference by placing the ranking cut. This simulation was carried out in proton-proton collisions at $\sqrt{s}$ = 500 GeV in Run09 STAR geometry. The event generator is Pythia6 by using the Perugia tune, which has shown a good agreement on charged-particle multiplicity between data and simulation at vast collisions energy range. The mean charged-particle multiplicity for min-bias triggered events is about 6.62. The mean value becomes 8.57 after applying the ranking large than 0 cut. The enhancement is about 29%. Figure 4.27 shows the charged particle multiplicity distribution in proton-proton collisions at $\sqrt{s}$ = 500 GeV. The black dots show the true charged-particle multiplicity distribution from Pythia6 simulation. The magenta dots requires a vertex be reconstructed and the ranking of this vertex should large than 0. The ranking cut mainly cut off the low multiplicity events. Events with 10 charged particles or less will be cut off by requiring ranking larger than 0. However, one should notice that the 29% enhancement may not exactly right. In the ranking algorithm, BEMC and EEMC matched information are used to change track's weight. However, EMCs have

different sensitivity to different particle species. When using simulation to study the ranking cut efficiency, the particle's component in the simulation should be the same, at least close to, particle's component in the data. This needs a systematic study on the Pythia6. Thus, in the Charged-particle multiplicity measurement, we need avoid the ranking cut. At the same time, the reliability of vertex should be held.

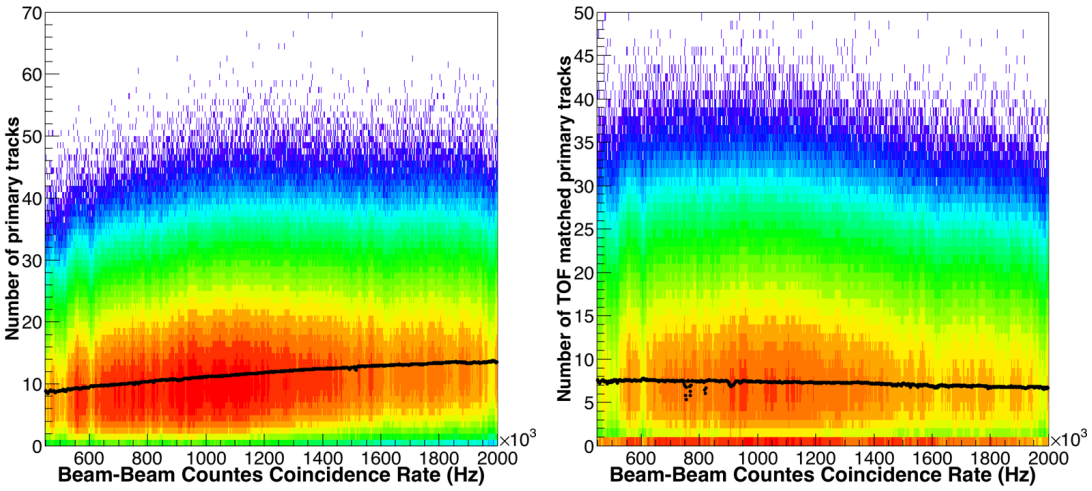

Figure 4.28: Left: number of primary tracks as a function of BBC coincidence rate, Right: number of TOF matched primary tracks as a function of BBC coincidence rate. Both primary tracks are associated with the default primary vertex.

In this analysis, the charged-particle multiplicity measurement is carried out in two different trigger events: events with a J/ψ produced and events from non-single diffractive p+p collisions. The data set for events with a J/ψ produced is using BHT1 trigger events. As we have talked at last section, the vertex finding efficiency is very high in the BHT1 events. Furthermore, if a J/ψ signal has been reconstructed in an event, then the primary vertex in this event should be the vertex that fired the trigger. As for the min-bias triggered events, we used the dataset from Run09. A low luminosity run was taken at 2009 by using BBCMB trigger. The Beam-Beam counter coincidence rate is a factor of 40 lower than in Run11. Thus, only few pile-up events in an event, which gives the confidence to the reliability of primary vertex.

The primary charged-particle tracks have been mixed with pile-up tracks. The pile-up effect can be easily observed in the number of the primary tracks as a function of the Beam-Beam Counter coincidence rate which indicates the instantaneous luminosity at STAR. A high BBC coincidence rate means a high luminosity. In the left panel of Figure 4.28, the number of primary tracks versus BBC coincidence rate is shown. The number of tracks is accounted in the pseudo-rapidity interval of $|\eta|< 1$, and all tracks have been applied basic track quality requirement. The black dots on plot are the mean value of number of primary tracks in each BBC coincidence rate. In Run11, we have a

very large BBC coincidence rate range, which starts from 450k to 2M Hz. The increasing trend of the mean value indicates that pile-up tracks do reconstructed as primary tracks. Hence, a substitute of the primary charged-particle multiplicity is needed. In this analysis, a fast detector matching method is used to reject pile-up tracks. In the right panel of Figure 4.28 shows the number of TOF matched tracks versus BBC coincidence rate. The black dots show the mean of the number of TOF matched tracks in each BBC rate bin. Here, TOF matching means the tofmatchflag > 0. The mean value almost insensitive to BBC coincidence rate. The slight decreasing of the mean is caused by the decreasing of track reconstruction efficiency. At high luminosity range, TPC will record more pile-up tracks, which means a higher TPC occupancy. Hence, the track reconstruction efficiency will decrease as the luminosity increasing.

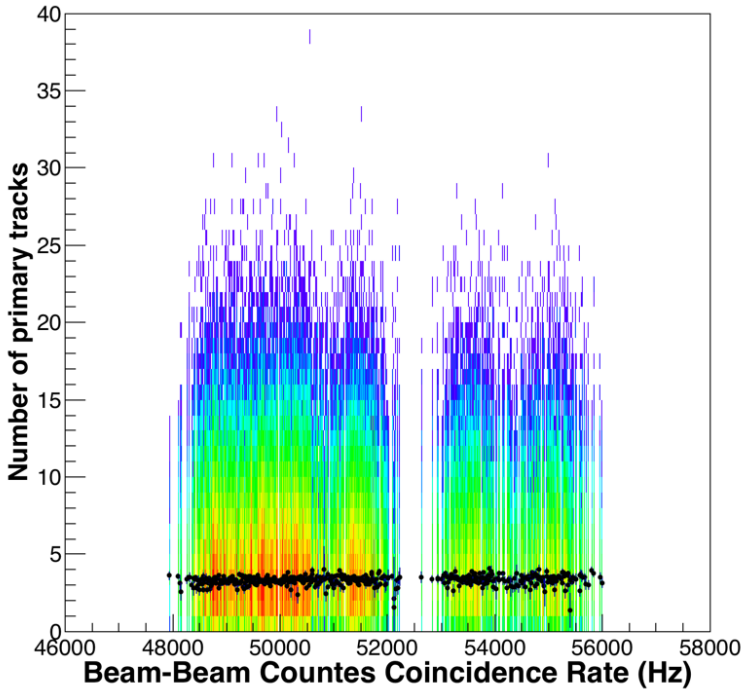

Figure 4.29: Number of primary tracks as a function of BBC coincidence rate.Black dots indicate the mean value of primary tracks in each BBC coincidence rate bins.

In the meaning time, a tight DCA cut is applied on tracks in Run11 charged-particle multiplicity measurement. There are thousand global tracks in the BHT1 trigger events, while the TOF module number is about 4000. There is a big probability that a pile-up track can project to a TOF hit, and associated with the hit. Another additional constraint is needed to reject this kind of random match. As we have mentioned in the vertex finding section, a track with a small DCA is more likely coming from the vertex rather than originated from the pile-up event. Hence, in the Run11 measurement, a DCA < 0.5 cm is applied on top of the TOF matched requirement. While in the Run9 analysis, a relative loose DCA cut of DCA < 1 cm is applied. In Run9, the BBC coincidence

Table 4.8: Track cuts for charged-particle multiplicity measurement in Run11 and Run09

Cut name	Run11	Run09
nHitFit	≥ 15	≥ 15
p_T	> 0.2 GeV/c	> 0.2 GeV/c
η	$\|\eta\| < 1$	$\|\eta\| < 1$
dca	dca < 0.5 cm	dca < 1 cm
TOF matching	tofmatchflag > 0	tofmatchflag > 0

rate is about 40 times lower than in Run11. The pile-up effect is much less in Run09. The number of primary tracks as a function of the BBC coincidence rate is shown in Figure 4.29. From the Figure 4.29, the mean number of primary tracks shows a constant value for the default vertex. Hence, in this luminosity range, the vertex finder has the power to find the right vertex. One may notice the mean value of the number of primary tracks in Run9 is about $\sim$3.5, while the mean value of the number of TOF matched primary tracks is about 7.5 in Run11. With additional TOF match requirement, the mean value is even increased in Run11. There are two reasons, one is the TOF was not fully installed in Run09. Only 79% was installed at Run09. The other reason is the in-bunch pile-up. The number of bunches in RHIC is the same in Run9 and Run11. The difference is the number of ions in each bunch. In Run9 the max number is about 600×10^9 protons per bunch, while in Run11 the max number of ions per bunch has been increased a lot, from beginning of 1600×10^9 per bunch to end of 14700×10^9 protons per bunch. The increasing is not only in the BBC coincidence rate, also increased the probability of in-bunch pile-up. Hence, the mean value of the number of primary tracks in Run9 is even lower than the number of TOF matched tracks in Run11. This is a result of real collisions.

In conclusion, the number of TOF matched tracks used as a substitute measurement of charged-particle multiplicity in the events. The track quality cuts, as well as the TOF matching criteria for Run11 and Run09, are listed in Table 4.8. There is another potential difference between MB events and the events with a J/ψ produced. In the events with a J/ψ, it has two tracks to reconstructed a J/ψ signal, which is taken into account when doing the efficiency correction.

4.4.3 J/ψ measurement

In the analysis of J/ψ versus charged-particle multiplicity, J/ψ signal is reconstructed by the same dataset as in the J/ψ transverse momentum spectrum measurement. In the spectrum measurement, to achieve a high J/ψ statistics, no vertex cut is utilized on events. The efficiency and acceptance correction is mainly applied on electron. How-

ever, the correction for the charged-particle multiplicity is much complicated than J/ψ measurement. A uniform acceptance can simplify the efficiency correction. The study of the embedding data has shown that track within the range of $|\eta| < 1$ will have a very uniform acceptance if applied a vertex cut of $|V_z| < 50$ cm. Hence, a vertex cut of $|V_z| < 50$ cm is utilized to the primary vertex.

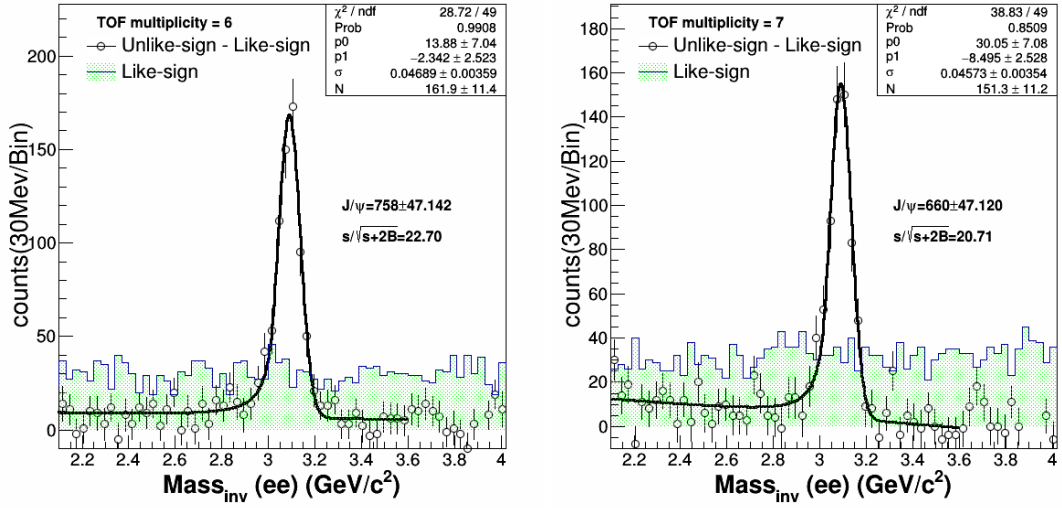

Figure 4.30: J/ψ signals in two different TOF multiplicity bins. Green filled histograms are the Like-sign background. Open circles are the Unlike-sign minus Like-sign signals. Black curves are fitting to open circles using crystal ball function with an exponential function to describe the residual background.

The J/ψ reconstruction method is the same as mentioned in the J/ψ spectrum measurement. The DCA cut for "EMC+TPC" electron keeps the same in this analysis, as the J/ψ signal requirement is already a very strong constraint for the pile-up tracks. Hence, the electron selection criteria are the same as been listed in the Table 4.4. Since the TOF detector is used in the charged-particle multiplicity measurement, one needs to reject events which the TOF detector was not included during the data token. Lots of 0 TOF matched bin have appeared as shown in the right panel of Figure 4.28. Those runs need to be rejected in this analysis. After applied the vertex cuts and a basic QA on TOF detector, the total reconstructed J/ψ account is about 6500. Figure 4.30 shows the J/ψ in the TOF multiplicity bin of 6 and 7. Green filled histogram is the like-sign background. Open circles are the unlike-sign minus Like-sign signals. Black curve is the fitting result of open circles by using a crystal ball function and an exponential function to describe the residual background. A large significance is obtained in this two bins with a number of 22.7 and 20.7 separately, and it has a very good statistics with 758 and 660 J/ψ in each bin. In this two plots, no transverse momentum cuts were placed. The J/ψ p_T basically starts from 4 GeV/c. The good statistics of J/ψ leave room for the study of p_T dependence of J/ψ distribution as a function of charged-particle multiplicity.

In this analysis, the J/ψ yield extraction has been divided into two p_T ranges, which be called low p_T J/ψ and high-p_T J/ψ. The low p_T starts from 4 GeV/c to 8 GeV/c. The high-p_T J/ψ starts from 8 GeV/c. Figure 4.31 has shown the raw J/ψ yield in different p_T bins as a function of TOF matched multiplicity. The solid circles show the p_T integrated J/ψ counts as a function of TOF matche multiplicity. The open circles show the low-p_T range J/ψ. The open boxes show the high-p_T range J/ψ. The maximum TOF multiplicity bin is 18.

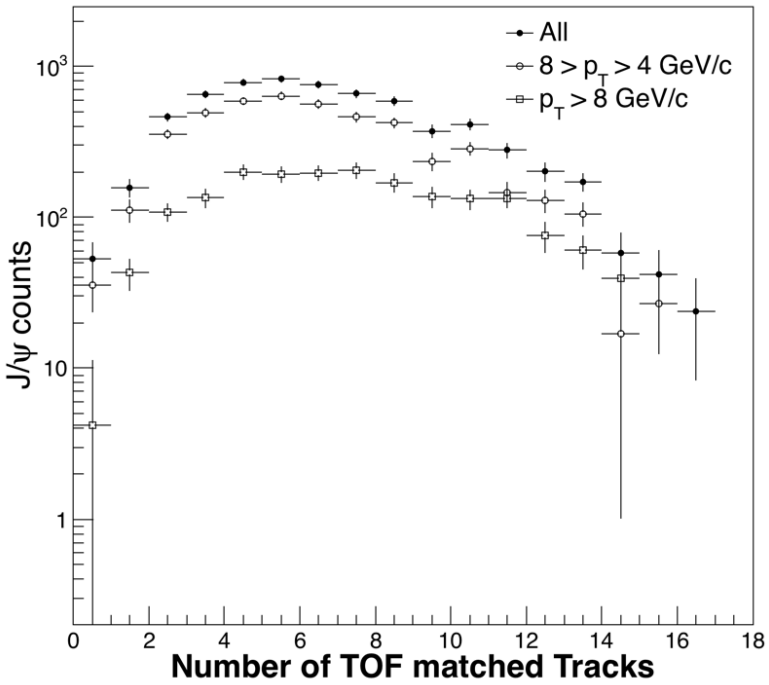

Figure 4.31: J/ψ raw counts as a function of TOF multiplicity. The solid circles show the all p_T range J/ψ. The open circles show the low-p_T range J/ψ. The open boxes show the high-p_T range J/ψ.

4.4.4 Efficiency and acceptance

4.4.4.1 Tracking efficiency and acceptance

The efficiency and acceptance correction for the charged-particle multiplicity is a multi-track correction. The luminosity is not a constant value during Run11, as indicated in the BBC coincidence rate, which is a factor of 5 difference. Hence, the tracking efficiency in different BBC coincidence rate is also different due to different TPC occupancy. The acceptance of track is not only rely on the η of this track but also rely on the vertex position. An event with a certain number of charged-particle produced, the acceptance will have very big difference by placing the vertex in different z position. The tracking efficiency also has p_T dependance. Thus, the tracking efficiency and ac-

ceptance of each track is a function of luminosity, vertex z position, pseudo-rapidity as well as transverse momentum.

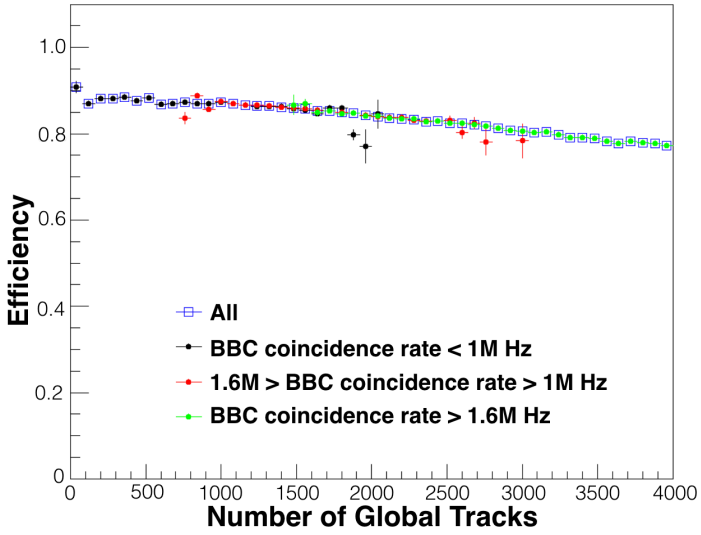

Figure 4.32: Tracking efficiency as a function of number of global tracks. Three different BBC coincidence rate bins are also shown in black, red as well as green. The integral in BBC coincidence rate is shown in blue open boxes.

In this analysis, we required 12 embedding data samples, 6 data samples in Run11 and 6 data samples in Run09. In Run11, pion, kaon, proton and its anti-particle embedding samples were required. Each event has been embedded 5 particles. The embedded pion has flat distribution in transverse momentum with a kinematic range of $0 < p_T < 15$ GeV/c. The distribution in η and ϕ are within $|\eta| < 1.2$ and $0 < \phi < 6.29$ respectively, also with a flat distribution. Other particles have the same kinematic range and distribution. The embedding method is the same as used in J/ψ embedding. For Run09 embedding data samples, the embedded particle species is also pion, kaon, proton and corresponding anti-particles. The kinematic is also the same as in Run11 embedding, but using Run09 data sample.

In this analysis, we use number of global tracks to indicate the luminosity. Figure 4.32 shows the pion tracking efficiency as a function of a number of global tracks. The track quality requirement for reconstructed tracks are nHitFit ≥ 15, $p_T > 0.2$ GeV/c, $|\eta|<1$ as well as DCA < 0.5 cm. For a consistent check, three different BBC coincidence rate bins are also shown in black, red, and green. The first BBC coincidence rate bin is the BBC coincidence rate less than 1M Hz, the second bin is in the range of 1M Hz to 1.6 M Hz, the final bin requires BBC coincidence rate is larger than 1.6M Hz. The integration of the BBC coincidence rate is shown in blue open boxes. As we can get from the efficiency, all those efficiencies are consistent with each other in the overlapping range. This indicates that the number of global tracks is a good indicator of the

luminosity. The efficiency is close to 90% with the number of global tracks less than 500. The efficiency drops to 80% with the number of global tracks increased to 4000. The tracking efficiency difference is about 10%.

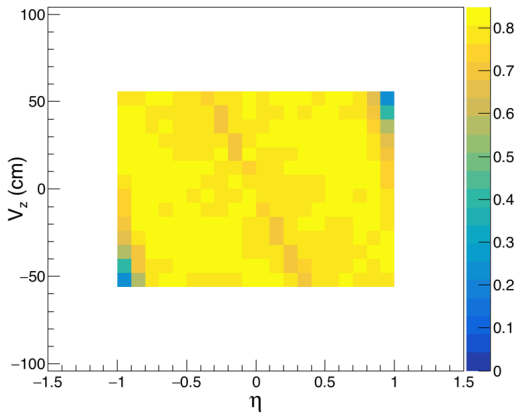

Figure 4.33: Two-dimension tracking efficiency as a function of track's η and event's vertex z position.

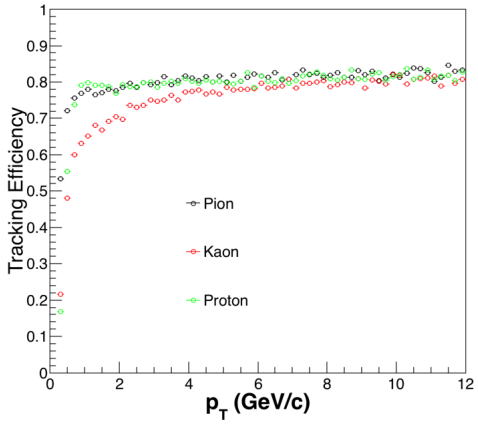

Figure 4.34: Tracking efficiency as a function of transverse momentum for pion, kaon, and proton.

The track's η and vertex z position together affect the track's acceptance. Figure 4.33 shows the two-dimension efficiency of pion as a function of η and vertex z position. The average efficiency is about 80%. Measurement without the range of $|\eta| < 1$ is not shown in the plot. All reconstructed tracks are required the track quality as in the luminosity study. The proton and and kaon's two-dimension efficiency has a similar distribution with pion. At the corner of lower-right, which has a vertex value of 50 cm and track η of -1, a very large efficiency dropped can be seen. Below this range the efficiency decreased rapidly. Figure 4.34 shows the tracking efficiency as a function of transverse momentum for pion, kaon, and proton. All those particles has a consistent tracking efficiency at high p_T range. Pion and proton tracking efficiency saturated at about 1GeV/c. Kaon due to decay contribution shows a gentle increasing in tracking efficiency as p_T increased.

In general, the particle's tracking efficiency is a function of luminosity, η, vertex z position, as well as particle's transverse momentum. The η and vertex z both affect the tracks acceptance. Hence, tracking efficiency is tried to be expressed as three factor: number of global track, (η,V_z), as well as transverse momentum. An independence check of those three factor has been carried out, which shows no correlation among those three factor, and they can be treated independently. Normally, the tracking efficiency is expressed as a function of transverse momentum, then the efficiency as a function of number of global tracks need to be normalized. The efficiency as a function of number

of global tracks is scaled by the average efficiency. The efficiency as a function of η and vertex z position also scaled by average efficiency. Then the signal track tracking efficiency can be expressed as followed:

$$\begin{aligned}\epsilon(l;\eta;V_z;p_T) &= \epsilon'(l)\epsilon'(\eta,V_z)\epsilon(p_T) \\ &= \epsilon'(N_{global})\epsilon'(\eta,V_z)\epsilon(p_T)\end{aligned} \tag{4.8}$$

$\epsilon'(N_{global})$ is luminosity factor, which is the efficiency shown in Figure 4.29 and normalized by average efficiency. $\epsilon'(\eta,V_z)$ is geometry factor, which is the efficiency shown in Figure 4.33 and normalized by average efficiency. The $\epsilon(p_T)$ is the tracking efficiency as a function of transverse momentum, which is shown in Figure 4.34.

4.4.4.2 TOF matching efficiency

The TOF response is not well simulated in the embedding, so the TOF matching efficiency has to be calculated from data. The TOF matching efficiency is normally calculated as the number of TOF matched track divided by the number of primary tracks that passed the track quality and acceptance cuts:

$$\epsilon_{TOFmatching} = \frac{N_{TOF}}{N_{TPC}} \tag{4.9}$$

However, this procedure becomes complicated with pile-up tracks. The denominator N_{TPC} has lots of pile-up tracks even in primary tracks at high luminosity runs. According to this formula, the TOF matching efficiency will lower than the true value with pile-up track in the primary tracks. So another fast detector matching is employed to extract TOF matching efficiency. BEMC normally is the additional fast detector. Then the denominator becomes number of BEMC matched tracks, and the numerator is the number of tracks with both BEMC and TOF matching. Then the TOF matching efficiency is:

$$\epsilon_{TOFmatching} = \frac{N_{BEMC\&TOF}}{N_{BEMC}} \tag{4.10}$$

However, there is a potential assumption that the BEMC and TOF are totally independent, especially in the acceptance. Otherwise, a correlation factor is needed in the efficiency calculation. If there is no correlation between BEMC and TPC, the TOF efficiency from equation 4.9 and equation 4.10 should be the same in the pile-up free events. In Run09 low luminosity, the BBCMB trigger events are used to test this two TOF matching efficiency. Figure 4.35 left side shows the TOF matching efficiency mentioned above. The black dots show the TOF matching efficiency obtained from BEMC matching method. The Blue boxes show the TOF matching efficiency obtained from the traditional TPC method. In Run09, only part of the TOF detector was installed. The TOF matching efficiency is about 45% from the traditional TPC method as defined

in equation 4.9. The TOF matching efficiency obtained by BEMC matching method is systematic higher than the traditional TPC method which indicates a correlation. Figure 4.35 right plot shows the TOF matching efficiency enhancement factor by using BEMC matching method. The efficiency enhancement has a constant value with p_T large than 0.5 GeV/c. We can extract the TOF matching efficiency in the Run11 data sample by using the efficiency enhancement factor obtained from the Run09 data set.

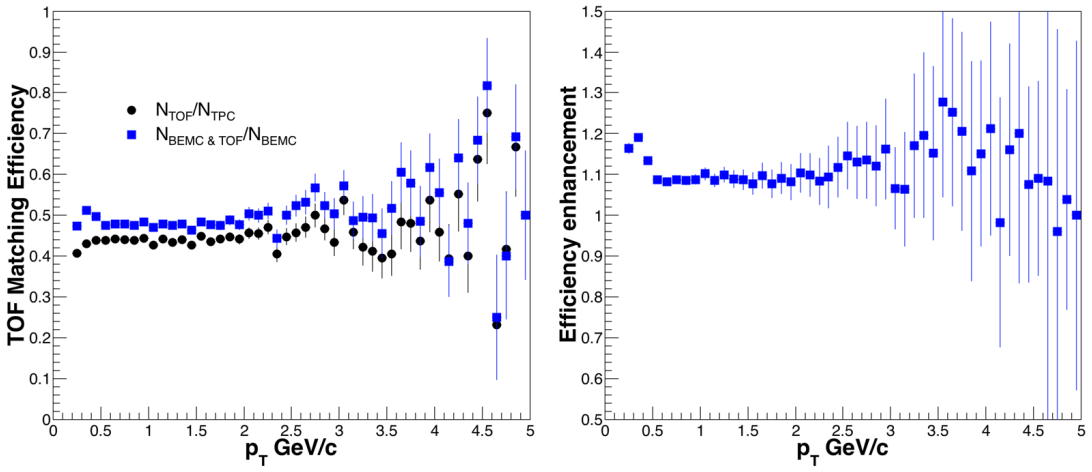

Figure 4.35: Left: TOF matching efficiency by using two different methods, black dots shows the TOF matching efficiency obtained from BEMC matching method. The Blue boxes show the TOF matching efficiency obtained from the traditional method. Right: the efficiency enhancement factor of BEMC matching method.

To extract the TOF matching efficiency correctly, an appropriate data set is needed. BHT1 trigger events actually is not a suitable data set for applying the TOF matching efficiency enhancement factor. The charged-particle multiplicity in proton-proton collisions in the η range of $|\eta| < 1$ is about 7. BHT1 trigger events by definition will have a large energy deposited in BEMC. Then BHT1 events are partially biased in the BEMC acceptance. The TOF matching efficiency obtained in BHT1events will contain a potential BEMC enhancement. If we applied efficiency enhancement factor obtained in Run09 on the TOF efficiency, it could overestimate the TOF matching efficiency. The more suitable data set would be an MB data set or the same kind of BBCMB trigger data. However, BBCMB event's vertex validity will be a problem. VPD is a fast detector, and it can measure the vertex position independence. Vertex information from VPD could be an additional constraint on the vertex. In the TOF matching efficiency analysis, a vertex difference between VPD vertex and vertex from vertex finder less than 3 cm is placed. The vertex selection criteria are valid vertex, $|V_z^{TPC} - V_z^{VPD}| < 3$ cm, as well as $|V_z^{TPC}| < 50$ cm. Then, TOF matching efficiency can be extracted from Run11 BBCMB data by using the efficiency enhancement factor obtained from Run09.

However, as mentioned, BBCMB and BHT1 data sets have different acceptance to TOF. The efficiency enhancement factor would not exactly the same in this two different triggers. Here, another method is used to extract the TOF matching efficiency. The DCA value from equation 4.7 indicates the possibility of track originated from the certain vertex. By tightening the DCA value, it will reject the pile-up tracks. Figure 4.36

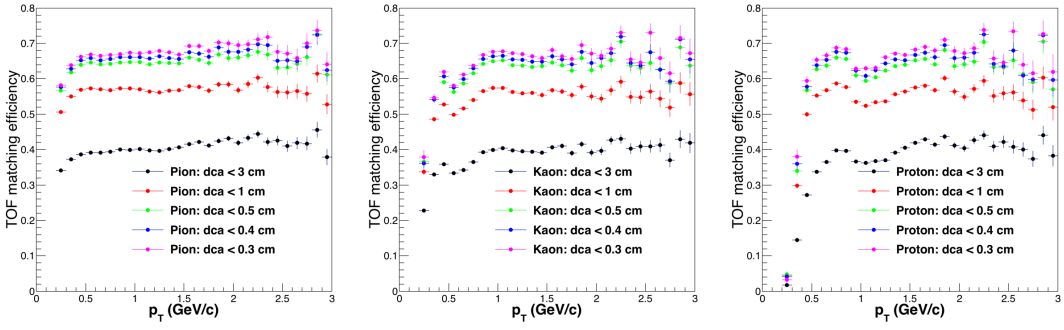

Figure 4.36: TOF matching efficiency for pion (left), kaon (middle), and proton (right),with different DCA cuts. All tracks are required basic track quality except the DCA value.

shows the TOF matching efficiency evolution of different particle species by tightening DCA cut. The pion sample is selected by requiring n$|\sigma_\pi| < 0.5$ with the track quality cuts. The kaon and proton are the same as for pion selection but change the nσ to the corresponding particle's nσ value. As shown in the pion TOF matching efficiency, by tighten the DCA value from 3 cm to 0.3 cm, the TOF matching efficiency increased and shows saturation at very tight DCA cuts, which indicates that most of the pile-up tracks have been rejected. The TOF matching efficiency is about 68% for pion with p_T large than 0.5 GeV/c. The TOF matching efficiency shows saturation for kaon with p_T large than 0.7 GeV/c. The low efficiency below 0.7 GeV/c is due to the decay of kaon. For proton, the TOF matching efficiency dropped a bit at about 1 GeV/c. This is caused by contamination from other particles.

Here a consistent check is made. In Run09, the BBCMB dataset has same issue with calibration of dE/dx. This dataset can not provide the nσ information. Hence, we compare the hadron TOF matching efficiency obtained from this two different methods. The black dots show the TOF matching efficiency obtained from BEMC matching method. The red dots show the TOF matching efficiency obtained from tighten DCA method. The efficiency consistent with each other with $p_T > 0.4$ GeV/c. The tighten DCA method has relative high efficiency wth p_T less then 0.4 GeV/c. This difference at low p_T is coming from the efficiency enhancement factor. In such a low p_T range, we need thinking about the reliability of BEMC matching method. As we have mentioned in the BEMC detector, most hadrons are MIP particles, the energy deposition in BEMC is about 300 MeV. This energy loss is very close to the particle's transverse momentum. The rejection power of BEMC matching may not reliable at low p_T range. The

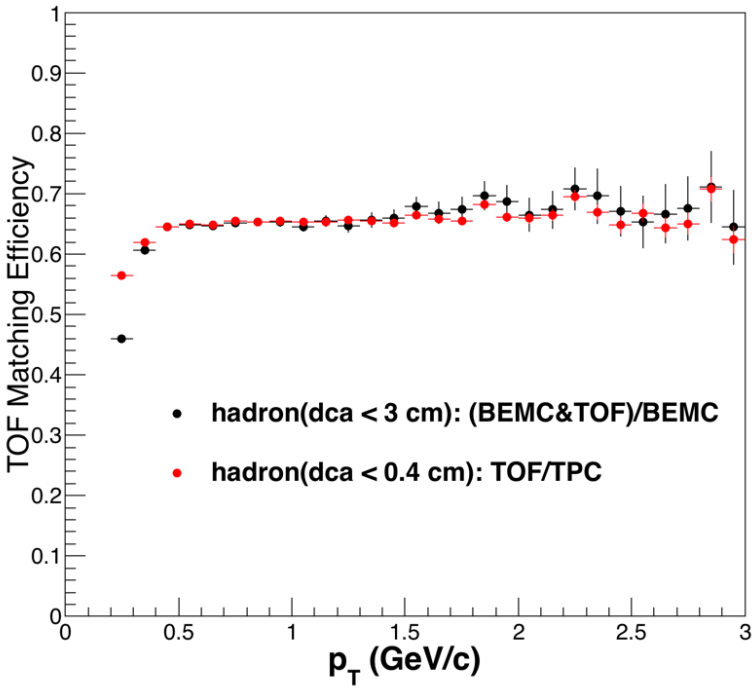

Figure 4.37: TOF matching efficiency as a function of transverse momentum. The black dot show the TOF matching efficiency obtained from BEMC matching method. The red dot show the TOF matching efficiency obtained from tighten DCA method.

TOF matching efficiency shape extracted by tighten DCA cuts is more close to the TOF matching efficiency extracted in the Run09 low luminosity.

In general, we compared the TOF matching efficiency extracted by two different method. The BEMC matching method and tighten DCA method gives a consistent TOF matching efficiency with p_T above 0.4 GeV/c. The validity of BEMC matching method at p_T < 0.4 GeV/c needs more study. In this analysis, we used the TOF matching efficiency extracted from tighten DCA method.

4.4.4.3 Unfolding

The main ingredients of this analysis are the raw data distributions for both BBCMB and BHT1 events, which can be named as M spectrum, and the corresponding matrix M, which allows the unfolding of true primary spectrum from the raw. Then the relationship between measured spectrum M, the true charged-particle multiplicity, and the response matrix R can be expressed as follow:

$$M = RT, \tag{4.11}$$

In this analysis study, we need infer the true charged-particle multiplicity (T) for both BBCMB events and BHT1 J/ψ charged-particle multiplicity from the corresponding measured (M) distribution. R is a matrix and each of the matrix element R_{mt} describes

the probability that an event with true multiplicity t is measured as an event with the multiplicity m. In the following, the matrix R will be called response matrix. The response matrix contains all response of detector, which including all tracking efficiency discussed above. Naively, the true distribution can be obtained by the inversion of the matrix and measured distribution M, which can be expressed as $T = R^{-1}M$. However, there are two issues of this inversion procedure. First of all, by using the inverted matrix means the response matrix is not a singular matrix. But this is not guaranteed to be true. Such as the detector has poor resolution, then the two rows of the matrix can be identical. The second is the resolution of the spectrum can create non-physical fluctuations. This can be illustrated in Figure 4.38. Let's consider that response matrix R can be inverted. In the left panel of Figure 4.38, the black line shows the measured distribution and the histogram is the binned sample from black curve. Using the equation $T = R^{-1}M$, in the right panel of Figure 4.38, the black line shows true distribution. The histogram shows the unfolded distribution which is obviously not the true distribution. This kind of oscillating structure in the unfolded T distribution can be a result of statistical fluctuation, which caused by the limited number of measured events or events used to create the response matrix. In the unfolding process, the limitation of statics could result in a bad

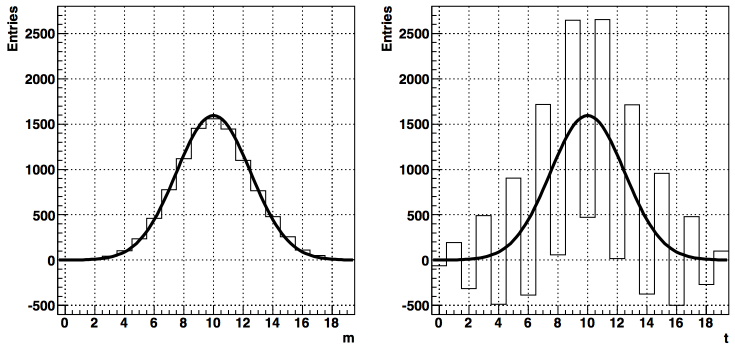

Figure 4.38: In the left plot, the black line shows the measured distribution and the histogram is the binned sample from black curve. In the right plot, the black line shows true distribution. The histogram shows the unfolded distribution.

resolution either on measured spectrum or response matrix. To work around the non-physical fluctuations, an constraint is placed to the result. This constraint rely on the priori knowledge of the distribution. In this analysis, we use Bayesian unfolding which is an iterative method based on Bayes' theorem. It implicitly regularizes the solution by limiting the number of iterations.

The Bayesian unfolding states that the conditional probability $P(A|B)$ of A if B is true as follow:

$$P(A|B) = \frac{P(B|A)P(A)}{P(B)}, \tag{4.12}$$

$P(A)$ and $P(B)$ are the independent probabilities of A and B being true. $P(B|A)$ is the probability of B if A is true. In the charged-particle multiplicity measurement, A can be identified as the true multiplicity distribution. B is the measured event with certain multiplicity. $P(B|A)$ is the response matrix of the detector. With these three information be known, One can calculate the $P(A|B)$. By using the nomenclature of R, T, and M, The value in Bayesian conditional probability can written as $P(B|A) \equiv R_{mt}$, $P(A) \equiv T$ and $P(B) \equiv M$. The formula can be rewritten as:

$$\widetilde{R}_{tm} = \frac{R_{mb}P_t}{\sum_{t'} R_{mt'}P_{t'}}, \tag{4.13}$$

P_t is an priori guess of the true distribution, which is obviously not known in advance. The unfolding procedure simply calculates

$$U_t = \sum_m \widetilde{R}_{tm}M_m, \tag{4.14}$$

If $U_t \equiv P_t$ then U_t is the true distribution, otherwise, the process is reiterated using U_t instead of P_t. The process can be iterated for a number of iterations until convergence.

4.4.4.4 Response matrix

The response matrix maps the true distribution into the measured charged-particle multiplicity. However, picture is not that naive. Certain concerns originated from both physical and technologic situation will make it difficult in building the maps. The pion, kaon and proton efficiency obtained in the embedding data can not be directly used on the measured particles. The measured number of TOF matched tracks and TPC tracks are not a single particle species, it has multiple components, and normally are pion, kaon, proton as well as the electron. And different particle species have different tracking efficiencies, as shown in Figure 4.34. Furthermore, the particle identification is aways not that easy in a large kinematic range. Even with a good discriminability at low p_T range, the overlap range will cause double counting issues. Another alternative method to get the total hadron efficiency is mixing the pion, kaon, and proton efficiency according to their yield. However, there is no published results on any of these particle p_T spectrum in p+p collisions at $\sqrt{s}$ = 500 GeV yet. The same case happened to TOF matching efficiency application.

The other issue is the charged-particle multiplicity itself. The charged-particle multiplicity in physics means the number of charged particle been produced just after the collision happens. In other words, the distance between collision point and the particle production point should be 0. Then, the charged-particle multiplicity is not including the particles from decay contribution. While in the measurement, the charged-particle

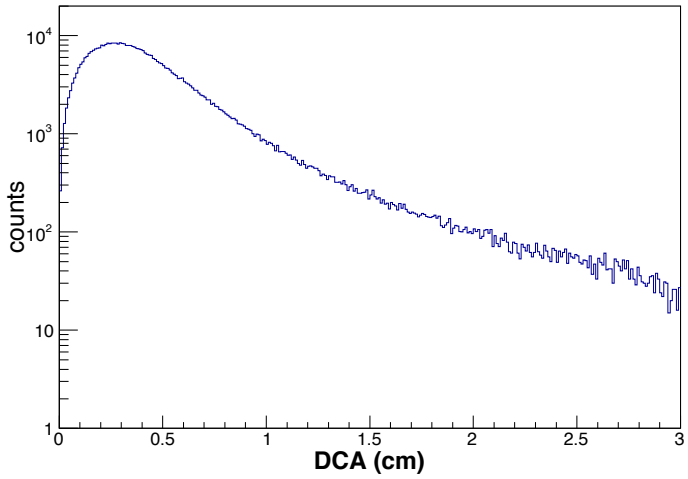

Figure 4.39: The distance of the closet approach between the reconstructed track and the collision point. Tracks are originated from the collision point.

multiplicity is all final states particles, which including decayed contribution. The final states particles are so-called stable particles with a long life time. Furthermore, the reconstructed tracks which originated from the primary vertex will have no 0 DCA value due to the limitation of TPC spatial resolution, as shown in Figure 4.39, the track reconstruction process will smear out the DCA distribution. The mean DCA value of physics primary track is about 0.45 cm. The DCA less than 1 cm cut efficiency is about 90%. On the other hand, particle from decay contribution with a small decay value could also be reconstructed as a primary tracks. While the study of decay particle contributions need a well understand of all different particle's yield. It needs a lots of measurement. Nevertheless, the smearing effect on DCA can certainly fall the secondary particle's DCA into 1 cm. By cutting on certain DCA value, there are more than physics primary tracks be selected, some smeared secondary contributions are also be counted in the charged-particle multiplicity. The data driven method to subtract the secondary contribution is not easy.

All those effects be discussed above need a very good understand of the proton-proton collisions. However, in this energy range, the above concern are lack of systematical research. Hence, we use the PYTHIA simulation to determination concern above. The response matrix is determined by PYTHIA simulation, which also contained some physics information. In this analysis, the follow effect are included in the response matrix: the tracking efficiency, the TOF matching efficiency, the secondary particles from decay contribution.

PYTHIA8 is used to generate both MB events and events with a J/ψ produced. The tune used for J/ψ simulation is STAR-HF Tune: STAR-TUNE which has been

Table 4.9: PYTHIA8 MB events simulation parameters

Parameter name	value	Parameter name	value
Beams: A	proton	Beams:B	proton
Beams: eCM	500 GeV	softQCD: minBias	on

Table 4.10: PYTHIA8 J/ψ events simulation parameters

Parameter name	value	Parameter name	value
Beams: A	proton	Beams:B	proton
Beams: eCM	500 GeV		
PDF:useLHAPDF	on	PDF:LHAPDFset	MRSTMCal.LHgrid
Charomium: all	on	Bottomonium: all	on
PartonLevel: MI	on	PartonLevel: ISR	on
BeamRemnants: priordialKT	on	PartonLevel: FSR	on
StringFlav:mesonCvector	1.5	mesonBvector	3
4:m0	1.43	5:m0	4.3

adjusted to match the STAR existing J/ψ and non-photonic electron p_T distribution. The parameters setting for MB events and J/ψ events simulation are listed in Table 4.9 and Table4.10. The STAR-TUNE is a part of LHAPDF, but with certain PDF setting, which shows a good agreement on J/ψ p_T spectra. All charmonium channels and bottomonium channels are turn on to account for feed-down contributions. The multiple interactions, initial-state radiation as well as final-state radiation has been turned on, among which multiple interactions has been improved mainly affecting processes involving in light quarks and gluons. The relative production ratio for vector and pseudo-scaler of charm and bottom mesons is also set down. The charm quark mass is set to 1.43 GeV, the bottom quark mass is set to 4.3 GeV. In the MB simulation, the default PDF is used.

A consistent check is needed between PYTHIA simulation and data in particle production. However, there is no measurement at collisions energy of 500 GeV, the UA1 experiment was taken data at 546 GeV in proton-antiproton collisions. Figure 4.40 shows the pion invariant cross section as a function of p_T from PYTHIA8 simulation. The open circles are PYTHIA simulation and triangles are measurements from UA1 experiment. The agreement is good with p_T large than 0.5 GeV. Actually, identical result is not expected as the collisions has about 10% difference. In PYTHIA, we may need to define primary tracks. The produced final state particle's DCA, distance between particle produced point and collisions point, is shown in Figure 4.41. Here the final state particles are pion, kaon, proton, and electron. The particle with DCA = 0 cm is just 28.8% of the total final state particles. The reconstructed primary tracks are

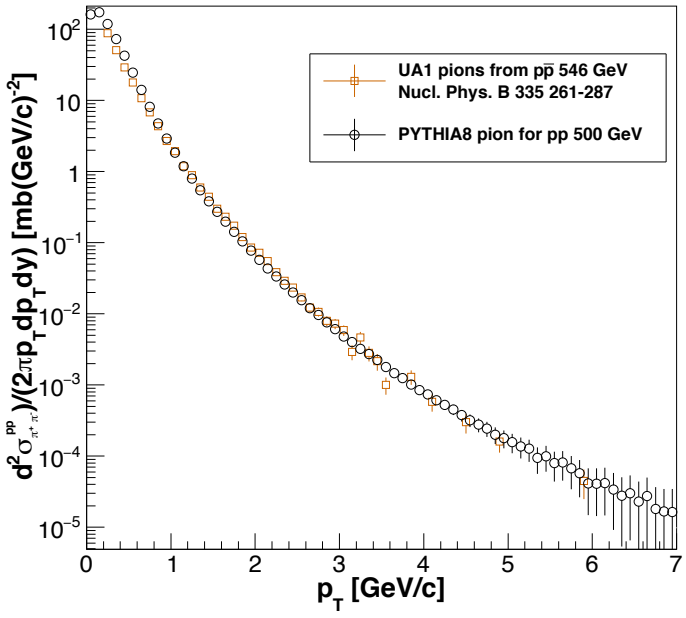

Figure 4.40: The pion invariant cross section as a function of p_T from PYTHIA 8 simulation in proton-proton collisions at $\sqrt{s}$ = 500 GeV and measurement from UA1 experiment in proton-antiproton collisions at $\sqrt{s}$ = 546 GeV.

required to be within 3 cm with vertex. The distance between reconstructed vertex and reconstructed track is determined by reconstructed vertex and reconstructed track spatial resolution. The Figure 4.42 shows the V_z difference distribution, it is the distance

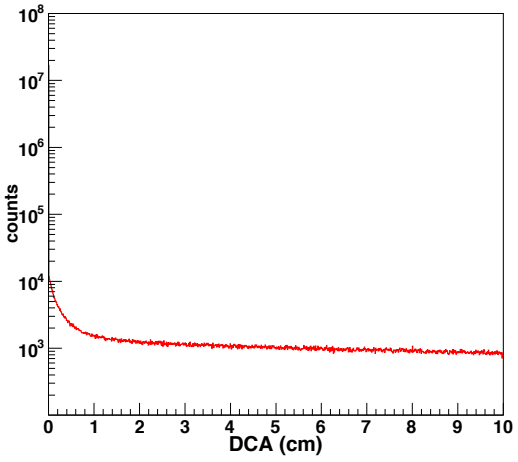

Figure 4.41: The DCA distribution of final state particles. The DCA is defined as the distance between particle produced point and collisions point.

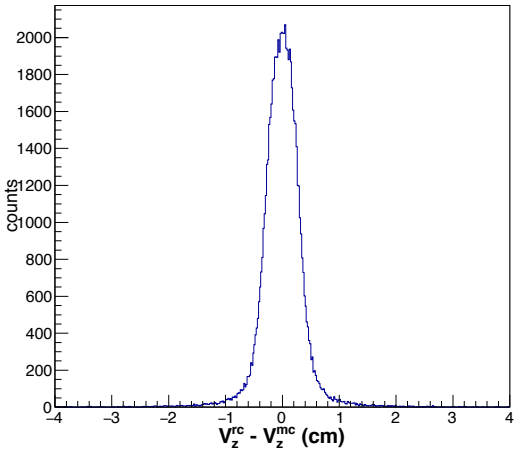

Figure 4.42: The distance of the reconstructed vertex and the Monte Carlo vertex in z direction. The vertex is reconstructed as in the real data reconstruction.

between Monte Carlo vertex and reconstructed vertex. The width of the V_z distribution is about 0.25 cm. Thus, one needs smearing the vertex along z-axis and tracks production point simultaneously. The track's production point smearing is according to the

DCA distribution shown in Figure 4.39. Then the physics primary tracks are defined as tracks with the DCA = 0 cm. The reconstructed primary tracks are defined as tracks with the smeared DCA < 3 cm. In the measurement, the charged-particle multiplicity is measured by requiring a J/ψ be reconstructed. This means in this event there is already has two electron be reconstructed.

The response matrix and unfolding process is processed by a RooUnfold package. It is developed by Tim Ady, Richard Claridge, etc. The training of the response matrix is by filling the number of physics primary tracks and the number of reconstructed primary tracks. In the measurement, there is a p_T cut off, every reconstructed track' p_T needs to be large than 0.2 GeV/c. The cut off is also take into account in the response matrix. We chose the Bayesian unfolding method and the number of iterations is 4.

In general, the response matrix will take care of the tracking efficiency, TOF matching efficiency, secondary particle's contamination as well as particle's p_T spectra cut off. The response matrix in this analysis is not only a response matrix which account for the detector's response, it also includes some physics information. Thus, the unfolded true charged-particle multiplicity distribution will show some model dependence. This part is assigned in the systematic uncertainty, which will be shown in next section.

4.4.4.5 Vertex finding and trigger efficiency

In the BHT1 events, the vertex finding efficiency is more than 96%. Thus the relative efficiency change would be small in different charged-particle multiplicity bins. Furthermore, the J/ψ events normally have a large number of charged particles produced. As one may expected that vertex finding efficiency is a function of charged-particle multiplicity. With more tracks produced, the probability of a vertex be reconstructed is higher. Hence, the vertex finding efficiency for J/ψ is not a big deal, it can largely cancel out each other when taken the yield ratio. The trigger efficiency is obtained by embedding as discussed in the J/ψ p_T spectra measurement.

In Run9 BBCMB events, there is not requirement on BEMC tower firing, the vertex finding efficiency is not guarantee to be high, and should show a charged-particle multiplicity dependence. The BBCMB trigger bias also needs correction as a function of charged-particle multiplicity. Hence, the physics charged-particle multiplicity obtained by using response matrix needs further correction for the vertex finding efficiency and BBCMB trigger bias. The vertex finding and BBC trigger bias are studied by simulation using the PYTHA events. Detector response and all physics process are simulated with GEANT 3, and the event reconstruction is followed the offline production procedure. The PYTHA is in version 6.205 with minimum processes selected and with CDF

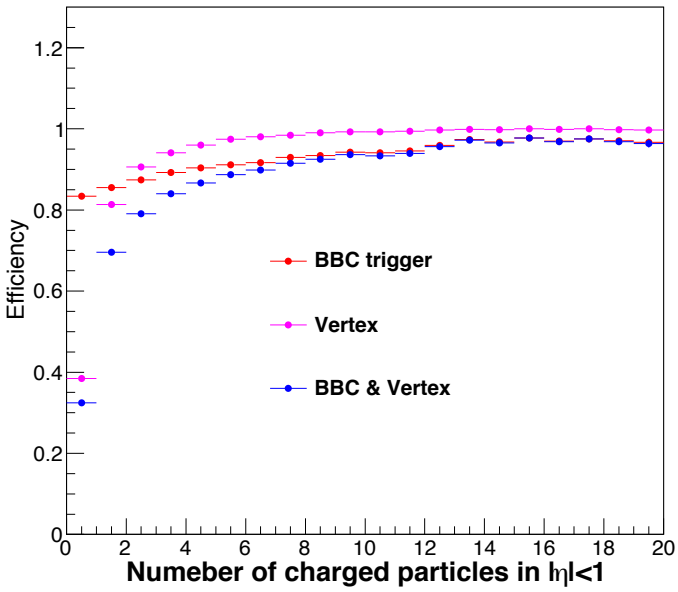

Figure 4.43: The BBC trigger efficiency as a function of charged particle multiplicity are shown in red circles. The vertex finding efficiency as a function of charged particle multiplicity are shown in magenta circles. The BBC trigger together with vertex finding efficiency are shown in blue circles.

TuneA settings. Figure 4.43 shows the efficiency of BBCMB trigger and vertex finding efficiency as a function of charged-particle multiplicity. The BBC trigger efficiency as a function of charged particle multiplicity is shown in red circles. It shows a weak multiplicity dependence. The vertex finding efficiency as a function of charged particle multiplicity is shown in magenta circles. The vertex finding efficiency at low multiplicity has a rapid decrease, the vertex finding efficiency saturated above 7 tracks. The BBC trigger together with vertex finding efficiency is shown in blue circles.

4.4.5 Systematic Uncertainty on J/ψ production versus charged-particle multiplicity

The systematic uncertainties of the final J/ψ production versus charged particle multiplicity are studied. The physics results is a double ratio of J/ψ yields and multiplicities, lots of uncertainties were canceled out each other. In this analysis, the following factors are taking into account: TOF matching efficiency, pion relative yield, as well as uncertainties from unfolding process.

The TOF matching efficiency extracted from tight DCA cut method has been shown in Figure 4.37. The TOF matching efficiency obtained by two different method consistent with each other. However, the tight DCA method may involved some pile-up contamination contribution. As shown in Figure 4.36, there is a systematic trend as the DCA cut getting tighten. This indicates that there still have some contamination after applied the tight DCA cut. Hence, 1% TOF matching efficiency difference is assigned.

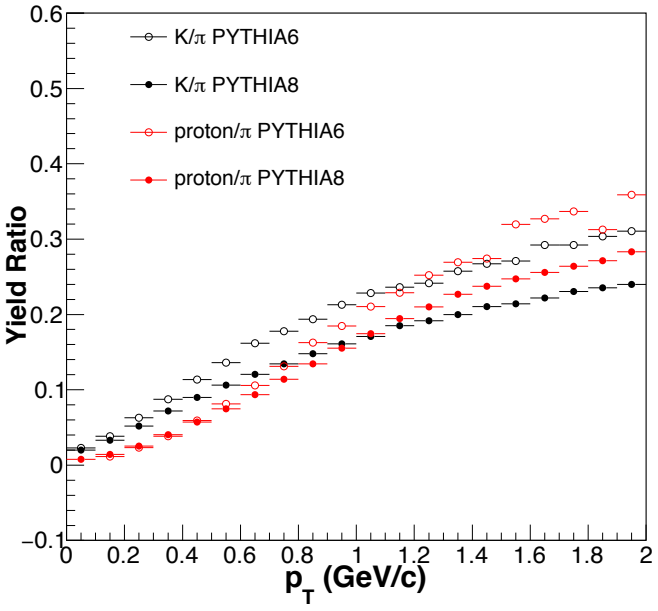

Figure 4.44: The kaon to pion ratio as a function of p_T, the proton to pion ration is also shown. The open circles are the results from PYTHIA6 simulations, and the solid circles are simulation from PYTHIA8 simulations.

Table 4.11: Relative yields systematic uncertainties in different multiplicity bins.

systematic uncertainty	p_T range	bin1	bin2	bin3	bin4	bin5
Total	integral	4.3%	4.1%	2.7%	5.3%	5.6%
	low-p_T	5.7%	4.2%	1.8%	6.0%	8.2%
	high-p_T	4.5%	4.4%	4.8%	8.8%	8.9%

The response matrix has been included some physics processes including the secondary decay contribution and kaon or proton to pion ratio. All these contributions are relay on the PYTHIA8 simulation. A PYTHIA6 simulation is processed as one of the model dependence uncertainty. The PYTHIA6 simulation is only applied in the MB data. Figure 4.44 shows the kaon to pion ratio and the proton to pion ratio from PYTHIA6 and PYTHIA8. The yield ratio for K/π difference is not a small value. This two very different datasets are used to train the response matrix. The finial results difference are assigned as the systematic uncertainties from model dependence.

In this analysis, the regulatisation parameter in Bayesian unfolding specifies the number of iterations, starting with the training sample truth (iterations=0). The regulatisation parameter is chosen to be 4. It is chosen to find the largest value up to which the errors remain reasonable. Here, an iteration of 6 and 8 was applied to compared the with the 4 iteration process in both MB events and J/ψ events. The overall systematic uncertainties of the J/ψ production as a function of the charged-particle multiplicity are listed in Table 4.11.

Chapter 5 Results and Discussion

The J/ψ meson is measured in p+p collisions at $\sqrt{s}$ = 500 GeV at STAR via the di-electron decay channel. The di-electron has a decay branch ratio of 5.9%. A total of 154 million BHT1 events has been analyzed in High p_TJ/ψ spectrum study. The same dataset is also used to study the relative yield ratio of $\psi(2S)$ to J/ψ study. About 1 million BBCMB triggered events token from low luminosity run in Run2009 at the same collision energy has also been analyzed in the J/ψ versus event activity study. The J/ψ reconstruction method, yield extraction method, efficiency and acceptance correction, PYTHIA simulation method, trigger bias study, as well as all analysis details has been discussed in chapter 4. In this chapter, all physics results will be shown and discussed, which includes high p_T spectrum, $\psi(2S)$ yield to J/ψ ratio, J/ψ x_T scaling, as well as the J/ψ production versus charged-particle multiplicity.

5.1 High p_T J/ψ Spectra

The differential invariant cross section of J/ψ production at mid-rapidity is calculated by following formula:

$$B_{ee}\frac{d^2N}{2\pi p_T dp_T dy} = \frac{1}{2\pi p_T \Delta p_T \Delta y}\frac{N_{J/\psi}}{\epsilon \mathcal{L}}, \tag{5.1}$$

where B_{ee} is the J/ψ di-electron channel decay branch ratio. Δp_T is the bin width of each p_T interval. Δy is the measured rapidity range of J/ψ, which is 2 in this analysis. $N_{J/\psi}$ is the number of J/ψ reconstructed in each p_T interval. ϵ is the total J/ψ detection efficiency, which included electron trigger efficiency, electron tracking efficiency as well as the geometric acceptance. $\mathcal{L}$ is the sampled luminosity by BHT1 trigger, which is 22 pb^{-1}. The J/ψ detection efficiency is obtained by embedding technology which simulated the detector response by using GEANT 3 simulation. The systematic uncertainty is estimated by changing cuts in both embedding and data analysis, and the final invariant yield difference is assigned as the systematic uncertainty. The systematic uncertainty on yield extraction is studied by varying J/ψ mass counting range and fitting range. To average out the statistic fluctuation, the bin-by-bin systematic uncertainties is fitted by a constant function in each source. The overall systematic uncertainty for the spectrum is 6.3%, details can be found in Table 4.5.

Figure 5.1 shows the inclusive J/ψ invariant cross section as a function of p_T in proton-proton collisions at $\sqrt{s}$ = 500 GeV at mid-rapidity ($|y| < 1$). The red error bars represent the statistical uncertainties. The red boxes depict the systematic uncertainties. The result is compared with Next-Leading Order NRQCD calculation [117] in the

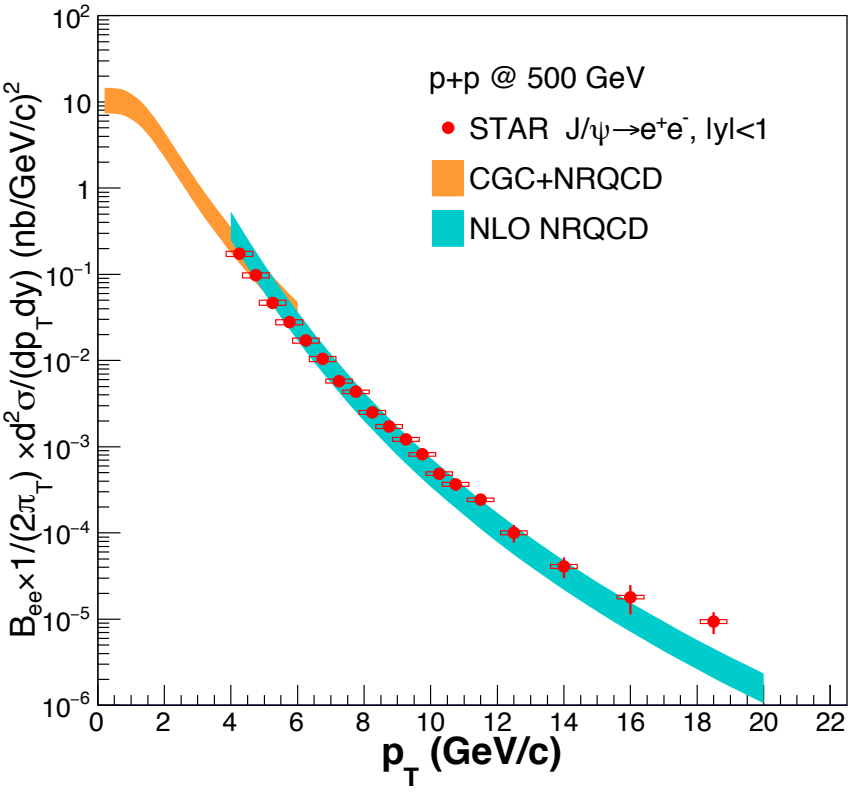

Figure 5.1: Inclusive J/ψ invariant cross section as a function of p_T in proton-proton collisions at $\sqrt{s}$ = 500 GeV at mid-rapidity of $|y| < 1$, compared with Next-Leading Order NRQCD calculations at the kinematic range of $4 < p_T < 20$ GeV/c with cyan band. The Color Glass Condensate + NRQCD prediction was also shown at low p_T range of $0 < p_T < 6$ GeV/c with Orange band. The red error bars represent the statistical uncertainties. The red boxes depict the systematic uncertainties.

kinematic range of $4 < p_T < 20$ GeV/c. The CGC + NRQCD prediction [36] is also shown at low p_T range ($0 < p_T < 6$ GeV/c) with orange band. The prediction from both model are the prompt J/ψ, the B decayed J/ψ contribution is not included in the prediction. By comparing the measurement and predictions, it can be concluded that the NLO NQRCD can reasonably described the J/ψ spectrum with $p_T > 4$ GeV/c. The prediction from CGC+NRQCD can also describe the J/ψ spectrum with $4 < p_T < 6$ GeV/c. At very high p_T range, the data is higher than the NLO NRQCD calculations. However, one should noticed that the B meson decayed J/ψ have a very large contribution to the inclusive J/ψ production [48] in this p_T range. It would be very interesting to look at the overlapping range between two models at $4 < p_T < 6$ GeV/c. The perturbative QCD can only have the prediction power on $c\bar{c}$ production at high p_T ($p_T \gg M_c$). While the CGC effective theory can only give the short distance $c\bar{c}$ pair production cross section at low p_T range, and the CGC effective theory has been combined with the LDEMs from NRQCD to provide a analytic expression for low p_T J/ψ. Two different models in the overlap range give a consistent result. An exact kinematic was used to match the collinear factorization calculation and small x factorization in pA collision [118].

This overlapping range in p+p collision may also indicates some exact kinematic, which will help to better understand the J/ψ production mechanism. The measured inclusive J/ψ cross section with a large kinematic range could provide a good constraint on the theoretical understand of J/ψ production.

Here, we are lack of prediction from CSM. However, by comparing the measurement [119] at STAR in proton-proton collision at $\sqrt{s}$ = 200 GeV and the measurements at LHC energies [120] also in proton-proton collision, even with the NNLO* CS corrections, the CS cross section are still underestimated the measurements at high p_T range at both energies. Thus, the CSM would expected to be also underestimated the J/ψ spectrum in p+p $\sqrt{s}$ = 500 GeV. However, this does not necessary to concluded that NRQCD describes the J/ψ production. Measurements on the unpolarized cross section alone does not fully described the J/ψ production mechanism, the polarization is also a key observable. While NLO NRQCD calculations [121] predicted transverse polarization at LHC and CDF, which contradict with measurements both at ALICE [122] and CDF [123] measurements. More studies are need to further understand the J/ψ production mechanism.

5.2 Measurement of the relative yields of $\psi(2S)$ to J/ψ mesons

The inclusive J/ψ production includes both prompt and non-prompt J/ψ. The prompt J/ψ production consists of the direct production and feed-down contribution from excited states like $\psi(2S)$ and χ_c. It is hard to extract the feed-down contribution from theory. Most of the case the relative yields of $\psi(2S)$ to J/ψ mesons ratio is used to estimate the contribution from $\psi(2S)$ contribution. The relative yields of $\psi(2S)$ to J/ψ mesons ratio is give by:

$$R = \frac{\frac{d^2\sigma}{dp_T dy}(\psi(2S)) \cdot \mathcal{B}(\psi(2S) \to e^+e^-)}{\frac{d^2\sigma}{dp_T dy}(J/\psi) \cdot \mathcal{B}(J/\psi \to e^+e^-)}. \tag{5.2}$$

Most of the systematic uncertainties from acceptance and efficiency correction are largely cancel out in the measurement. The $\psi(2S)$ is measured in the kinematic range of 4 < p_T < 12 GeV/c at mid-rapidity. The $\psi(2S)$ signal has been shown in Figure 4.23. The measured $\psi(2S)$ kinematic range is very large, it needs to think about where to place the data point. The same measurement with a large bin width will give very different physics information by placing the data point in different place in the bin. In this analysis, the data point is placed at the position where the yield coincides with the integrated yield of this bin. The $\psi(2S)$ yield shape has been assumed to be the same as J/ψ as discussed in analysis. The yield ratio is shown in Figure 5.2, the red bar shows the statistical uncertainty. The red box shows the systematic uncertainty. Measurements from

other experiment at different colliding energies in p+p and p+A collisions [124, 125] are also shown. With different collision energies and collision systems, the yield's ratio shows a global trend, and our measurement follows such a trend.

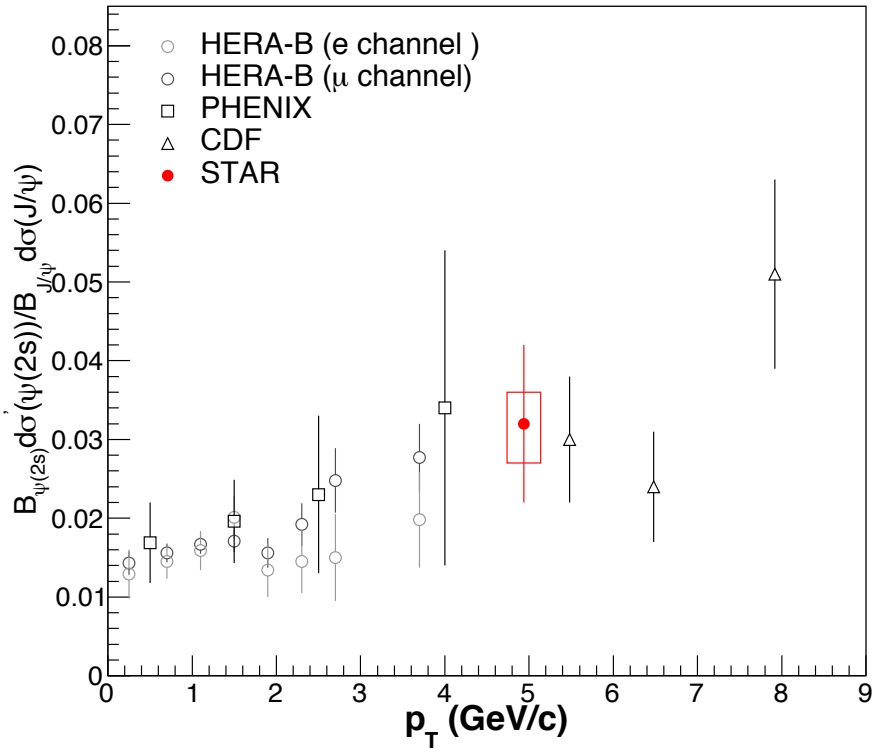

Figure 5.2: The relative yields of $\psi(2S)$ to J/ψ mesons. The kinematic range of this analysis is $4 < p_T < 12$ GeV/c in the mid-rapidity of $|y| < 1$. The J/ψ measurement from other experiment measurements are from HEAR-B electron channel, HEAR-B muon channel, PHENIX measurement, as well as CDF measurement. The red error bar represents the statistical uncertainty. The red box represents the statistical uncertainties.

The relative yield ratio of $\psi(2S)$ over J/ψ is 3.2 $\pm$ 1% in the kinematic range of 4 $< p_T <$ 12 GeV/c. Here, the branch ratio is also included in the ratio measurement. The branch ratio of $\psi(2S) \to e^+e^-$ and $\psi(2S) \to e^+e^-$ branch ratio is $(7.35 \pm 0.18)\times10^{-3}$ and (5.94 ± 0.06)% respectively. The relative yield can help to unfold the inclusive J/ψ component to direct J/ψ. The ratio itself is also a test of the CSM and NRQCD models.

5.3 J/ψ x_T scaling

The J/ψ production has been studied in both the p_T spectra and polarization. However, the details of the $c\bar{c}$ production and its evolution are still black boxes, very litter details are known in these process. All these process are highly dependent on phenomenon study. The study of the J/ψ production at parton level may shed light on the J/ψ production mechanism. Previous measurements of pion production [126, 127] in

high energy p+p collisions have shown that the invariant cross section of inclusive pion follows the x_T scaling law. The scaling can be expressed in the follow two expression:

$$E\frac{d^\sigma}{dp^3} = \frac{1}{p_T^n} f(x_T), \tag{5.3}$$

or

$$E\frac{d^\sigma}{dp^3} = \frac{1}{(\sqrt{s})^n} g(x_T), \tag{5.4}$$

where $x_T = 2p_T/\sqrt{s}$, the $f(x_T)$ and $g(x_T)$ are universal functions, which 'scales', depend only on x_T. n gives the form of the force-law between constituents, n=0 in the e^+e^- collisions, while n=4 for the QED process and Vector Gluon exchange process in the p+p collisions. The scatting between quark and meson by exchanging a quark will give n=8. When other QCD process involved, the n will varies according to the x_T and $\sqrt{s}$. Hence, the n reflects evolution of the parton distribution functions of proton and the fragmentation functions.

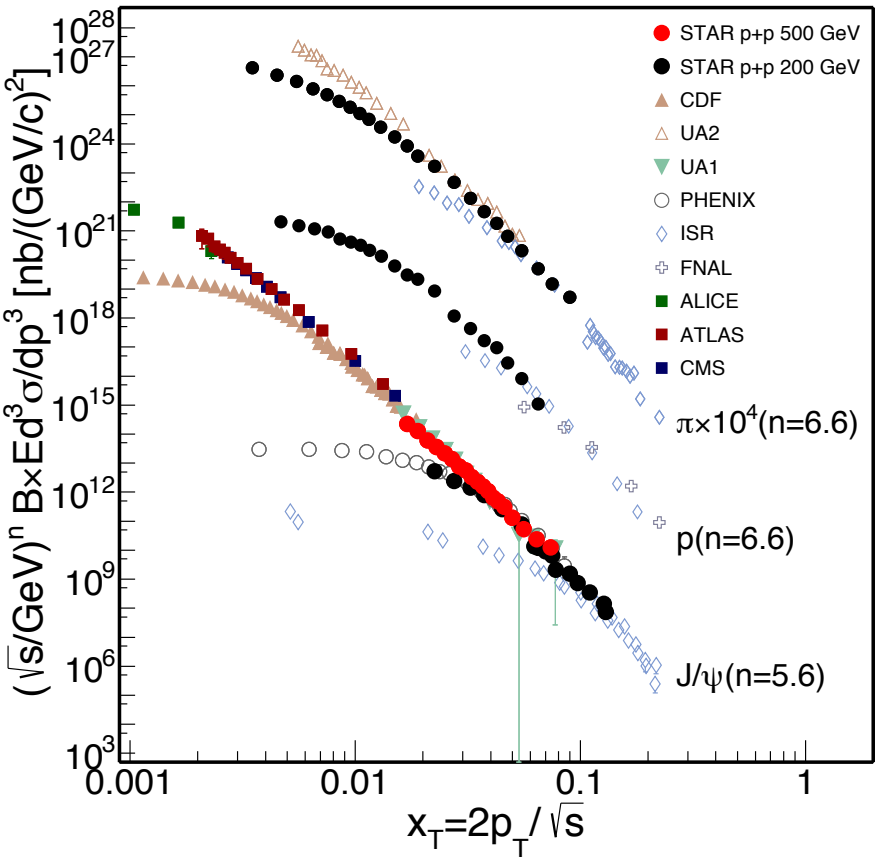

Figure 5.3: J/ψ, pion and proton x_T distribution in different collision energies. The pion measurement are from [126, 127] , The proton results are from [128], The J/ψ results are from CDF, UA1, PHENIX, ISR, FNAL, ATLAS, ALICE, CMS, as well as STAR p+p collision at $\sqrt{s}$ = 200 GeV and the new results at $\sqrt{s}$ = 500 GeV.

The inclusive J/ψ, pion, and proton invariant cross section [129] in proton-proton collisions at different energies are shown in Figure 5.3. The red solid circles are the our

measurements. The red bars show the statistical uncertainties. The red boxes show the systematic uncertainties. Our measurement covers the x_T range of 0.016 < x_T < 0.08. J/ψ measurements from CDF, UA1, PHENIX, ISR, FNAl, ATLAS, ALICE, CMS as well as STAR p+p 200 GeV are also shown. The collision energy varies from $\sqrt{s}$ = 30 GeV to $\sqrt{s}$ = 7 TeV. A global fitting of the scaling range J/ψ cross section at different collision energies was carried out. The scaling range is taken as p_T > 5 GeV/c. The fitting function is:

$$B \times \frac{d^3\sigma}{dp^3} = A(\sqrt{s})\frac{1}{p_T^n}(1 - x_T)^m, \tag{5.5}$$

$A(\sqrt{s})$ is the normalization factor. The fitting gives a result of n= 5.6 $\pm$ 0.2. This formula has been used to fit our new measurement alone with p_T > 4 GeV/c, which gives n = 5.2 $\pm$ 0.2. The results are consistent with each other, which indicates that our measurement with J/ψ p_T > 4 GeV/c is also following the x_T scaling. In the parton model, n represents the number of point-like constituents taking an active role in the interaction. The pion and proton also shows x_T scaling at high p_T range but with n = 6.6 $\pm$ 0.1. At high p_T, the power parameter n is more closer to the predictions from COM and CEM (n $\backsimeq$ 6) and much smaller than that from NNL0* CSM prediction (n $\backsimeq$ 8).

The scaling at high p_T indicates that despite of very different $c\bar{c}$ production cross section at different collision energies, the evolution of $c\bar{c}$ to the J/ψ shows an universal behavior. The evolution of $c\bar{c}$ can be taken as an independent process from $c\bar{c}$ production. Similar scaling is also observed in the J/ψ polarization measurement at high p_T [130]. At high p_T range, the gluon has a large momenta, thus the spatial size is small. Hence, the production of $c\bar{c}$ is likely originated from a $2 \rightarrow 2$ parton-parton hard scatting. On the other hand, J/ψ with p_T < 4 GeV/c shows deviation from the x_T scaling. At this low p_T range, the large gluon size will introduce spatial overlapping in the thin distance. Then, the $c\bar{c}$ is more likely origin from multi-scatting [118]. Thus, the $2 \rightarrow 2$ scattering picture is not suitable in the range. Hence, the deviation from the scaling which mostly indicates parton can not treat as point like parton below this p_T scale.

5.4 J/ψ production as a function of charged-particle multiplicity

The charged-particle multiplicity in MB events and in J/ψ events are shown in Figure 5.4. The open blue circles are unfolded charged-particle multiplicity in MB events. J/ψ events has been divided into two different J/ψ p_T intervals: 4 < p_T < 8 GeV/c and p_T > 8 GeV/c. These two intervals events are shown in open black circles and open black squares, respectively. The p_T integrated J/ψ events is also shown with solid black circle markers. In this analysis, there are five multiplicity intervals: 1-7, 8-14, 15-21,

22-28, 29-42. The charged-particle multiplicity starts with 2 charged particles in J/ψ events, which originated from the requirement of J/ψ been reconstructed first.

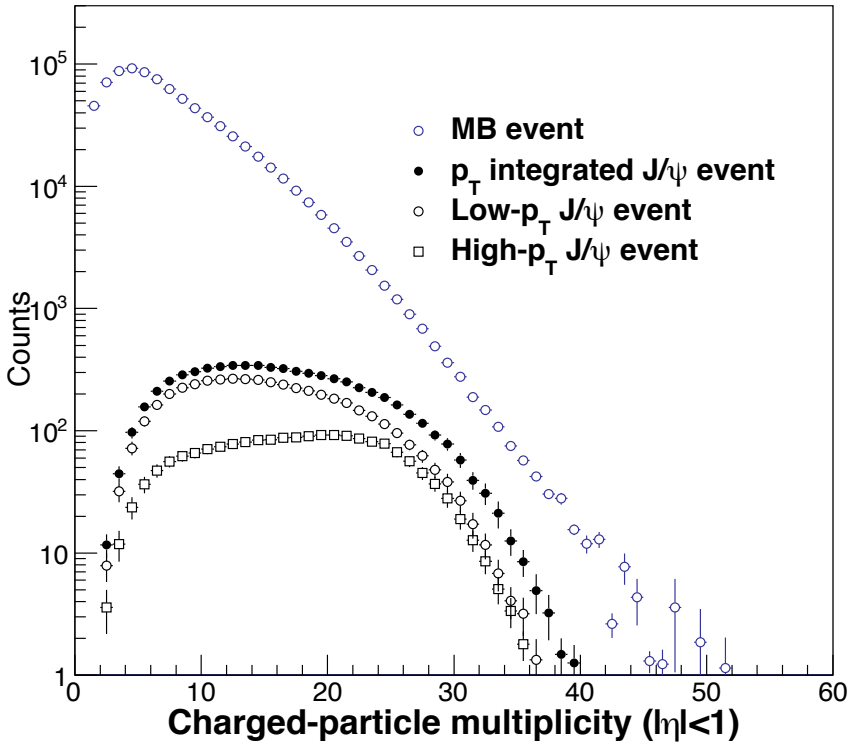

Figure 5.4: The charged-particle multiplicity distribution for MB events and J/ψ events. The open blue circles are the unfolded and trigger bias corrected charged-particle multiplicity in MB events. Open black squares are the unfolded charged-particle multiplicity in J/ψ events with J/ψ p_T > 8 GeV/c. Open black circles are also the distribution in J/ψ events but with 4 < p_T $\leq$ 8 GeV/c. The J/ψ p_T integrated events' charged-particle multiplicity are shown in solid black circles.

The relative yield of inclusive J/ψ as a function of charged-particle multiplicity is evaluated from the inclusive J/ψ cross section and the probability of each multiplicity interval in MB events:

$$\frac{N^i_{J/\psi}}{< N_{J/\psi} >} = \frac{N^{inclusive}_{J\psi}}{2\pi\epsilon\mathcal{L}p_T\Delta p_T\Delta y}\frac{N_{MB}}{N^{inclusive}_{J/\psi}}\frac{N^i_{J/\psi}}{N^i_{MB}}, \tag{5.6}$$

where $N^{inclusive}_{J\psi}$ is the total inclusive J/ψ counts in BHT1 trigger events, $N^i_{J/\psi}$ is the number of J/ψ counts in the ith multiplicity interval, N_{MB} is the total event number between multiplicity 1 and 42. N^i_{MB} is the total event number in ith multiplicity interval. ϵ and $\mathcal{L}$ are the J/ψ reconstruction efficiency and the integrated luminosity for BHT1 trigger. The inclusive J/ψ relative yields at different p_T intervals as a function of charged-particle multiplicity at central rapidity are shown in Figure 5.5. The relative yields are presented with their statistical (vertical bars) and systematic uncertainties. The p_T integrated relative J/ψ, high-p_T J/ψ, and low-p_T J/ψ are represented in solid

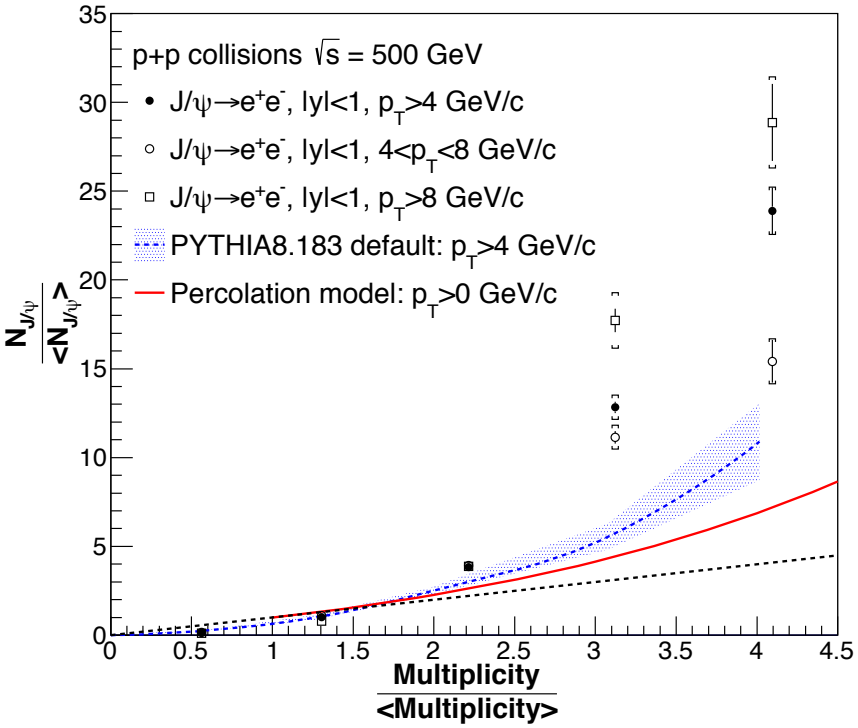

Figure 5.5: The inclusive J/ψ relative yields at different p_T intervals as a function of charged-particle multiplicity at central rapidity. The relative yields are presented with their statistical (vertical bars) and systematic uncertainties. The p_T integrated relative J/ψ, high-p_T J/ψ, and low-p_T J/ψ are represented in solid black circles, open black squares, and open black circles respectively. The predictions from PYTHIA 8.183 event generator and percolation model are shown in dashed blue band and red line respectively. The diagonal (dashed) line is also shown to guide the eye.

black circles, open black squares, and open black circles respectively. The predictions from PYTHIA 8.183 event generator and percolation model are shown in dashed blue band and red line respectively. The diagonal (dashed) line is also shown to guide the eye. A stronger than linear increase is observed and the increase trend shows a strong p_T dependence.

There are four mechanisms associated with $c\bar{c}$ production in PYTHIA8: 1) The first (hardest) hard process, 2) Hard process in MPI, 3) Gluon splitting which is originated from hard process and 4) initial or final state radiation (ISR/FSR). The first hard process describes the $c\bar{c}$ production in the first, normally also the hardest, $2 \rightarrow 2$ hard process. In RHIC energies, the $2 \rightarrow 2$ $c\bar{c}$ production process is dominated by gluon fusion ($gg \rightarrow c\bar{c}$). In the MPI scenario, the $c\bar{c}$ is produced in the subsequent hard processes, it is similar to the first hard process but in consecutive interactions. The produced gluon in the hard process has a probability to split into a $c\bar{c}$ pair. This hard process gluon split could also contributed in the $c\bar{c}$ production. Gluon which originates from initial and final state radiation could also split into a $c\bar{c}$ pair. This $c\bar{c}$ production process is called ISR/FSR. With all these four mechanism considered, the prediction from PYTHIA8 can

only described the J/ψ production as a function of charged-particle multiplicity at low multiplicity range and it underestimates the increase trend at high multiplicities. The similar phenomenon is observed at LHC energy of $\sqrt{s}$ = 7 TeV in proton-proton collisions [86]. This indicates there are some other processs which affect the J/ψ production at high multiplicities.

The percolation model [91] assumes that all projectiles, in high-energy hadronic collisions, have finite spatial extension and collide at finite impact parameter by means of elementary praton-parton collisions. The parton-parton collision will produce strings which constitute the elementary sources of particle production. The size of string is determined by the source's mass ($\propto 1/m_T$). Moreover, these strings can interact, overlapping, with each other. Thus, the effective number of soft strings will be reduced by overlapping. The scenario is also suitable for J/ψ production, but the size of the strings is different from soft process. Then in the high-energy collision scenario, the total charged-particle multiplicity is reduced, due to soft sources overlapping. While the hard process is less affected by sources overlapping due to the smaller size. As a consequence, the J/ψ production as a function of charged-particle multiplicity from percolation model prediction will have a faster-than-linear increase. Figure 5.5 only shows the p_T-integrated percolation calculation prediction. As describing above, the prediction curve expect to have a p_T dependence, the higher the p_T of particle the stronger the deviation from the linear expectation. Measurement at LHC shows that the percolation model can qualitatively described the trend of open charm, open beauty and hidden charm production [86].

ALICE measurement shows that the strong than linear increase has no p_T dependence and a more gentle increase compared to our measurements. At the LHC energies, the double J/ψJ/ψ production in a single proton-proton collision has been measured, and the production cross-section is 4.1 $\pm$ 1.2 nb [131]. However, at RHIC highest p+p energy $\sqrt{s}$ = 500 GeV, we were not observed any J/ψ events which included an open charm produced. As percolation model described, the hard source could also affect by overlapping, while at RHIC energy the lower production rate of hard source will less affect by it. Then a more stronger increase is shown at RHIC energy. The p_T dependent calculations from percolation model compare with our measurement will help to understand the $c\bar{c}$ pair production scenario and the evolution of the production scenario as a function of collision energy.

5.5 Summary

In summary, we measured the high p_T (p_T > 4 GeV/c) inclusive J/ψ spectrum in p+p collision at $\sqrt{s}$ = 500 GeV at mid-rapidity through the dielectron channel at the

STAR experiment. The J/ψ spectrum can well described by the NLO NRQCD calculation. For 4 < p_T < 6 GeV/c, the CGC+NRQCD can also describe the J/ψ spectrum. The high p_T spectrum is found to follow the x_T scaling. The relative yields of $\psi(2S)$ to J/ψ mesons is also presented in 4 < p_T < 12 GeV/c at mid-rapidity and the relative yield ratio is 3.2 $\pm$ 1%. A global trend is observed in the relative yield ratios from different collision energies and collision species. Our measurement follows such a global trend. J/ψ production as a function of the charged-particle multiplicity is studied. The measurements are divided into two J/ψ p_T intervals: 4 < p_T < 8 GeV/c and p_T > 8 GeV/c. A stronger than linear increase trend was observed in both the low-p_T interval and high-p_T interval, and the incerase shows a strong p_T dependence. The p_T integrated J/ψ yield in events with a multiplicity of 4 times of the average charged-particle multiplicity is a factor of 25 larger than the average J/ψ yield. The PYTHIA 8.183 calculations with the MPI contributions can described the trend at low multiplicity range. However, it underestimated the J/ψ yields at high multiplicities. The lacking of other quantitative models estimated at $\sqrt{s}$ = 500 GeV prevent us to learn more on the strong than linear increase trend of J/ψ production and its p_T dependence.

Chapter 6 Outlook

6.1 Detector Upgrades

STAR has proposed several detector upgrades related to J/ψ particle: Inner TPC sector upgrade and End-cap Time of upgrade.

6.1.1 Inner Time Projection Chamber (iTPC) Upgrade

Time Projection Charmer (TPC) is the key detector for STAR physics program, it has been operated for over 15 years. The performance of TPC is close to the original design requirements like tracking efficiency, momentum resolution, and the energy loss measurements. As mentioned, the inner sector of TPC was design to have separated pad row rather than continuous pad coverage in outer TPC sectors, which have been shown in Figure 3.7. The separated pad design was limited by the available packing density of the front end electronics (FEE) channels. Hence, the inner sector is not contribute significantly in improving the dE/dx resolution. The inner TPC section serves to extend the position measurements along the track to small radii thus improving the momentum resolution.

The STAR Collaboration has proposed an upgrade on TPC which will improve dE/dx measurements, tracking performance, as well as larger track acceptance. The upgrade included increasing the inner TPC segmentation, renewing the inner wires grids in the MWPCs, as well as replace all readout electronics to match the increased number of channels in the inner sectors [132]. The pad size design of the new iTPC has been carried out using the STAR simulation framework. The number of pad row increased to 40 for inner TPC sector with a pad size of 15.5 $\times$ 4.5 mm^2. The current inner TPC configuration has 13 widely spaced pad rows. At STAR, the track quality requires at least 15 hits in the TPC. Then, tracks with a large pseudo-rapidity that traverse 13 rows of the current inner TPC are disregarded. The increase of the number of pad rows in the inner section will increase the acceptance for low p_T particle tracks. Figure 6.1 [132] shows the tracking efficiency of pion, kaon, and proton as a function of pseudo-rapidity and transverse momentum for current TPC and proposed iTPC configurations in Au+Au collisions at $\sqrt{s}$ = 200 GeV. The efficiencies from current TPC are shown in blue curves. The efficiencies from iTPC are shown in red curves. The tracking efficiency has a huge enhancement compared to current TPC configuration in $1 < |\eta| < 1.5$ range, as well as low p_T hadrons at mid-rapidity. Figure 6.2 [132] shows the dE/dx resolution as a function of tracking length from the primary vertex to the edge of TPC for different pseudo-rapidity regions. The dE/dx resolution of proposed iTPC is

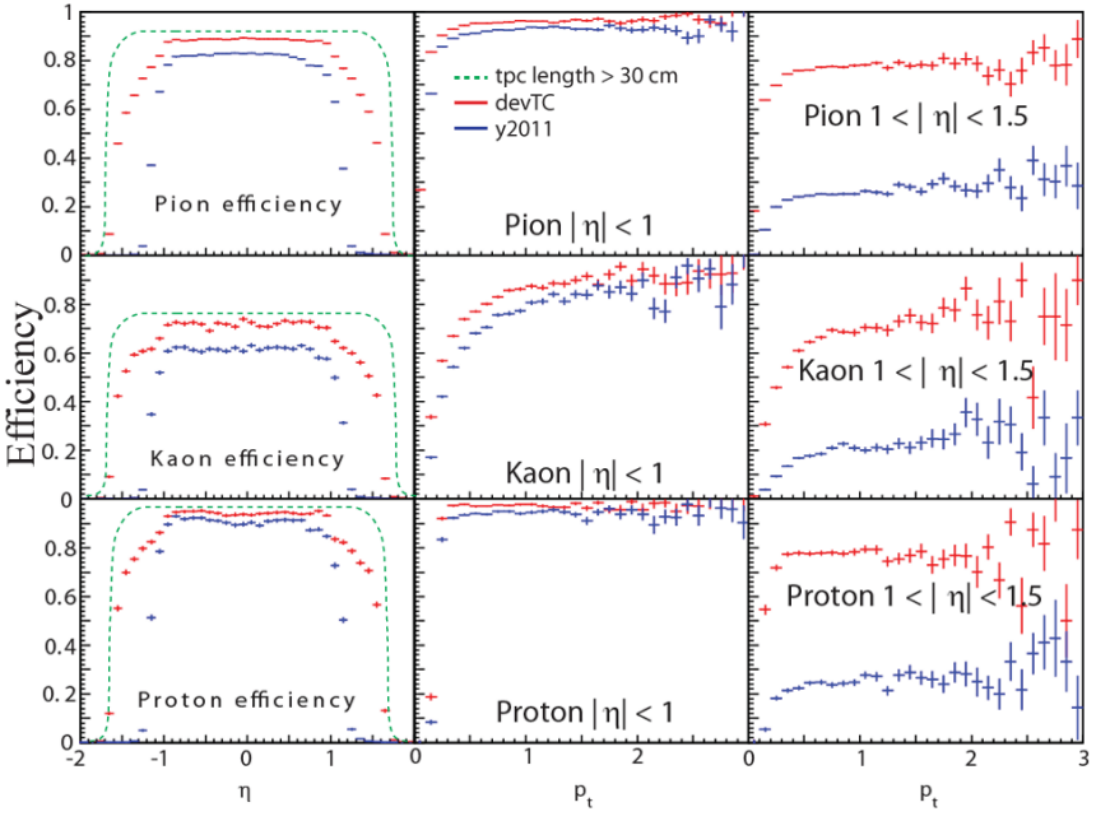

Figure 6.1: Tracking efficiency of pion, kaon, and proton as a function of η and p_T (GeV/c) for the current TPC design (blue) and iTPC design (red). The theoretical curve for the efficiency for tracks longer than 30 cm is shown as a green dashed line.

better than current TPC, this effect is very obvious at high pseudo-rapidity region ($|\eta| > 1$). The dE/dx resolution is inversely proportional to the number of sampled TPC hits used in calculating the dE/dx. The iTPC can provide 40 hits, while current inner TPC can only provide 13 hits. With more sampling in dE/dx measurement point, a better dE/dx resolution is expected. Most analysis in STAR requires at least 25 hits for track quality, which select tracks with a radius of 170 and 90 cm for current TPC and iTPC respectively. Figure 6.3 shows the acceptance maps for different hadrons with current TPC configuration and iTPC configuration. The pseudo-rapidity has been converted to rapidity using the appropriate transformation Jacobians.

The proposed iTPC upgrade will replace all 24 existing inner sectors in the STAR TPC with new, fully instrumented, sectors. By double the number of pads in the inner sectors and increase the sampled path length of tracks passing over the pads from 20% to 95%, iTPC will provide better momentum resolution, better dE/dx resolution, and most importantly it will provide improved acceptance at high rapidity to $|\eta| \leq 1.5$ compared to the current TPC coverage of $|\eta| \leq 1$. The iTPC upgrade extends the rapidity coverage by 50%, which provide a major benefit for many analyses.

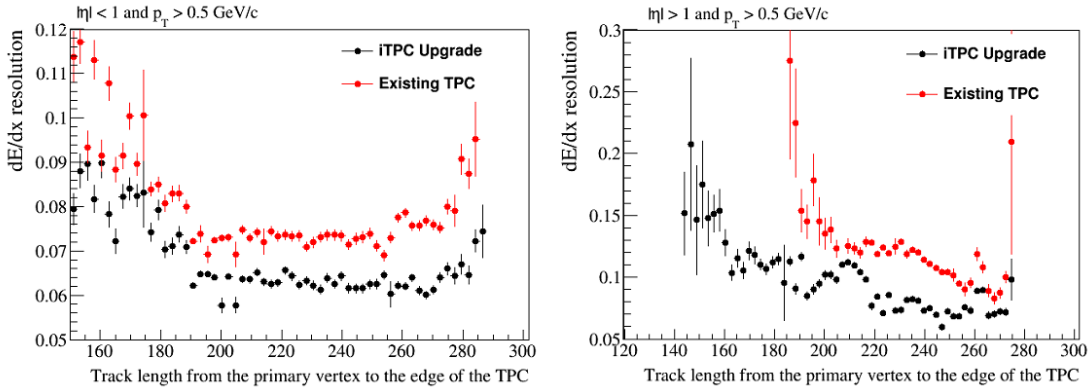

Figure 6.2: (Color online) the comparisons of dE/dx resolution between current TPC configuration and upgraded iTPC in $|\eta| < 1$ (Left) and $|\eta| > 1$ (Right).

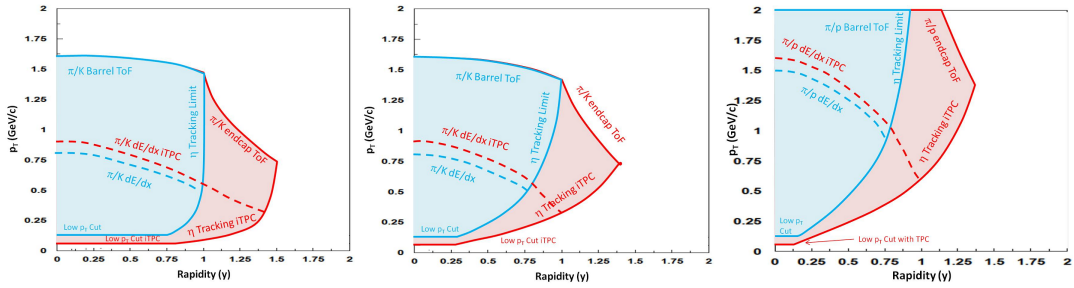

Figure 6.3: (Color online) the y-p_T acceptance maps for pions (Left), kaons (Middle), and protons (Right) showing the limits due to tracking coverage and PID.

6.1.2 End-cap Time of Flight (eTOF) Upgrade

The STAR Collaboration and the CBM collaboration propose to install the CBM TOF detectors [133] at the east side of STAR. The End-cap TOF detector will arrange as a "wheel", which consistent of 36 CBM TOF modules with a total of 108 MRPCs and 6912 readout channels. The eTOF will be placed at 2.8 away from the interaction point. The "wheel" has a inner radii of 0.75 m and a outer radii of 1.7 m, the pseudo-rapidity coverage is -1.5 < η < -1.1. The schematic view of the proposed eTOF is shown in Figure 6.4. The barrel and end-cap TOF used the same MRPC technology, and thus has a similar 80 ps time resolution. By using iTPC and eTOF information, the π/K identification capability will extend to1.60 GeV/c. Compared to using iTPC only, which can do the π/K identification at 0.75 GeV/c, it is a big enhancement. And the $(\pi, K)/p$ identification capability will extend to 3.0 GeV/c [111]. The identification capability of iTPC and eTOF are shown in Figure 6.3. TOF system have a good identification for the electron in the kinematic range of 0.2 < p_T < 2.0 GeV/c, which can be used to measure the J/ψ at forward rapidity.

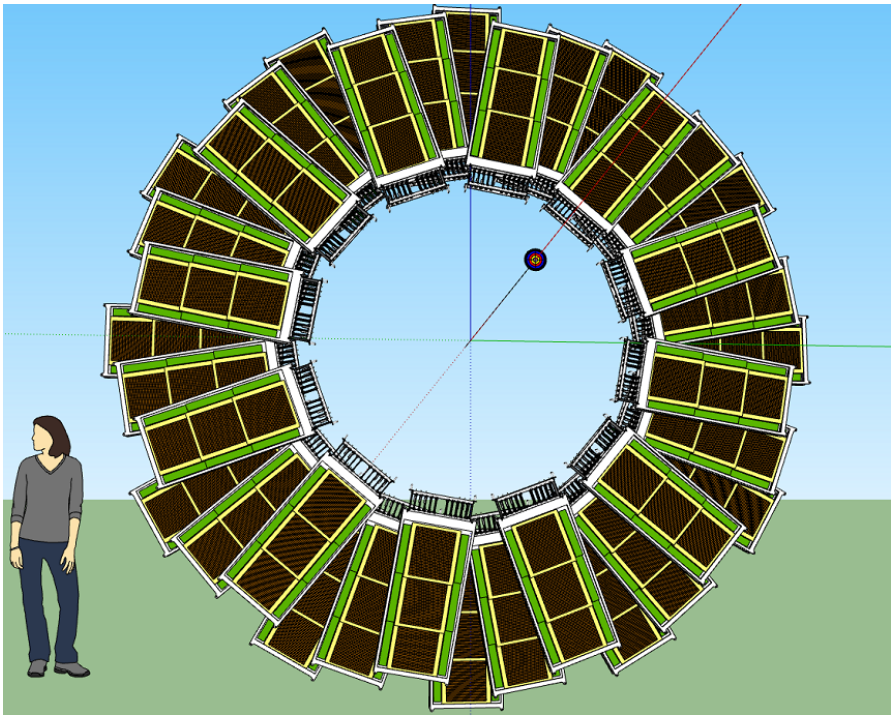

Figure 6.4: A schematic view of the proposed eTOF layout.

6.2 J/ψ relate physics

6.2.1 J/ψ production in single-transverse-polarized proton-proton collisions

In 2008, Yuan [134] proposed that the transverse single-spin asymmetry (SSA) of J/ψ is sensitive to the J/ψ production mechanism by assuming a nonzero gluon Sivers function [135]. The nonzero gluon Sivers function is a transverse-momentum-dependent distribution (TMD) that describes the correlation between the transverse spin of the proton and the k_T of the partons within it. Furthermore, Yuan predicts that in ep collision the SSA will vanished when the produced $c\bar{c}$ are produced in a color-singlet configuration, and a nonzero SSA arises from color-octet t configuration from the gluon Sivers function. While in the proton-proton collisions, the nonzero gluon Sivers function will affect the produced $c\bar{c}$ production. Furthermore, in the color-single model, the hadronization will not affect the quantum number of this $c\bar{c}$. Thus, there will have a nonzero SSA for color-single model. While for the Color-octet model, the inital-state and final-state effects will cancel out each other, then the SSA from color-octet model will vanished.

PHENIX Collaboration measured the J/ψ transverse single-spin asymmetry in p+p collisions at $\sqrt{s}$ = 200 GeV. The results are shown in Figure 6.5 [136], where $x_F = 2p_L/\sqrt{s}$, p_L is the momentum along the beam direction. In the mid-rapidity range, they reconstructed about 600 J/ψ signals in di-electron channel and are dominated by low p_T range. As shown in figure, reconstructed J/ψ kinematic range is $0 < p_T < 6$ GeV/c. The measurement has larger uncertainties. Moreover, as we have discussed, both CSM

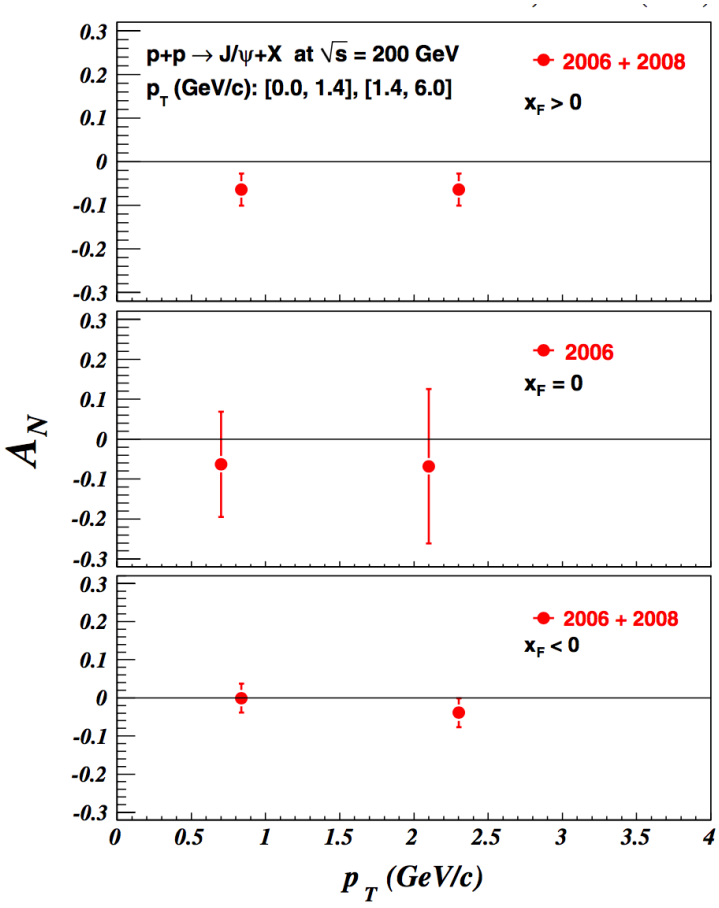

Figure 6.5: (color online). Transverse single-spin asymmetry of J/ψ mesons ploted against J/ψ transverse momentum.

and NRQCD are describing high p_T J/ψ production. While at RHIC Run11, we reconstructed about 9k J/ψ in a kinematic range of $4 < p_T < 20$ GeV/c via di-electron channel. The measured J/ψ with a total of 10% uncertainty. With this data sample, the J/ψ transverse single-spin asymmetry can extend to high p_T and make a fair comparison with models, which may shed light on J/ψ mechanism study.

6.2.2 J/ψ in the ultra peripheral proton-proton collision

The polarized protons at RHIC provide an unique opportunity to measure A_N for exclusive J/ψ in ultra-peripheral p$^{\uparrow}$+p collisions (UPC) [137] at $\sqrt{s}$ = 500 GeV. The measurement is at a fixed Q^2 of 9 GeV^2 and $10^{-4} < x < 10^{-1}$. A nonzero asymmetry would be the first signature of a non-zero GPD E for gluons. The gluon GPD E is sensitive to spin-orbit correlations and is intimately connected with the orbital angular momentum carried by partons in the nucleon and thus with the proton spin puzzle. The elastic process can be choose by using "Roman Pots" detectors. The SARTRE event generator has described the ρ^0 production in UPC at Au+Au collision. And it also has

been used to simulate exclusive J/ψ production in p$^{\uparrow}$+p UPC. The acceptance of the STAR RP PHASE-II^{*} system in t matches well the t spectrum in UPC collisions, as shown in Figure 6.6. The J/ψ UPC events are selected by requiring at least one of the two protons fired the RPs. J/ψ can be reconstructed in di-electron or di-muon channel. The estimation in di-electron channel shows, after taking all trigger and reconstruction efficiencies, there will be $\sim$11k J/ψ signals for a delivered luminosity of 400 pb^{-1}.

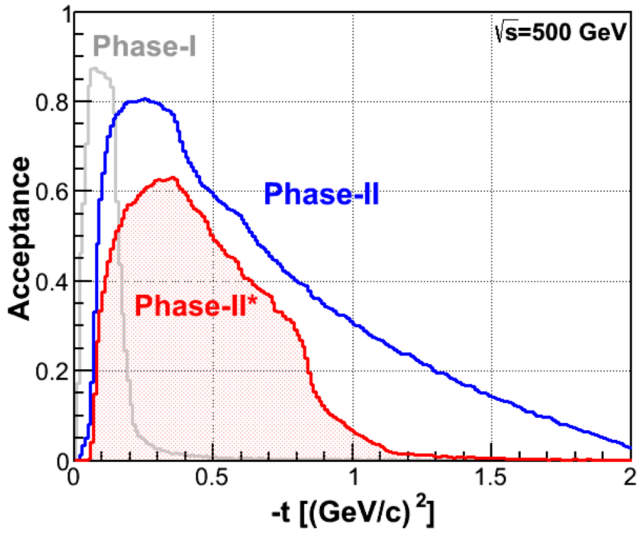

Figure 6.6: (left) Acceptance of protons in exclusive p+p scattering at $\sqrt{s} = 500$ GeV as function of t for a possible future upgrade (blue) and the STAR set up since 2015 (PHASE-II) (red) configuration. The acceptance for the original STAR Phase-I setup is also shown (grey).

References

[1] Lee, Tsung-Dao, and Chen-Ning Yang. "Question of parity conservation in weak interactions." *Physical Review 104.1 (1956): 254*.

[2] Wu, Chien-Shiung, et al. "Experimental test of parity conservation in beta decay." *Physical review 105.4 (1957): 1413*.

[3] Breidenbach, Martin, et al. "Observed behavior of highly inelastic electron-proton scattering." *Physical Review Letters 23.16 (1969): 935*.

[4] Bloom, Elliott D., et al. Breidenbach, Martin, et al. "High-Energy Inelastic e-p Scattering at 6° and 10°." *Physical Review Letters 23.16 (1969): 930*.

[5] S. W. Herb *et al.*, "Observation of a Dimuon Resonance at 9.5 GeV in 400-GeV Proton-Nucleus Collisions" *Phys. Rev. Lett., 1977, 39(252)*.

[6] Abe, F., et al., "Observation of top quark production in pp collisions with the Collider Detector at Fermilab." *Physical review letters 74.14 (1995): 2626*.

[7] J. Beringer et al, "Review of Particle Physics." *Phys. Rev. D, 2012, 86 (010001)* .

[8] Higgs, Peter W, "Broken symmetries and the masses of gauge bosons." *Physical Review Letters 13.16 (1964): 508*.

[9] Aad, Georges, et al. "Observation of a new particle in the search for the Standard Model Higgs boson with the ATLAS detector at the LHC." *Physics Letters B 716.1 (2012): 1-29*.

[10] H. Fritzsch and M. Gell-Mann, "Current algebra: Quarks and what else?" *Proceedings of the XVI International Conference on High Energy Physics. C720906V2, 135 (1972)*.

[11] D.W. Duke and R.G. Roberts, "Deep inelastic scattering and asymptotic freedom: A detailed analysis and confrontation." *Nucl. Phys. B 166, 243 (1980)*.

[12] S. Bethke, "The 2009 world average of α_s." *Eur. Phys. J. C 64, 689 (2009)*.

[13] Wilson, Kenneth G, "Confinement of quarks." *Physical Review D 10.8 (1974): 2445*.

[14] Aubert, Jean-Jacques, et al. "Experimental observation of a heavy particle J." *Physical Review Letters 33.23 (1974): 1404*.

[15] Augustin, J-E., et al, "Discovery of a Narrow Resonance in e+e Annihilation." *Physical Review Letters 33.23 (1974): 1406*.

[16] Nakamura, K et al, "Review of Particle Physics" *J. Phys. G, 2010, 37(075021)*.

[17] Hagiwara, K., et al, "Review of particle properties" *Physical Review D 66.1 (2002):010001*.

[18] Nakamura, Kenzo, and Particle Data Group, "Review of particle physics" *Journal of Physics G: Nuclear and Particle Physics 37.7A (2010): 075021*.

[19] Norrbin, E., and Torbjorn Sjostrand, "Production and hadronization of heavy quarks." *The European Physical Journal C-Particles and Fields 17.1 (2000): 137-161*.

[20] Einhorn, M. B., and S. D. Ellis, "Hadronic production of the new resonances: Probing gluon distributions" *Physical Review D 12.7 (1975): 2007*.

[21] Berger, Edmond L., and D. Jones, "Inelastic photoproduction of J/ψ and upsilon by gluons" *Physical Review D 23.7 (1981): 1521*.

[22] Baier, Rudolf, and R. Ruckl, "Hadronic collisions: a quarkonium factory" *Zeitschrift f□r Physik C Particles and Fields 19.3 (1983): 251-266*.

[23] G.A. Schuler, "Quarkonium production and decays" *arXiv:hep-ph/9403387*.

[24] Artoisenet, Pierre, J. P. Lansberg, and Fabio Maltoni, "Hadroproduction of J/ψ and Υ in association with a heavy-quark pair" *Physics Letters B 653.1 (2007): 60-66*.

[25] Campbell, J., F. Maltoni, and F. Tramontano, "QCD corrections to J/ψ and Υ production at hadron colliders" *Physical review letters 98.25 (2007): 252002*.

[26] Artoisenet, P., et al, "Υ production at Fermilab Tevatron and LHC energies" *Physical review letters 101.15 (2008): 152001*.

[27] Fritzsch, Harald, "Producing heavy quark flavors in hadronic collisions?A test of quantum chromodynamics" *Physics Letters B 67.2 (1977): 217-221*.

[28] Halzen, Francis, "CVC for gluons and hadroproduction of quark flavours" *Physics Letters B 69.1 (1977): 105-108*.

[29] Gluck, M., J. F. Owens, and Et Reya, "Gluon contribution to hadronic J/ψ production" *Physical Review D 17.9 (1978): 2324*.

[30] Amundson, J. F., et al, "Quantitative tests of color evaporation: Charmonium production" *Physics Letters B 390.1-4 (1997): 323-328*.

[31] Bodwin, Geoffrey T., Eric Braaten, and Jungil Lee, "Comparison of the color-evaporation model and the nonrelativistic QCD factorization approach in charmonium production" *Physical Review D 72.1 (2005): 014004*.
[32] Bodwin, Geoffrey T., Eric Braaten, and G. Peter Lepage, "Rigorous QCD analysis of inclusive annihilation and production of heavy quarkonium" *Physical Review D 51.3 (1995): 1125*.
[33] Butenschoen, Mathias, and Bernd A. Kniehl, "J/ψ polarization at the Tevatron and the LHC: nonrelativistic-QCD factorization at the crossroads" *Physical review letters 108.17 (2012): 172002*.
[34] Ma, Yan-Qing, Kai Wang, and Kuang-Ta Chao, "J/ψ (ψ(2S)) production at the Tevatron and LHC at $\mathcal{O}(\alpha_s^4 v^4)$ in nonrelativistic QCD." *Physical review letters 106.4 (2011): 042002*.
[35] Gong, Bin, et al, "Polarization for Prompt J/ψ and $\psi(2S)$ Production at the Tevatron and LHC" *Physical review letters 110.4 (2013): 042002*.
[36] Ma, Yan-Qing, and Raju Venugopalan, "Comprehensive description of J/ψ production in proton-proton collisions at collider energies" *Physical review letters 113.19 (2014): 192301*.
[37] Gelis, Francois, et al, "Heavy quark pair production in high-energy pA collisions: quarkonium" *Nuclear Physics A 915 (2013): 1-23*.
[38] Kharzeev, D. E., Eugene M. Levin, and Kirill Tuchin, "Nuclear modification of the J/ψ transverse momentum distributions in high energy pA and AA collisions" *Nuclear Physics A 924 (2014): 47-64*.
[39] Gelis, Francois, et al, "The color glass condensate" *Annual Review of Nuclear and Particle Science 60 (2010): 463-489*.
[40] Gribov, Leonid Vladimirovic, Evgenij M. Levin, and Michail G. Ryskin, "Semihard processes in QCD" *Physics Reports 100.1-2 (1983): 1-150*.
[41] Mueller, Alfred H., and Jianwei Qiu, "Gluon recombination and shadowing at small values of x" *Nuclear Physics B 268.2 (1986): 427-452*.
[42] STAR collaboration, "J/ψ production at high transverse momenta in p+p and Au+Au collisions at $\sqrt{s_{NN}}$ = 200 GeV" *Physics Letters B 722.1 (2013): 55-62.*
[43] Lam, C. S., and Wu-Ki Tung, "Systematic approach to inclusive lepton pair production in hadronic collisions" *Physical Review D 18.7 (1978): 2447*.
[44] Collins, John C., and Davison E. Soper, "Angular distribution of dileptons in high-energy hadron collisions" *Physical Review D 16.7 (1977): 2219*.
[45] Gottfried, Kurt, and John David Jackson, "On the connection between production mechanism and decay of resonances at high energies" *Nuovo Cimento (1955-1965) 33.2 (1964): 309-330*.
[46] Gluck, M., J. F. Owens, and Et Reya, "Gluon contribution to hadronic J/ψ production" *Physical Review D 17.9 (1978): 2324*.
[47] Adare, A., et al, "Ground and excited state charmonium production in p+p collisions at $\sqrt{s}$= 200 GeV" *Physical Review D 85.9 (2012): 092004*.
[48] Aad, Georges, et al, "Measurement of the differential cross-sections of inclusive, prompt and non-prompt J/ψ production in proton?proton collisions at $\sqrt{s}$ = 7 TeV" *Nuclear Physics B 850.3 (2011): 387-444*.
[49] Baier, Rudolf, and R. Ruckl, "Hadronic production of J/ψ and υ: transverse momentum distributions" *Physics Letters B 102.5 (1981): 364-370*.
[50] Abe, F., et al, "Production of J/ψ Mesons from χ_c Meson Decays in $p\bar{p}$Collisions at $\sqrt{s}$= 1.8 TeV" *Physical Review Letters 79.4 (1997): 578*.
[51] Lansberg, J. P, "J/ψ production at $\sqrt{s}$ = 1.96 and 7 TeV: colour-singlet model, NNLO* and polarization" *Journal of Physics G: Nuclear and Particle Physics 38.12 (2011): 124110*.
[52] Aubert, B., et al, "Time-integrated and time-dependent angular analyses of B $rightarrow$ J/$\psi K\pi$: A measurement of $cos?(2\beta)$ with no sign ambiguity from strong phases" *Physical Review D 71.3 (2005): 032005*.
[53] Aad, Georges, et al, "Measurement of the differential cross-sections of inclusive, prompt and non-prompt J/ψ production in proton?proton collisions at $\sqrt{s}$ = 7 TeV" *Nuclear Physics B 850.3 (2011): 387-444*.
[54] Aaij, R., et al, "Measurement of J/ψ production in pp collisions at $\sqrt{s}$ = 7 TeV" *The European Physical Journal C 71.5 (2011): 1-17*.
[55] Artoisenet, P., et al, "υ production at Fermilab Tevatron and LHC energies" *Physical review letters 101.15 (2008): 152001*.
[56] Buscemi, Francesco, "All entangled quantum states are nonlocal" *Physical review letters 108.20 (2012): 200401*.

[57] Ma, Yan-Qing, Kai Wang, and Kuang-Ta Chao, "Complete next-to-leading order calculation of the J/ψ and $\psi(2S)$ production at hadron colliders" *Physical Review D 84.11 (2011): 114001*.
[58] Aamodt, Kenneth, et al, "Rapidity and transverse momentum dependence of inclusive J/ψ production in pp collisions at $\sqrt{s}$ = 7 TeV" *Physics Letters B 704.5 (2011): 442-455*.
[59] Aaij, R., et al, "Measurement of J/? production in pp collisions at $\sqrt{s}$ = 7 TeV" *The European Physical Journal C 71.5 (2011): 1-17*.
[60] STAR collaboration, "J/ψ production at high transverse momenta in p+p and Au+Au collisions at $\sqrt{s}$ = 200 GeV" *Physics Letters B 722.1 (2013): 55-62*.
[61] Abellan Beteta, Carlos, et al, "Measurement of $\psi(2S)$ meson production in pp collisions at $\sqrt{s}$ = 7 TeV" *European Physical Journal C, 2012, vol. 72, p. 2100 (2012)*.
[62] S. Chekanov et al, "Measurements of inelastic and photoproduction at HERA" *The European Physical Journal C-Particles and Fields 27.2 (2003): 173-188*.
[63] Abdallah, J., et al, "Study of inclusive J/? production in two-photon collisions at LEP II with the DELPHI detector" *Physics Letters B 565 (2003): 76-86*.
[64] Abulencia, A., et al, "Polarizations of J/ψ and $\psi(2S)$ Mesons Produced in $p\bar{p}$ Collisions at $\sqrt{s}$ = 1.96 TeV" *Physical review letters 99.13 (2007): 132001*.
[65] Braaten, Eric, Bernd A. Kniehl, and Jungil Lee, "Polarization of prompt J/ψ at the Fermilab Tevatron" *Physical Review D 62.9 (2000): 094005*.
[66] Gong, Bin, Xue Qian Li, and Jian-Xiong Wang, "QCD corrections to J/ψ production via color-octet states at the Tevatron and LHC" *Physics Letters B 673.3 (2009): 197-200*.
[67] Lansberg, J. P, "On the mechanisms of heavy-quarkonium hadroproduction" *The European Physical Journal C-Particles and Fields 61.4 (2009): 693-703*.
[68] Abelev, Betty, et al, "J/ψ Polarization in p p Collisions at $\sqrt{s}$= 7 TeV" *Physical review letters 108.8 (2012): 082001*.
[69] CMS collaboration, "Measurement of the prompt J/? and ? (2S) polarizations in pp collisions at $\sqrt{s}$= 7 TeV" *Physics Letters B 727.4 (2013): 381-402*.
[70] Back, J. J., et al, "Measurement of J/ψ polarization in pp collisions at $\sqrt{s}$ = 7 TeV" *The European Physical Journal C 73.11 (2013)*.
[71] STAR Collaboration, "J/ψ polarization in p+p collisions at in STAR" *Physics Letters B 739 (2014): 180-188*.
[72] Adare, A., et al, "Transverse momentum dependence of J/ψ polarization at midrapidity in p+p collisions at $\sqrt{s}$= 200 GeV" *Physical Review D 82.1 (2010): 012001*.
[73] Atomssa, Ermias T, "J/ψ production measurements by the PHENIX experiment" *The European Physical Journal C-Particles and Fields 61.4 (2009): 683-686*.
[74] Strikman, Mark, "Transverse structure of the nucleon and multiparton interactions" *Progress of Theoretical Physics Supplement 187 (2011): 289-296*.
[75] Frankfurt, L., M. Strikman, and C. Weiss, "Transverse nucleon structure and diagnostics of hard parton-parton processes at LHC" *Physical Review D 83.5 (2011): 054012*.
[76] Aguilar-Benitez, M., et al, "Comparative properties of 400 GeV/c proton-proton interactions with and without charm production" *Zeitschrift f□r Physik C Particles and Fields 41.2 (1988): 191-196*.
[77] Abelev, B., et al, "J/ψ production as a function of charged particle multiplicity in pp collisions at $\sqrt{s}$= 7 TeV" *Physics Letters. Section B: Nuclear, Elementary Particle and High-Energy Physics 712.3 (2012): 165-175*.
[78] Chatrchyan, Serguei, et al, "Jet and underlying event properties as a function of charged-particle multiplicity in proton?proton collisions at $sqrts$ = 7 TeV " *The European Physical Journal C 73.12 (2013): 2674*.
[79] Abelev, Betty, et al, " Underlying Event measurements in pp collisions at $\sqrt{s}$= 0.9 and 7 TeV with the ALICE experiment at the LHC" *Journal of High Energy Physics 2012.7 (2012): 116*.
[80] Abelev, Betty, et al, "Multiplicity dependence of two-particle azimuthal correlations in pp collisions at the LHC " *Journal of High Energy Physics 2013.9 (2013): 49*.
[81] M.Y. Azarkin, I.M. Dremin and M. Strikman, "Jets in multiparticle production in and beyond geometry of proton-proton collisions at the LHC " *Phys. Lett. B 735 (2014) 244*.
[82] M. Strikman, "Comments on the observation of high multiplicity events at the LHC" *Phys. Rev. D 84 (2011) 011501*.
[83] B.Z. Kopeliovich, H.J. Pirner, I.K. Potashnikova, K. Reygers and I. Schmidt, " J/ψ in high-multiplicity pp collisions: Lessons from pA collisions" *Phys. Rev. D 88 (2013) 116002*.
[84] LHCb collaboration, " Observation of double charm production involving open charm in pp collisions at $\sqrt{s}$ = 7 TeV," *Journal of High Energy Physics 2012.6 (2012): 141*.

[85] LHCb collaboration, "Observation of J/ψ pair production in pp collisions at $\sqrt{s}$ = 7 TeV" *Phys. Lett. B 707 (2012) 52*.
[86] Adam, Jaroslav, et al, "Measurement of charm and beauty production at central rapidity versus charged-particle multiplicity in proton-proton collisions at $\sqrt{s}$ = 7 TeV " *Journal of High Energy Physics 2015.9 (2015): 148*.
[87] PHOBOS collaboration, " Phobos results on charged particle multiplicity and pseudorapidity distributions in Au + Au, Cu + Cu, d + Au and p + p collisions at ultra-relativistic energies" *Phys. Rev. C 83 (2011) 024913*.
[88] H.J. Drescher, M. Hladik, S. Ostapchenko, T. Pierog and K. Werner, " Parton based Gribov-Regge theory" *Phys. Rept. 350 (2001) 93* .
[89] K. Werner, B. Guiot, I. Karpenko and T. Pierog, "Analysing radial flow features in p?Pb and p?p collisions at several TeV by studying identified particle production in EPOS3" *Phys. Rev. C 89 (2014) 064903*.
[90] K. Werner, B. Guiot, I. Karpenko and T. Pierog, "Analysing radial flow features in p-Pb and pp collisions at several TeV by studying identified particle production in EPOS3 " *Phys. Rev. C 89 (2014) 064903*.
[91] E.G. Ferreiro and C. Pajares, "High multiplicity pp events and J/ψ production at LHC " *Phys. Rev. C 86 (2012) 034903* .
[92] M. Harrison *et al.*, "RHIC project overview." *Nucl. Instr. Meth. A 499, 235 (2003)*.
[93] Alekseev, I., et al, " Polarized proton collider at RHIC" *Nucl. Instr. and Meth. A 499, 392 (2003)*.
[94] RHIC Accelerator Division, "RHIC Configuration Manual" *https://www.bnl.gov/cad/accelerator/docs/pdf/RHICConfManual.pdf*.
[95] K.H. Ackermann *et al.* (STAR Collaboration), "STAR detector overview." *Nucl. Instr. Meth. A 499, 624 (2003)*.
[96] D. Beavis *et al.*, "The STAR Heavy Flavor Tracker Technical Design Report." *https://drupal.star.bnl.gov/STAR/starnotes/public/sn0600*.
[97] M. Anderson *et al.*, "The STAR time projection chamber: a unique tool for studying high multiplicity events at RHIC." *Nucl. Instr. Meth. A 499, 659 (2003)*.
[98] The STAR TOF Collaboration, "Proposal for a large area Time of Flight system for STAR." *https://drupal.star.bnl.gov/STAR/starnotes/public/sn0621*.
[99] M. Beddo *et al.*, "The STAR Barrel Electromagnetic Calorimeter." *Nucl. Instr. Meth. A 499, 725 (2003)*.
[100] L. Ruan *et al.*, "Perspectives of a Midrapidity Dimuon Program at RHIC: A Novel and Compact Muon Telescope Detector." *J. Phys. G 36, 095001 (2009)*.
[101] C. A. Whitten Jr. (for the STAR Collaboration), "The Beam-Beam Counter: A Local Polarimeter at STAR." *AIP Conference Proceedings 980 (1), 390 (2008)*.
[102] W.J Llope *et al.*, "The STAR Vertex Position Detector." *Nucl. Instr. Meth. A 759, 23 (2014)*.
[103] C. Adler *et al.*, "The RHIC zero degree calorimeters" *Nucl. Instr. Meth. A 470, 488 (2001)*.
[104] M. Anderson *et al.*, "A readout system for the STAR time projection chamber" *Nucl. Instr. and Meth. A499 (2003) 659?678*.
[105] Van Buren, Gene *et al.*, "Correcting for distortions due to ionization in the STAR TPC" *Nucl. Instr. and Meth. A566 (2006) 22-25*.
[106] Billoir, Pierre *et al.*, "Progressive track recognition with a Kalman-like fitting procedure" *Computer Physics Communications 57.1-3 (1989): 390-394*.
[107] H. Bichsel, "A method to improve tracking and particle identification in TPCs and silicon detectors." *Nucl. Instr. Meth. A 562, 154 (2006)*.
[108] M. Shao *et al.*, "Beam test results of two kinds of multi-gap resistive plate chambers." *Nucl. Instr. Meth. A 492, 344 (2002)*.
[109] B. Bonner *et al.*, "A single Time-of-Flight tray based on multigap resistive plate chambers for the STAR experiment at RHIC." *Nucl. Instr. Meth. A 508, 181 (2003)*.
[110] B. Bonner *et al.*, "A single Time-of-Flight tray based on multigap resistive plate chambers for the STAR experiment at RHIC." *Nucl. Instr. Meth. A 508, 181 (2003)*.
[111] M. Shao *et al.*, "Extensive particle identification with TPC and TOF at the STAR experiment." *Nucl. Instr. Meth. A 558, 419 (2006)*.
[112] Nelson, R. E., R. Vogt, and A. D. Frawley, "Narrowing the uncertainty on the total charm cross section and its effect on the J/ψ cross section " *Physical Review C 87.1 (2013): 014908*.
[113] Balewski, " http://www.star.bnl.gov/protected/spin/balewski/2005-PPV-vertex/effiMC/" .

[114] X. Li, W. Xu, P. Kurnadi, S. Sakai, G. Wang, J. Dunlop, T. Ullrich, A. Suaide and W. Xie, " High p_T Non-photonic Electron Production in p+p collisions at $\sqrt{s}$ = 200 GeV" *https://drupal.star.bnl.gov/STAR/starnotes/private/psn0522*.
[115] Zebo Tang, " J/ψ production at high transverse momentum in p+p and Cu+Cu collisions at $\sqrt{s_{NN}}$ = 200 GeV" *https://drupal.star.bnl.gov/STAR/starnotes/private/psn0469*.
[116] Trzeciak, Barbara, "J/ψ polarization in p+p collisions at $\sqrt{s}$= 200 GeV in STAR" *Phys. Lett. B 739 (2014) 180*.
[117] Hua-Sheng Shao, Hao Han, et al, "Yields and polarizations of prompr J/ψ and $\psi(2S)$ production in hadronic collisions" *Energ. Phys. (2015) 2015: 103*.
[118] Stasto, Anna M., et al, " Matching collinear and small x factorization calculations for inclusive hadron production in p A collisions" *Physical Review D 90.1 (2014): 014047*.
[119] STAR collaboration, " J/? production at high transverse momenta in p+ p and Au+ Au collisions at $\sqrt{s} = 200GeV$" *Physics Letters B 722.1 (2013): 55-62*.
[120] Aad, Georges, et al, "Measurement of the differential cross-sections of inclusive, prompt and non-prompt J/? production in proton?proton collisions at $\sqrt{s}$ = 200 GeV " *Nuclear Physics B 850.3 (2011): 387-444*.
[121] Butenschoen, Mathias, and Bernd A. Kniehl, "J/ψ polarization at the Tevatron and the LHC: nonrelativistic-QCD factorization at the crossroads" *Physical review letters 108.17 (2012): 172002*.
[122] Abelev, Betty, et al, "J/ψ Polarization in p+p Collisions at $\sqrt{s}$= 7 Te " *Physical review letters 108.8 (2012): 082001*
[123] Abulencia, A., et al, " Polarizations of J/ψ and $\psi(2S)$ Mesons Produced in $p\bar{p}$ Collisions at $\sqrt{s}$ = 1.96 TeV" *Physical review letters 99.13 (2007): 132001*.
[124] Abt, Iris, et al, "A Measurement of the $\psi(2S)$ to J/ψ production ratio in 920 GeV proton-nucleus interactions " *The European Physical Journal C 49.2 (2007): 545-558*.
[125] Adare, A., et al, "Ground and excited state charmonium production in p+p collisions at $\sqrt{s}$ = 200 GeV" *Physical Review D 85.9 (2012): 092004*.
[126] Adams, John, et al, " Identified hadron spectra at large transverse momentum in p+ p and d+ Au collisions at $\sqrt{s}$ = 200 GeV" *Physics Letters B 637.3 (2006): 161-169*.
[127] Adams, John, et al, "Pion, kaon, proton and anti-proton transverse momentum distributions from p+ p and d+ Au collisions at $\sqrt{s}$ = 200 GeV" *Physics Letters B 616.1 (2005): 8-16*.
[128] Antreasyan, D., et al, " Production of hadrons at large transverse momentum in 200-, 300-, and 400-GeV p?p and p-nucleus collisions" *Physical Review D 19.3 (1979): 764*.
[129] Abelev, B. I., et al, " J/ψ production at high transverse momenta in p+ p and Cu+Cu collisions at $\sqrt{s_{NN}}$ = 200 GeV" *Physical Review C 80.4 (2009): 041902*.
[130] Mustafa, Mustafa, " Overview of recent results from the STAR experiment" *Nuclear Physics A 956 (2016): 43-50* .
[131] A. V. Berezhnoy., et al, " Double J/? meson Production at LHC and 4c-tetraquark state" *Phys. Rev. D84 (2011) 094023*.
[132] L. Adamczyk *et al.* (STAR Collaboration), "Proposal for STAR Inner TPC Sector Upgrade (iTPC)." *STAR Internal Note: SN0619 (2015)*.
[133] N. Herrmann, "Technical Design Report for the CBM Time-of-Flight System (TOF)." *GSI Report GSI-2015-01999 (2014)*.
[134] Yuan, Feng, " Heavy-quarkonium production in single-transverse-polarized high-energy scattering" *Physical Review D 78.1 (2008): 014024*.
[135] Sivers, Dennis, "Hard-scattering scaling laws for single-spin production asymmetries " *Physical Review D 43.1 (1991): 261*.
[136] Adare, A., et al, " Measurement of transverse single-spin asymmetries for J/ψ production in polarized p+ p collisions at $\sqrt{s}$= 200 GeV" *Physical Review D 82.11 (2010): 112008*.
[137] Klein, Spencer, and Joakim Nystrand, "Photoproduction of J/ψ and Υ in pp and $\bar{p}p$ Collisions" *arXiv preprint hep-ph/0310223 (2003)*.

ACKNOWLEDGMENTS

要毕业了，六年时间如白驹过隙，匆匆而过。硕博连读的六年时光中，在从事的科研工作中有过挫折，有过兴奋，有过沮丧，但更多的是一份感激。在论文完成之际，我想对我工作和学习上提供帮助的各位老师和同学表达我最真诚的感谢。

首先感谢我的导师李澄教授，从我进入科大的第一天开始，就有幸开始跟随李老师学习。李老师渊博的学识、严谨专注的治学态度以及和蔼可亲的为人让我受益良多。感谢帮助和指导我的唐泽波老师，他一直是我学习研究和生活中的良师益友。研究工作中，在工作遇见困难的时期，泽波给予了我积极的引导和帮助，生活中，给与我的人生建议和指引，让我终身受益。感谢在布鲁克海文国家实验室期间，阮丽娟研究员对我的指导和关心，阮老师明白了当的办事风格以及在科研中对细节的把控，让我深切体会到工作在对撞物理一线的研究人员的严格要求。同时要感谢陈宏芳、邵明、孙勇杰和周意老师多年来给我提供学术指导以及无私帮助，让我能够顺利的完成研究。在博士学习的几年，诸位导师的无私帮助和谆谆教诲，平易近人、求真务实、积极进取的人生态度也深深影响着我，诸位导师的辛勤栽培和人格魅力将是我博士学习期间重要的财富。在此，我要向诸位导师表示崇高的敬意和衷心的感谢！

感谢实验室的查王妹、杨帅、杨驰、黄炳矗、陈天翔、张辉、江琨等师兄的指导和照顾。感谢周龙、王小壮两门同学一路相随。感谢张生辉、赵晓坤、谢冠男，杨荣星、尤文豪、赵晓坤、刘圳、胡东栋、陈小龙、王鹏飞、洪道金、纪媛婧、巨欣跃、宋国锋、吕游、吴奕涛、周健、李子味、李洋等师弟师妹。感谢他们对我学习生活的关系和帮助，有了他们的陪伴，我才能充实地度过这几年，愿同窗之间友谊长存。同时也要感谢在 bnl 一起生活的朋友们：王旭、张金龙 (胖)、徐一飞、冯赵、张正桥、张金龙 (瘦)、褚晓璇、涂彪、黄欣杰、周晨升，大家一起的生活充满了乐趣。如果感激的人朋友中，我一不小心漏掉了谁，请不要介意你在“等”中，不是你不重要，只是匆匆行文，疏漏还望谅解。

最后，我要感谢全力支持我的家人，我的父母、兄长、嫂子还有我济铭侄儿。多年来，他们默默地支持我，给我坚持的动力和力量，让我能够投身到自己喜欢的工作学习当中，不断的激励我战胜困难和挫折。

Presentations and Publication List

Presentations:

1. J/ψ production in p+p collisions at $\sqrt{s}$ = 500 GeV at the STAR experiment (poster)

   XXVI international conference on ultrarelativistic heavy-ion collisions (QM2017), February 6-11, 2017, Chicago, USA.

2. Heavy quarkonium production at STAR experiment

   Brookhaven National Laboratory Early Career Researcher Symposium 2016, Dec. 13, 2016, Upton NY, USA.

3. J/ψ production in p+p and Au+ Au collisions at STAR experiment

   Hot Quarks 2016, Sep. 12 - 17 2016, South Padre Island, USA.

4. Heavy quarkonium production at STAR experiment

   RHIC & AGS Annual Users' Meeting, Jun. 7 - 10 2016, Upton , USA.

5. J/ψ production in p+p collisions at $\sqrt{s}$ = 500 GeV from STAR

   Annual Fall Meeting of the APS Division of Nuclear Physics 2015, Oct. 28 - 31 2015, Santa Fe, USA.

6. J/ψ and ψ(2S) production at p+p $\sqrt{s}$ = 500 GeV collisions from STAR experiment

   The 31st Winter Workshop on Nuclear Dynamics, Jan. 25 - 31, 2015, Keystone Resort, USA.

7. J/ψ production in p+p collisions at $\sqrt{s}$ = 500 GeV from STAR (poster)

   XXIV international conference on ultrarelativistic nucleus-nucleus collisions (QM 2014), May 19 - 24, 2014, Darmstadt, Germany.

Publication List:

1. *J/ψ and ψ(2S) measurement in p+p collisions at $\sqrt{s}$ = 500 GeV in the STAR experiment*

   Q. Yang (for the STAR Collaboration), Journal of Physics: Conf. Series 636 (2015) 012004

2. *J/ψ production in p+p at $\sqrt{s}$ = 500 GeV collisions and Au+ Au collisions at $\sqrt{s_{NN}}$ = 200 GeV at the STAR experiment*

   Q. Yang (for the STAR Collaboration), Journal of Physics: Conf. Series 832 (2017) 012026

3. *Systematic study of the experimental measurements on J/ψ cross sections and kinematic distributions in p + p collisions at different energies*

   Wangmei Zha, Bingchu Huang, Rongrong Ma, Lijuan Ruan, Zebo Tang, Zhangbu Xu, Chi Yang, Qian Yang, and Shuai Yang, Phys. Rev. C 93, 024919 (2016)

4. *Muon Identification with Muon Telescope Detector at the STAR Experiment*

   T.C. Huang, R. Ma, B. Huang, X. Huang, L. Ruan, T. Todoroki, Z. Xu, C. Yang, S. Yang, Q. Yang, Y. Yang, W. Zha, Nuclear Instruments and Methods in Physics Research A 833 (2016) 88?93.